FLUORESCENT PARTICLE TRACERS FOR SURFACE HYDROLOGY

DISSERTATION

Submitted in Partial Fulfillment

of the Requirements for the

Degree of

DOCTOR OF PHILOSOPHY

at

SAPIENZA UNIVERSITÀ DI ROMA

by

Flavia Tauro

May 2014

VITA

Flavia Tauro was born in Rome, Italy, in 1985. She earned her B.Sc. and M.Sc. in Environmental Engineering from "La Sapienza" University of Rome in 2007 and 2009, respectively. She received her M.Eng. degree in Civil and Environmental Engineering from the Massachusetts Institute of Technology in 2009. Since 2010, she has been working toward her Ph.D. degree in Mechanical Engineering and Hydrology at the New York University Polytechnic School of Engineering and "La Sapienza" University of Rome (dual degree program) under the supervision of Dr. Maurizio Porfiri and Dr. Salvatore Grimaldi. She passed the Ph.D. qualifying exam in January 2011 and the Ph.D. proposal defense in January 2012. She has worked as Graduate Research Assistant under the support of the National Science Foundation CAREER grant No. CMMI-0745753, Grant No. CMMI-0926791, and Grant No. CMMI-1129820; the Office of Naval Research Grant No. N00014-10-1-0988; the MIUR Project PRIN 2009 N. 2009CA4A4A; the Honors Center of Italian Universities (H2CU Sapienza University of Rome); and the American Geophysical Union Horton (Hydrology) Research Grant. Her research interests include environmental sensing, experimental hydrology, and experimental fluid mechanics.

"This is a beautiful river," he said to his companion.

"Yes," said the ferryman, "a very beautiful river, I love it more than anything.
Often I have listened to it, often I have looked into its eyes,
and always I have learned from it. Much can be learned from a river."

ACKNOWLEDGMENT

I owe my deepest gratitude to the guidance, encouragement, and support of my advisors, Prof. Maurizio Porfiri and Prof. Salvatore Grimaldi. Without their advice, caring, and time, I would have never fully appreciated the challenges and the gratification of being a scientist. They have provided me with a unique paradigm of professorship, which has motivated and inspired me throughout my doctoral studies.

I would also like to acknowledge Prof. Aldo Fiori, Prof. Rastislav Levicky, Prof. Francesco Napolitano, Prof. Maria Cristina Rulli, and Prof. George Vradis for serving on this committee and providing encouragement and support in these years. I also express my gratitude to Prof. Lucio Ubertini, Dr. Maria Grillo, and the Honors Center of Italian Universities for their continuous support.

The writing of this dissertation has been an invaluable opportunity to meet and work with wonderful scientists and scholars. I would like to extend my gratitude to Dr. Remi Dingreville, Mr. Ben Esner, Prof. Sean D. Peterson, and Dr. Laurent Pfister for their advice and support.

I would also like to acknowledge my co-authors and collaborators for providing precious contributions that have highly improved the work presented in this dissertation. I am grateful to the undergraduate and graduate students I have had the opportunity to work with and would like to extend special thanks to Mr. Christopher Pagano for his dedication and talent. I would like to acknowledge the entire Mechanical and Aerospace Engineering Department Faculty and Staff and past and current colleagues at the Dynamical Systems Laboratory for making this work enjoyable. Also, I would like to thank long-time friends Vittoria, Graziano, Paola, and Chiara for their unconditional friendship.

Finally, I would like to acknowledge and dedicate this work to my parents and grandmother for their love and for walking along this path beside me no matter how far.

AN ABSTRACT

FLUORESCENT PARTICLE TRACERS FOR SURFACE HYDROLOGY

by

Flavia Tauro

Advisors: Salvatore Grimaldi, Ph.D.
Maurizio Porfiri, Ph.D.

Submitted in Partial Fulfillment of the Requirements

for the Degree of Doctor of Philosophy

May 2014

Surface water processes control downstream runoff phenomena, waste and pollutant diffusion, erosion mechanics, and sediment transport. However, current observational methodologies do not allow for the identification and kinematic characterization of the physical processes contributing to catchment dynamics. Traditional methodologies are not capable to cope with extreme in-situ conditions, including practical logistic challenges as well as inherent flow complexity. In addition, available observational techniques are non-exhaustive for describing multiscale hydrological processes.

This research addresses the need for novel observations of the hydrological community by developing pioneer flow characterization approaches that rely on the mutual integration of traditional tracing techniques and state-of-the-art image-based sensing procedures. These novel methodologies enable the in-situ direct observation of surface water processes through remote and unsupervised procedures, thus paving the way to the development of distributed networks of sensing platforms for catchment-scale environmental sensing. More specifically, the proposed flow characterization methodology is a low-cost measurement system that can be applied to a variety of real-world settings spanning from few centimeters rills in natural catchments to riverine ecosystems. The technique is based on the use of in-house synthesized environmentally-friendly fluorescent particle tracers through digital cameras for direct flow measurement and travel time estimations. Automated image analysis-based procedures are developed

for real-time flow characterization based on image manipulation, template-based correlation, particle image velocimetry, and dimensionality reduction methodologies. The feasibility of the approach is assessed through laboratory-designed experiments, where the accuracy of the methodology is investigated with respect to well-established flow visualization techniques. Further, the transition of the proposed flow characterization approach to natural settings is studied through paradigmatic observations of natural stream flows in small scale channel and riverine settings and overland flows in hillslope environments. The integration of the proposed flow sensing system in a stand-alone, remote, and mobile platform is explored through the design, development, and testing of a miniature aerial vehicle for environmental monitoring through video acquisition and processing.

List of Publications

Journal Publications

[J1] Tauro F., Aureli M., Porfiri M., Grimaldi S.: "Characterization of buoyant fluorescent particles for field observations of water flows", *Sensors*, **10**(12), 11512–11529, 2010.

[J2] Grimaldi S., Petroselli A., Tauro F., Porfiri M.: "Time of concentration: a paradox in modern hydrology", *Hydrological Sciences Journal*, **57**(2), 217–228, 2012.

[J3] Tauro F., Pagano C., Porfiri M., Grimaldi S.: "Tracing of shallow water flows through buoyant fluorescent particles", *Flow Measurement and Instrumentation*, **26**(August 2012), 93–101, 2012.

[J4] Tauro F., Grimaldi S., Petroselli A., Porfiri M.: "Fluorescent particle tracers for surface flow measurements: a proof of concept in a natural stream", *Water Resources Research*, **48**(6), W06528, 2012.

[J5] Tauro F., Grimaldi S., Petroselli A., Rulli M. C., Porfiri M.: "Fluorescent particle tracers for surface flow measurements: a proof of concept in a semi-natural hillslope", *Hydrology and Earth System Sciences*, **16**(8), 2973–2983, 2012.

[J6] Tauro F., Mocio G., Rapiti E., Grimaldi S., Porfiri M.: "Assessment of Fluorescent Particles for Surface Flow Analysis", *Sensors*, **12**(11), 15827–15840, 2012.

[J7] Tauro F., Porfiri M., Grimaldi S., : "Fluorescent Eco-Particles for Surface Flow Physics Analysis", *AIP Advances*, **3**(3), 032108, 2013.

[J8] Tauro F., Rapiti E., Al-Sharab J. F., Ubertini L., Grimaldi S., Porfiri M.: "Characterization of Eco-friendly Fluorescent Nanoparticle-doped Tracers for Environmental Sensing", *Journal of Nanoparticle Research*, **15**(9), 1884, 2013.

[J9] Tauro F., Grimaldi S., Porfiri M.: "Unraveling flow patterns through nonlinear manifold learning", *PLoS ONE*, **9**(3), e91131, 2014.

[J10] Pagano C., Tauro F., Grimaldi S., Porfiri M.: "Large scale particle image velocimetry from an unmanned aerial vehicle", submitted for publication.

[J11] Tauro F., Porfiri M., Grimaldi S.: "Orienting the camera and firing lasers to enhance large scale particle image velocimetry for stream flow monitoring", submitted for publication.

Conference Proceedings

[C1] Grimaldi S., Petroselli A., Nardi F., Tauro F.: "Analisi Critica dei Metodi di Stima del Tempo di Corrivazione", XXXII Convegno Nazionale di Idraulica e Costruzioni Idrauliche, September 14–17 , 2010, Palermo, Italy.

[C2] Tauro F., Porfiri M., Grimaldi S.: "Fluorescent Particles as a Novel Sensing Technology for In-Situ Measurements of Water Flows", ASME 2011 Student Professional Development Conference, April 1–2, 2011, Philadelphia, PA.

[C3] Grimaldi S., Tauro F., Petroselli A., Porfiri M.: "Studio Preliminare di un Tracciante Innovativo con Particelle Fluorescenti per le Misure di Velocità su Versante", Convegno di Medio Termine dell' Associazione Italiana di Ingegneria Agraria, September 22–24 , 2011, Belgirate, Italy.

[C4] Tauro F., Aureli M., Porfiri M., Grimaldi S.: "Buoyant Fluorescent Particles as a Novel Sensing Technology for Field Observations of Water Flows", 2011 Dynamic Systems and Control Conference, October 31–November 2, 2011, Arlington, VA.

[C5] Tauro F., Pagano C., Porfiri M., Grimaldi S.: "Fluorescent Particle Image Tracking Procedure for Shallow Water Flow Tracing", 2012 Dynamic Systems and Control Conference, October 17–19, 2012, Fort Lauderdale, FL.

[C6] Grimaldi S., Tauro F., Petroselli A.: "Studio Preliminare di un Tracciante con Particelle Fluorescenti per le Misure di Velocità Superficiali", XXXIII Convegno Nazionale di Idraulica e Costruzioni Idrauliche, September 10–15, 2012, Brescia, Italy.

[C7] Tauro F., Grimaldi S., Porfiri M., Petroselli A.: "Fluorescent particles for non-intrusive surface flow observations", *Procedia Environmental Sciences*, **19**, 895–903, 2013.

[C8] Tauro F.: "Towards novel observations in hydrology", *AGU Hydrology Newsletter*, November 2013, p. 15–18, (Invited paper).

[C9] Tauro F.: "Fluorescent particle tracer for surface hydrology", *H2CU Magazine*, submitted for publication, 2013 (Invited paper).

[C10] Tauro F., Grimaldi S., Porfiri M.: "A topological framework for flow characterization and identification", 2014 Dynamic Systems and Control Conference, October 22–24, 2014, San Antonio, TX, submitted for publication.

[C11] Pagano C., Tauro F., Grimaldi S., Porfiri M.: "Development and testing of an unmanned aerial vehicle for large scale particle image velocimetry", 2014 Dynamic Systems and Control Conference, October 22–24, 2014, San Antonio, TX, submitted for publication.

Table of Contents

List of Figures

List of Tables

Chapter 1

Introduction

Surface water processes control downstream runoff phenomena [2, 3], waste and pollutant diffusion [4], erosion mechanics [5, 6], and sediment transport [7, 8]. These flows are largely dominated by ephemeral microchannel drainage networks in hillslope areas [9–12]. A quantitative understanding of the flow physics in these areas is currently limited by the lack of effective tracing techniques suitable for basin-scale observations [13]. More specifically, field experiments require environmentally resilient, non-invasive, and low cost measurement systems that can potentially operate in remotely-controlled or unmanned conditions. Furthermore, water turbidity, flow path heterogeneity, and natural flow obstructions impose severe constraints on sensing technologies in field studies [14, 15].

In this dissertation, we present a novel tracing methodology for surface hydrology measurements in natural environments. This innovative technique combines the efficiency and versatility of traditional conceptions while improving their practical feasibility. Specifically, this low-cost tracing methodology can be applied to a variety of real-world settings spanning from few centimeters rills in natural hillslopes to riverine ecosystems. The technique is based on the detection and tracking of $100 - 3000\,\mu\mathrm{m}$ fluorescent spheres through a digital camera for direct flow measurement and travel time estimations. Insoluble buoyant particles are used to limit the tracer dispersion from adhesion to natural substrates and thus minimize the amount of tracing material for experimental measurements. Further, enhanced fluorescence particles allow for non-intrusively detecting the tracer without deploying probes and samplers in the water. The methodology allows for the optimal tuning of the particle dimensions as a function of the flow scenario. Moreover, this inexpensive and automated technology is inherently designed to provide continuous measurements in complex flows, such as shallow water streams, overland flows, and mountainous creeks.

In this Chapter, we present leading-edge tracing methodologies in hydrology and environmental sciences. In addition, we provide an overview on a novel class of tracers that are designed to efficiently provide flow measurements in laboratory and real environments. Contributions of this proposed tracing system and possible enhancements in the hydrological field are finally discussed.

1.1 State of the art on hydrological tracers

Tracers are widely used for investigating, quantifying, and monitoring several physical processes, including overland flow [16], surface and subsurface flow [17–20], water travel time [21, 22], water aging [23], runoff formation [24], and concentration time [13, 25]. These processes are crucial for the analysis of hydrological and environmental phenomena, such as rainfall-runoff modeling, infiltration schemes, pollutant transport, and source identification [2, 26, 27].

1.1.1 Traditional hydrological tracers

Traditional tracers can be broadly classified into four groups, based on the substance or the object released into the water. Such groups are termed "isotopes", "chemicals", "buoys", and "dyes". A comprehensive and critical review of tracer technologies along with their specific field applications is presented in [13].

Isotopes can be either naturally found in water or artificially deployed in streams. Natural isotopes precipitate with rain and modify their properties during the hydrological cycle [28, 29]. On the other hand, artificial radioactive isotopes decay with time and are easily detected by non-invasively measuring their radiation emission. Nevertheless, safety policies on radioactive isotopes release are generally strict and expensive equipment is required for their preparation and detection [25, 30]. Isotopes are mainly used to separate hydrographs into event and pre-event flow [23, 24] and to determine watershed transit times [21, 25, 30–33]. They are commonly used in aquifers, groundwater dynamic observations, and for transport phenomena [34].

Chemicals, such as salt tracers [31, 33], nitrates and lithium [23], and potassium iodide [21], are widely used in surface hydrology, including applications in discharge measurements in small and impervious rivers. Their main advantages are the limited cost, ease of preparation, very low toxicity, and minimal suspended sediment adsorption. Conversely, sampling is necessary to measure the tracer concentration in streams. Therefore, the overall detection procedure does not provide continuous data, can be drastically affected by extreme weather conditions, and requires the presence of supervising operators.

Although drifter buoys are mostly used in oceanography [35, 36], in [37], experiments have been performed to estimate stream flow velocities and catchment travel times for hydrological applications. Buoys are relatively bulky elements that can carry GPS and other devices. Therefore, they are not appropriate for flow monitoring in the hillslope microchannel network.

Dyes have been used in stream water and groundwater hydrology for over 100 years [17, 27, 33]. For instance, they are successfully used to investigate hydraulic connections and flow pathways in [33] due to their enhanced detectability. Dye tracers are generally easily visible but non conservative and highly adsorptive [13, 17, 27, 33]. In other words, they are affected by significant dispersion due to infiltration processes and suspended sediments. High dye concentrations are usually needed and losses

are generally considerable. Dye tracers are generally detected through electrical conductivity measurements and ion exchange chromatography, which both require sampling. Fluorescence is sometimes used to enhance dye tracer detectability, see [13, 19, 20, 22]. Figure 1.1 summarizes the state of the art on hydrological tracers by showing pros and cons of the most important technologies described in literature.

1.1.2 Hydrological tracers for PIV

In addition to the aforementioned tracers, related research on PIV in fluid dynamics and hydrology has fueled the design and characterization of novel particle tracers for flow studies [38]. By acquiring and cross-correlating pairs of subsequent images, PIV identifies displacement vectors of particles moving in a fluid. Once displacements are estimated, fluid velocity vectors at selected points are simultaneously reconstructed [38–40]. Figure 1.2 displays a typical experimental set-up for underwater PIV.

When dealing with large-scale flows, PIV is referred to as Large-scale PIV (LSPIV). Particles of various sizes from microns to millimeters, shapes, and materials are considered in LSPIV research. For instance, foam bubbles, leaves, olive oil drops, and wood or ecofoam chips are used to estimate flow velocities in river sections with LSPIV [14, 15, 41, 42]. Advantages of these tracers are their limited cost and ease of implementation. On the other hand, they are not conservative, tend to dissolve in time-windows of minutes, and only allow for local measurements, which are not appropriate for hillslope microchannels.

LSPIV is intensively used in laboratory shallow water flows in [43]. In these flows, PIV and LSPIV optics and instrumentation can be drastically simplified since standard laboratory lights are usually sufficient for illumination in absence of prominent wave motion. Spherical polypropylene particles with additional matt black lacquer finish are considered in [43]. Their optimal size is determined to be $2\,\mathrm{mm}$ in diameter for good detection and proper flow mapping. The beads are coated with lacquer to both reduce agglomeration effects and enhance the contrast to the background. A particle dispenser is placed a few centimeters above the water surface to guarantee homogeneous seeding and avoid surface waves from falling particles. Since the research entails shallow flows, positively buoyant particles are used in this study. Black polypropylene particles are used in [44] to investigate low-velocity and shallow-depth flows with PIV. The beads' diameter is set to $3\,\mathrm{mm}$ and their specific gravity to $0.62\,\mathrm{kg/m^3}$. By contrast, Large-scale Particle Tracking Velocimetry (LSPTV) is preferred to LSPIV in [45] since it does not require a high particle seeding density and allows for a better spatial resolution. PIV, indeed, tracks the average motion of a particle group within an interrogation area of the image whereas PTV returns one vector for each particle and is therefore only applicable in case of relatively low seeding densities. To further enhance the tracer detection and avoid conglomerates, ellipsoidal beads with $18\,\mathrm{mm}$ long major axis and $6\,\mathrm{mm}$ long minor axis are proposed in [45]. Similarly to [43], floating polypropylene corpuscles with $0.9 - 1.03\,\mathrm{kg/m^3}$ density are considered in [45].

In-situ LSPIV is performed in [14, 15, 41, 46] to measure surface flow velocity and stream discharge

at precise river sections, see Figure 1.3. A mast-mounted camera is used to detect naturally occurring floating particles or ecofriendly tracers deployed upstream of the measurement section. In most studies, the accuracy of the method is highly influenced by the lack of illumination and camera lens distortions. In addition, GPS or total station for locating reference points and correcting camera distortions and operators' presence for collecting samples are necessary for good quality recordings and seeding the stream with particles. The presence of shadows and reflections in the recordings and, most importantly, challenges in identifying particles against other inherent corpuscles represent remarkable limitations in these studies.

Dedicated fluorescent microparticles have been recently synthesized for PIV laboratory scale studies; such tracers show high efficiency and detectability at almost every flow velocity and water depth [44, 47]. Fluorescent polymer nano and microspheres have been used to study near-wall fluid motion [48] and mixing processes in multiconstituent and multiphase fluid systems [47]. In [48], beads are detected through PTV which gives better results than PIV for microfluidic and low density systems. Despite their good detectability, the use of fluorescent microparticles is largely limited to turbulent flow studies in small-scale laboratory experiments [47, 48].

The only example of fluorescent particles designed for potential in-situ LSPIV measurements is reported in [49]. It is therein shown that reflection reduction is a remarkable advantage of fluorescent particles in large-scale hydraulic experiments. In [49], beads are obtained by mixing Rhodamine Water Tracer (WT), a low toxicity fluorescent dye, with commercial grade liquid polyester resin with a density of $1.2\,\mathrm{kg/m^3}$. The resin is formed into a block and subsequently ground into a powder. The powder is then sieved to extract particles smaller than $63\,\mu\mathrm{m}$ for experiments. The tracer is detected through common PIV and, due to the properties of the fluorescent material, good images are obtained in the vicinity of laser-reflective surfaces. Unfortunately, the proposed particle tracers have not been used for in-situ applications but only in laboratory studies on stratified flows [50]. In addition, experimental feasibility of these particles in underwater operations is limited for the porosity of the resin material. Indeed, after their release, particles tend to absorb water and rapidly increase their density as reported in [51]. Therefore, beads lose their natural buoyancy and precipitate.

1.2 Applications to hydrology and environmental sciences

We foresee the implementation of a network of low cost and versatile flow characterization modules for the real-time measurement of surface flow velocities and average travel times in natural catchments, see Figure 1.4. These stations will allow for continuously and remotely monitoring surface waters at the catchment scale. Further, tracking of the fluorescent particles along the drainage network will provide information on surface runoff initiation, rill development on hillslopes, and drainage organization at the larger scale. The use of variable diameters and densities of the tracer particles will guarantee the versatility of the methodology that will operate both in shallow and deep waters.

This methodology is expected to aid rainfall-runoff modeling by allowing for direct and more accurate estimations of both runoff flow velocity and time of concentration. These data are required in physically based models of natural catchments that elaborate on the concept of variable contributing area [52, 53]. Specifically, the overland flow velocity drastically influences the portion of the contributing basin along with the distribution of the travel times of the water flow reaching the outlet [54]. Therefore, its accurate estimation may radically improve predictive capabilities of rainfall-runoff models and flow information garnered through the proposed instrumentation may inform the formulation of new models.

Along these lines, the capability to acquire distributed data on flow kinematics in natural watersheds is also expected to reinforce sheet-flow models for hillslope areas [55–57]. Such models are usually calibrated using experimental data obtained in laboratory conditions since traditional tracing methodologies do not allow for the acquisition of spatially refined field measurements that are representative of the ephemeral drainage networks present in hillslope areas [58–60]. Applications of such novel system also include non-contact discharge estimation and channel flow velocity [61–66], which are important parameters for modeling the response of natural catchments.

Beyond potential impact to fundamental hydrology, the envisioned instrumentation is expected to facilitate applied research and strengthen empirical procedures in hydraulic engineering and water management. With regards to overland flows, the calibration and performance assessment of widely used formulas, such as Chezy's, Darcy-Weisbach's, Manning-Strickler's, and Lawrence's formula, will benefit from the direct flow observations made possible by the proposed instrumentation [56]. Notably, these friction formulas tend to underestimate overland flow velocities as they are usually calibrated on runoff hydrographs in place of the actual travel time of the water in the drainage network [67], whose measurement will be enabled by the proposed tracer particles.

Similar benefits are anticipated to be observed in the calibration procedure of rating curves for discharge estimation in river cross-sections, where traditional measurement techniques are not applicable [68]. The proposed methodology is expected to have a broad impact on several other disciplines within the Earth science umbrella. In particular, the ability of automatically detecting fluorescent particles may be exploited in karst systems groundwater hydrology [69], sediment transport [17] and erosion research [6], and pollutants and chemical constituents diffusion and transformation [4].

1.3 Document organization

The rest of the dissertation is organized as follows. In Chapter 2, the feasibility of utilizing fluorescent particles for environmental flow tracing is investigated. Results in this Chapter are taken from [70]; at the time of the research, coauthor Dr. Matteo Aureli was a senior doctoral student who helped on the experimental design components based on mechatronics principles. In Chapter 3, we develop a particle tracking procedure based on image analysis to trace fluorescent particles in environmental applica-

tions. Flow measurements obtained from the procedure are compared to well-established experimental measurement techniques in fluid dynamics. This chapter's findings are taken from [71]; coauthor Mr. Christopher Pagano was an undergraduate student who fabricated the miniature water tunnel used for experiments. In Chapter 4, we propose the use of the fluorescent particles and the implementation of the tracking procedure in a natural mountainous stream to analyze the potential of the methodology in high flow rates and adverse illumination conditions. Results are summarized from [72]; at the time of the project, Mr. Andrea Petroselli was an Assistant Professor in Hydrology at University of Tuscia, who collaborated on the design of the experiments. An additional feasibility study conducted on a semi-natural hillslope is illustrated in Chapter 5, where the fluorescent particle tracers are implemented in heavily turbid flows and rainfall conditions. Findings presented in this Chapter are taken from [73]; Mr. Andrea Petroselli contributed on the design of the experimental site. In Chapter 6, we illustrate a procedure to synthesize eco-friendly fluorescent particles for environmental applications and provide a comprehensive characterization of the microstructure and fluorescence properties of the beads. Findings in this Chapter are based on [74–76]. Specifically, at the time of the research, Mr. Gabriele Mocio and Mr. Emiliano Rapiti were an undergraduate student and a Master student, respectively, whom I mentored on particle fabrication and feasibility experiments. Dr. Jafar F. Al-Sharab was an Industry Assistant Professor at New York University Polytechnic School of Engineering, who performed some of the microscopy analyses. In Chapter 7, we present large scale flow monitoring implementations where floating tracers and image-based analysis techniques are employed to provide noninvasive kinetic characterization of natural water bodies. Further, we discuss the integration of the proposed nonintrusive flow measurement technique in a miniature platform for aerial monitoring. At the time of the project, Mr. Christopher Pagano was a Master student, who worked on the design and development of the aerial vehicle. In Chapter 8, we address noninvasive flow pattern characterization and detection from a nonlinear manifold learning perspective, whereby a dimensionality reduction algorithm is applied to images depicting fluid flows at varying regimes. In Chapter 9, we report conclusions and contributions of this work and outline recommendations for future research directions.

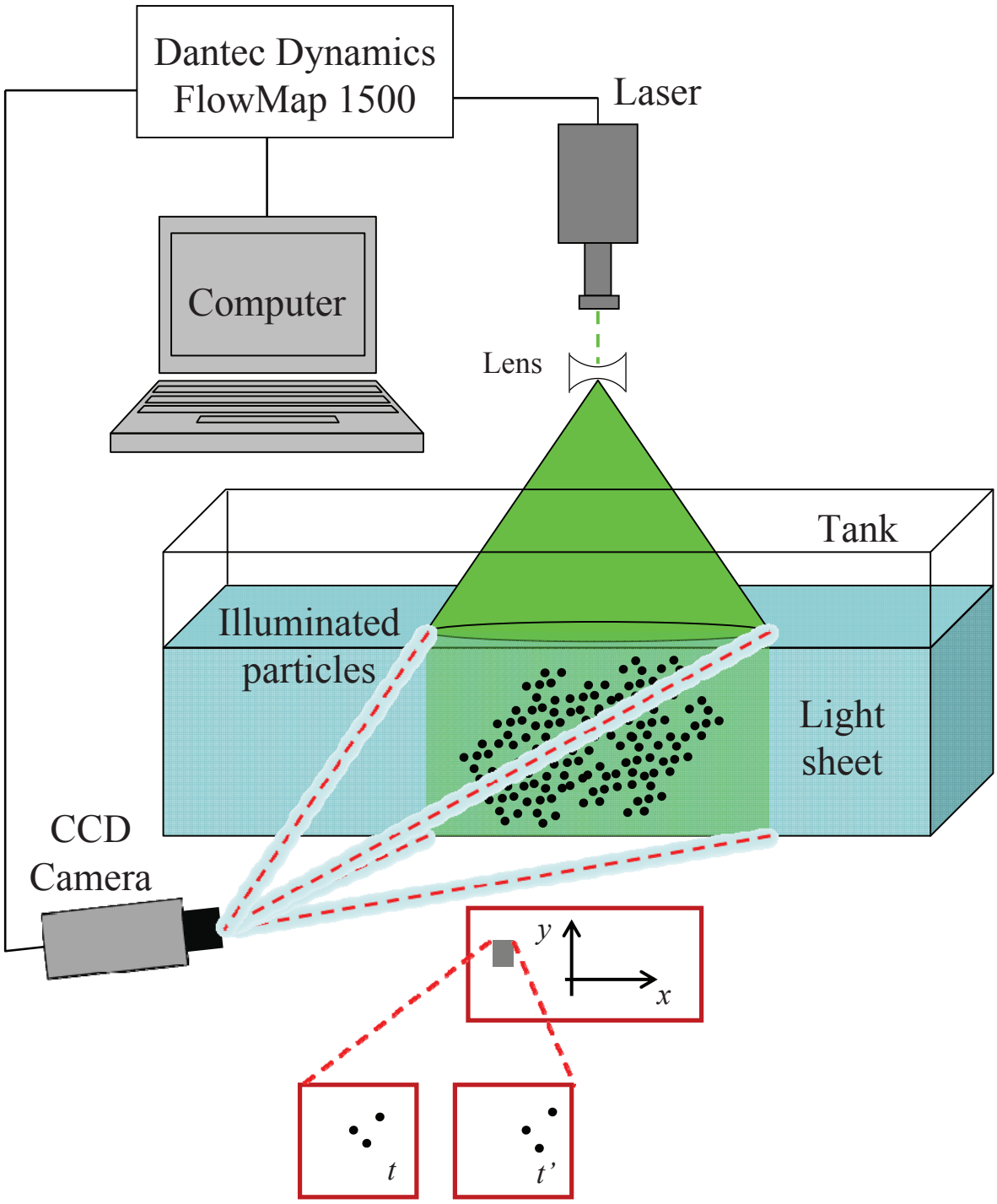

Figure 1.1: State of the art on hydrological tracers.

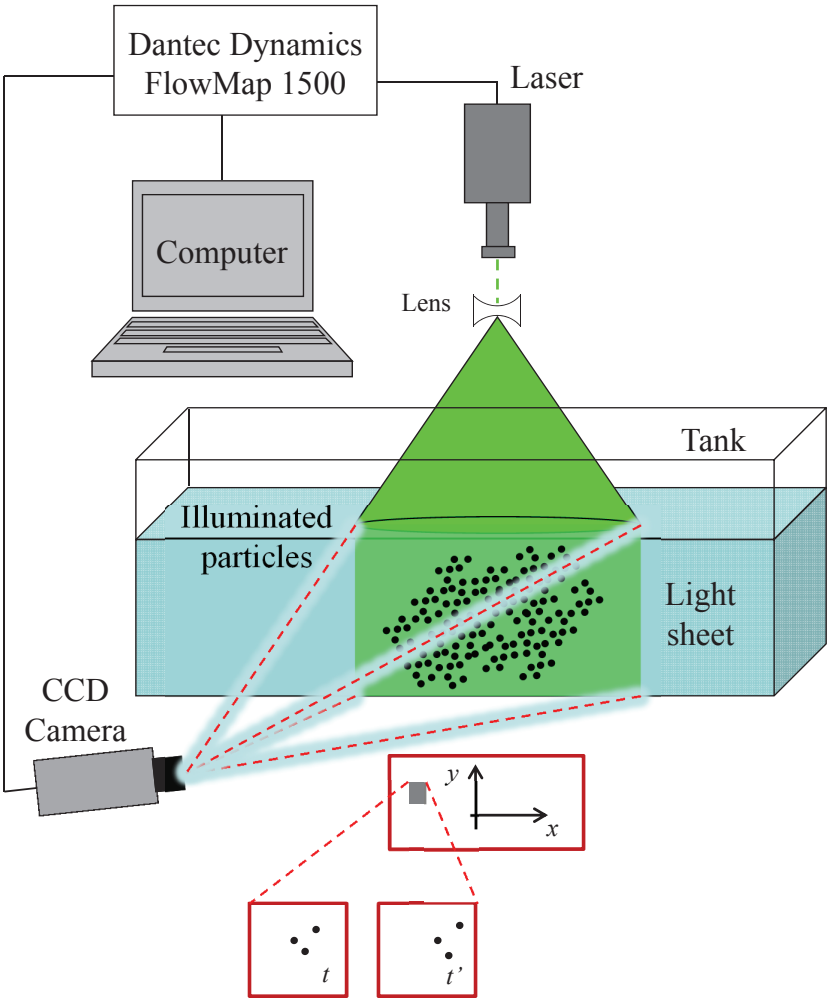

Figure 1.2: Typical experimental set-up for underwater PIV.

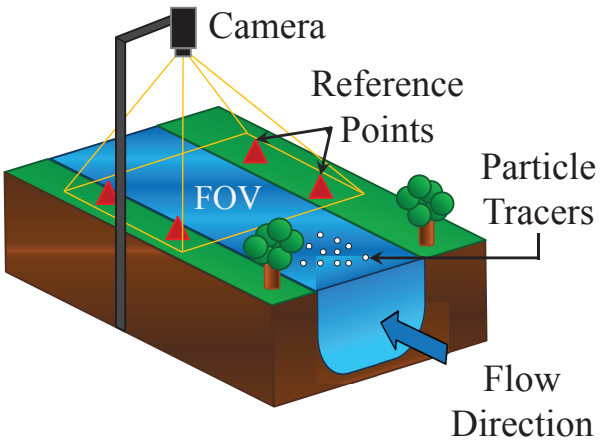

Figure 1.3: Sketch of a schematic LSPIV system.

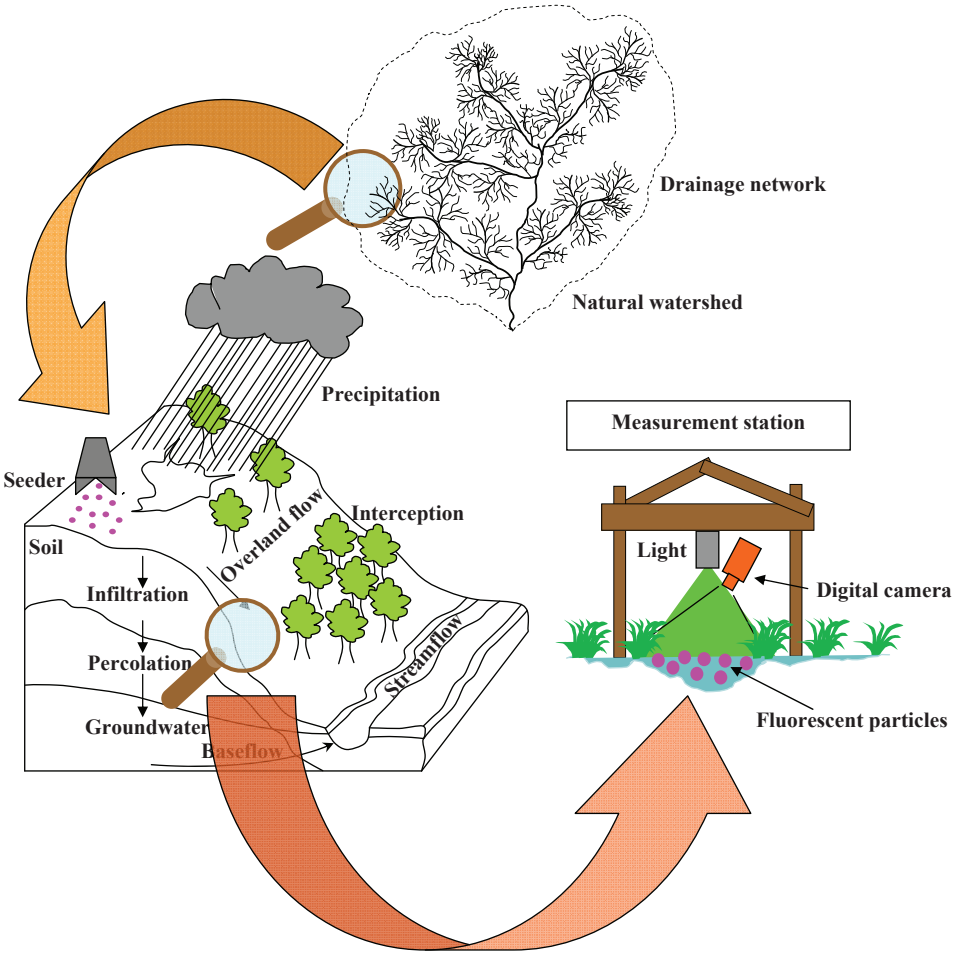

Figure 1.4: Schematic of the proposed instrumentation.

Chapter 2

Characterization of the visibility of buoyant fluorescent particles

2.1 Introduction and experimental methods

In this chapter, the feasibility of off-the-shelf buoyant fluorescent microspheres as particle tracers in turbid water flows is investigated. Microspheres' fluorescence intensity is experimentally measured and detected in placid aqueous suspensions of increasing concentrations of clay to simulate typical conditions occurring in natural hillslope drainage micronetworks. More specifically, experiments are conducted for different levels of clay concentration ranging from $0\,\mathrm{g/l}$ to $60\,\mathrm{g/l}$. The largest concentration corresponds to a remarkably high level of mountain-stream suspended sediment load, occurring during heavy floods [77]. Clay is selected for its fine size (10^{-6} to $10^{-11}\,\mathrm{m}$, see [78]) that results in high turbidity and slow sedimentation. Moreover, the particle visibility is studied at various immersion depths to account for the effect of turbulent flows which may tend to drag particles under the water surface, thus limiting their detectability [79, 80]. Measurements are performed by following two different schemes that provide a thorough understanding of the potential and limitations of commercial particle tracers in field observations. The former measurement method is based on direct fluorescence intensity measurement through an array of photoresistors; the latter scheme entails image-based detection of the considered beads. Additional information on particle performance and integration in low-cost measurement instruments for field observations is garnered through experiments conducted in an in-house developed miniature water channel. This experimental characterization aims at providing an assessment of off-the-shelf fluorescent beads performance in tracing high turbidity surface water flows.

The particles are purchased from Cospheric LLC [81] and their cost is approximately $100 for a $10\,\mathrm{g}$ sample; cost is reduced to $\$500/\mathrm{kg}$ for large batches. The beads are approximately spherical and their diameter is in the range of 0.710–$0.850\,\mathrm{mm}$, as displayed in the microscopy in Figure 2.1. The spheres are white under daylight and emit yellow-green light ($561\,\mathrm{nm}$ wavelength) if excited by a UV light

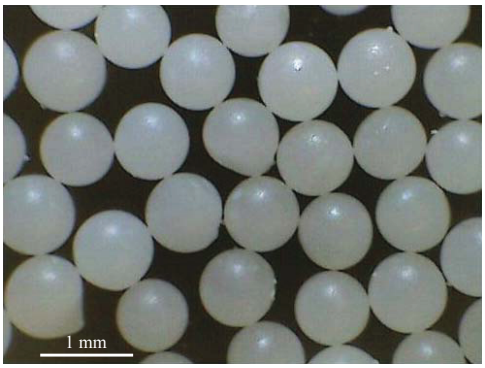

Figure 2.1: Particle microscopy showing size dispersion and system geometry.

source ($365\,\mathrm{nm}$ wavelength). The particle material is polyethylene and the fluorophore is embedded in the polymer matrix which allows for a long luminescence life-time. The particles nominal dry density is $0.99\,\mathrm{g/cm^3}$.

Particle fluorescence in a turbid water flow is characterized by using the experimental set-up in Figure 2.2(a). A set of 100 fluorescent particles are deployed in a plastic $5\,\mathrm{cm}$ diameter Petri Dish, thus covering a surface area fraction of the container of approximately 2.55%. The system consists of a voltage divider circuit placed $5\,\mathrm{cm}$ below the particle container and interfaced with a computer through a National Instruments NI USB-6221 Data Acquisition (DAQ) Board and an in-house developed Labview Virtual Instrument (VI). The circuit comprises an array of five PerkinElmer (St. Louis, MO, USA) VT900 photoconductive cells in parallel connection and one load resistor R_L in series to the photocells. A $540\,\mathrm{nm}$ filter is placed between the particle container and the photoresistors to isolate bead emissions from UV light. The slight mismatch between the particle emission and the filter wavelengths, $561\,\mathrm{nm}$ against $540\,\mathrm{nm}$, does not compromise the fluorescence intensity measurement. In addition, the experimental set-up is enclosed in a dark environment to avoid noise effects due to external light. The nominal resistance of each photoresistor under UV emission is on the order of $1\,\mathrm{M\Omega}$. Thus, a load resistance $R_L = 200\,\mathrm{k\Omega}$ is selected to match the array resistance and improve on the measurement sensitivity as per the voltage-divider configuration [82].

A Direct Current (DC) voltage of $5\,\mathrm{V}$ is applied to the series resistors to detect the change in resistance of the photoresistors under varying light intensity conditions. The voltage across the load resistor R_L is acquired at a sampling rate of $100\,\mathrm{Hz}$ and the resistance change is indirectly determined using [82]

$$V_{out} = \frac{R_L}{R_{Pr} + R_L} V_{in} \tag{2.1}$$

where V_{out} and V_{in} are the voltages measured and supplied through the DAQ board, respectively, and R_{Pr} denotes the resistance of the parallel connection of the photoresistors' array.

The use of a photoresistors' array against a single photoresistor is motivated by the need for reducing

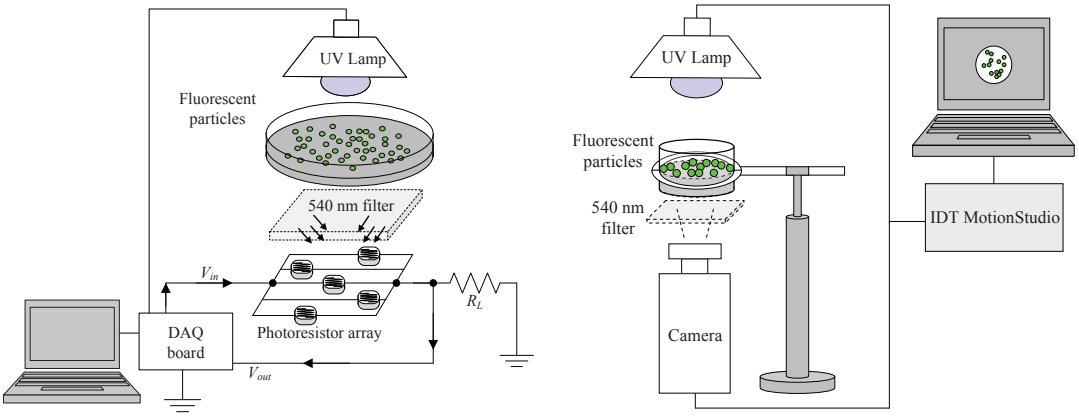

(a) (b)

Figure 2.2: Schematic of the measurement system for (a) characterization of particle fluorescence and (b) particle detection.

measurement noise and minimizing the effects of dishomogeneity in the particle dispersion within the Petri Dish. Furthermore, a fair repeatability of the experiments is guaranteed by maintaining the UV light at a constant distance of $5\,\mathrm{cm}$ from the sample and by placing an opaque separator between the lamp and the particle container. This allows the photoresistors to capture only the light that filters through the sample. Fluorescence characterization is performed in this test by selecting a constant level of the suspension in the container, that is, a constant particle immersion depth.

Results from the photoresistors' array can be validated by and complemented with data from image analysis techniques. In particular, information on particle location in the environment can be garnered by using image-based analysis tools. An IDT MotionPro 3 Series $1\,\mathrm{k} \times 1\,\mathrm{k}$ pixel color CMOS camera fitted with a $540\,\mathrm{nm}$ optical filter for image acquisition is placed below the particle container as displayed in Figure 2.2(b). The camera is placed at the constant distance of $30\,\mathrm{cm}$ below the particle container. Beads are illuminated by the UV lamp located $10\,\mathrm{cm}$ above the particles. An opaque separator is also inserted between the lamp and the container to avoid light that does not filter through the sample to be captured by the camera. In addition, the camera experimental set-up is also enclosed in a dark environment to avoid noise due to surrounding light sources. Images of increasing concentrations of clay-water suspensions are collected by the camera at a sampling frequency of $5\,\mathrm{Hz}$ and with an exposure time of approximately $0.2\,\mathrm{s}$. These parameters, along with image settings as brightness, contrast, and gamma correction, are kept constant during the experiments to allow for a proper comparison among different concentrations. The ratio of the bead pixel area to the analyzed frame area in the camera experimental set-up is kept equal to 2.55% to allow for a fair comparison with findings from particle fluorescence measurements.

In addition to the information provided by the use of photoresistors, the camera-based system allows for visual bead identification and localization in the area of interest. Particle size and shape can be recognized by using traditional image processing tools, such as edge detection [83]. Furthermore, infor-

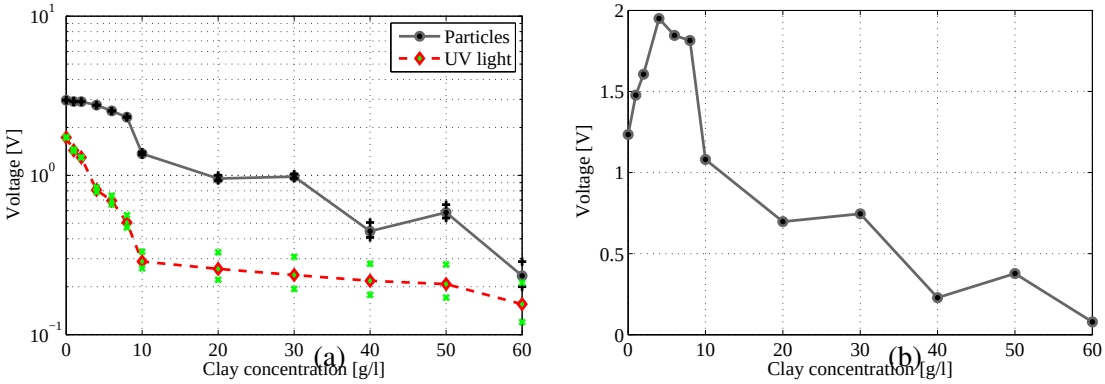

Figure 2.3: (a) Particle fluorescence and UV light intensity for increasing clay concentrations and (b) corresponding difference between photoresistors' response to particle and UV light intensity.

mation on the presence of fluorescent features can be obtained by analyzing the digital image histogram, that is, the discrete function $h(c_k) = n_k$ where c_k is the k-th intensity level and n_k is the number of pixels in the image whose intensity level is c_k, see [83].

2.2 Results

Particle fluorescence is measured by using the photoresistors' array. Experiments are conducted by varying the clay concentration while holding constant the number of particles to 100 and the immersion depth to $4\,\mathrm{mm}$. For each experiment at a given concentration, two or three independent measurements consisting of voltage data sampled at $100\,\mathrm{Hz}$ in nine seconds are collected and analyzed to provide statistical significance. More specifically, for each set of 900 samples, a mean value is computed and further averaging of these mean values yields the photoresistors' array output voltage displayed in Figure 2.3(a). In Figure 2.3(a), the black solid line represents the photoresistors' output voltage when the UV light illuminates both the suspension and the particles. The dashed red line shows the output voltage when the UV light illuminates only the clay suspension in the absence of particles. Black and green markers in the plot identify maximum and minimum average values from each experiment. As the clay concentration increases, less light is transmitted through the suspension and the recorded output voltage decreases. Voltage values corresponding to the UV light intensity, shown as a dashed red line, decrease with clay concentration, exhibiting a trend similar to the trend relative to the particle intensity, displayed as a solid black line. In Figure 2.3(a), the dashed red line is always below the curve corresponding to particle fluorescence, demonstrating that the beads can be sensed at every clay concentration. For further analysis, the difference between particle and light intensity is plotted in Figure 2.3(b). The peak of the curve corresponds to a $4\,\mathrm{g/l}$ clay suspension.

Two additional experiments are performed to estimate the influence of reflections and scattering

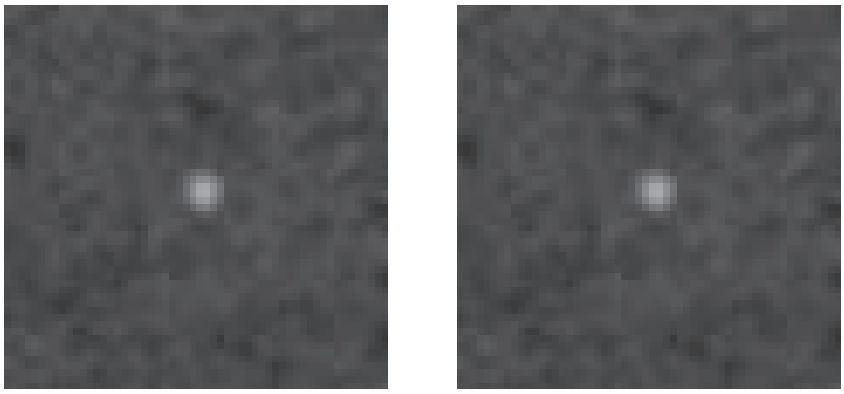

(a) (b)

Figure 2.4: Fluorescent particle in (a) clear and (b) turbid water.

from the container on the overall visibility of the beads. In the first experiment, the photoresistors' response to UV light in presence of the empty Petri Dish, is measured. In the second experiment, the photoresistors' response to particle fluorescence is measured by deploying 100 beads in the empty dish. The difference between the two output voltage signals is approximately equal to $0.86\,\mathrm{V}$, not shown in Figure 2.3(b). This value is lower than the value $1.2\,\mathrm{V}$ in Figure 2.3(b) corresponding to $0\,\mathrm{g/l}$, indicating that the presence of water magnifies the particle visibility.

Particle detection is performed by using the image-based experimental set-up. In this arrangement, a single particle is introduced in the Petri Dish for vision-based analysis. Particle detection is performed while varying both the clay concentration and the bead immersion depth. In clear water conditions, geometrical and optical characteristics of the system yield a typical bead reference frontal area of 9×9 pixels. The size of the analyzed image is then set at 56×56 pixels to keep a constant ratio of particle area to frame area approximately equal to 2.55%. A total of ten frames is recorded for each concentration and immersion depth and one randomly selected image is processed. Additionally, so-called background frames are collected by acquiring pictures of the clay suspension without fluorescent particles.

Figure 2.4 shows two representative images from the experimental campaign displaying the particle in clear and turbid water conditions. More specifically, Figure 2.4(a) shows the fluorescent bead in a clear water suspension at an immersion depth of $4\,\mathrm{mm}$. It can be noted that the particle pixel area is approximately equal to the reference area. On the other hand, Figure 2.4(b) displays the particle in a $1\,\mathrm{g/l}$ clay-water suspension at a depth of $6\,\mathrm{mm}$. The effects of clay and depth result into spreading of the bead boundaries in the image. This is mainly due to clay particles in the proximity of the bead scattering the fluorescence emissions. As a result, fluorescent spheres appear larger in the second image. On the other hand, fluorescent particles suspended in low clay concentrations and shallow depths appear smaller and with sharper boundaries as compared to turbid water conditions. In the former case, images show a meagre number of clear pixels with respect to the background frames.

The analysis of the particle visibility in turbid water is qualitatively conducted by utilizing his-

tograms obtained from 8-bit gray-scale frames. Accordingly, 256 classes of intensity are considered. The 8-bit gray-scale image is extracted from the original RGB (red, green, blue) picture by retaining only the green channel [83]. Figure 2.5 reports histograms pertaining to particle frames and corresponding backgrounds in Figure 2.4. Note that histogram bins related to low intensity classes refer to darker colors in the images. Bins corresponding to higher intensity classes may instead be ascribed to the presence of fluorescent particles.

Figure 2.5(a) and (c) represent the background and particle frame histograms, respectively, for clear water conditions. Figure 2.5(b) and (d) display the background and particle frame histograms for the $1\,\mathrm{g/l}$ suspension. The insets magnify low pixel count bins. By comparing these insets, it can be noted that Figures 2.5(c) and (d) present non-zero pixel counts at higher intensity classes. This effect is due to the presence of the fluorescent particle and therefore represents the fluorescent emissions. In particular, the inset in Figure 2.5(d), corresponding to the turbid concentration, displays non-zero pixel counts at intensity classes around 100–120. Conversely, the inset for clear water in Figure 2.5(c), depicts non-zero counts up to the neighborhood of class 150. This can be attributed to bead boundaries spreading in turbid water. On the other hand, background histograms in Figures 2.5(a) and (b) show peaks that are slightly shifted towards brighter classes when compared to their counterparts in Figures 2.5(c) and (d). This phenomenon is likely due to light scattering through clay particles. In addition, the peak in Figure 2.5(c) is higher than the corresponding one in the background frame, as shown in Figure 2.5(d).

Information from histograms can be lumped into appropriate global parameters to quantify the particle visibility against the background, including the effective particle boundary spreading and brightness. More specifically, the following index $\mathscr{G}$ is adopted to synthetically describe the effect of fluorescence on the overall frame tonal distribution:

$$\mathscr{G} = \frac{\sum\limits_{i \in \mathscr{I}} c_i n_i}{\sum\limits_{i \in \mathscr{I}} n_i}, \quad \mathscr{I} = \{i \in \{0, 1, ..., 255\} : n_i > 0\} \tag{2.2}$$

with

$$n_i = n_i^p - n_i^b. \tag{2.3}$$

Here, c_i represents the intensity classes from 0 to 255 and n_i the pixel count on each class of the histogram obtained by subtracting the background, that is, n_i^b, from the particle frame, that is, n_i^p, and including in the summation only the classes with positive pixel counts. Tones corresponding to the particle are expected to be in the higher intensity classes, while background pixels pertain to darker classes. By subtracting n_i^b from n_i^p, positive and negative pixel counts are expected to occur for brighter and darker classes, respectively. Therefore, by discarding negative pixel counts, the particle average intensity tone is identified. For instance, by subtracting the background, see Figures 2.5(a) and (b), to the particle frame, Figures 2.5(c) and (d), the particle is automatically isolated from the background and its contribution to the frame tonal distribution is quantitatively estimated. It should be noted that

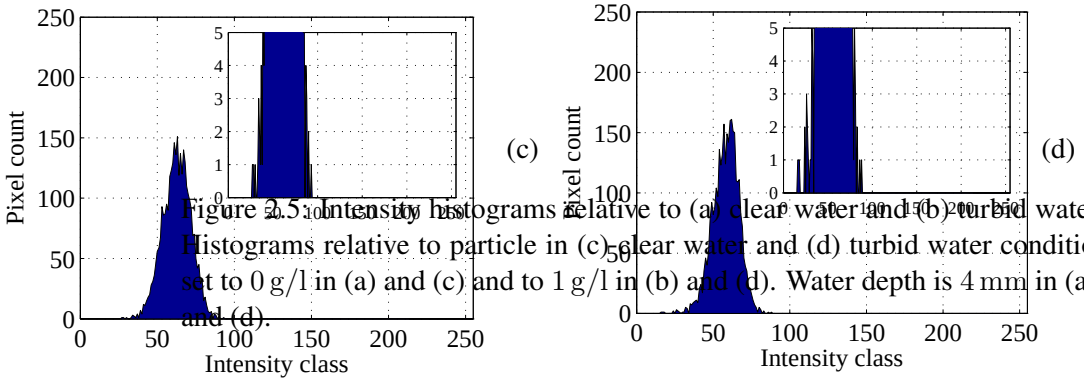

Figure 2.5: Intensity histograms relative to (a) clear water and (b) turbid water condition backgrounds. Histograms relative to particle in (c) clear water and (d) turbid water condition. Clay concentration is set to $0\,\mathrm{g/l}$ in (a) and (c) and to $1\,\mathrm{g/l}$ in (b) and (d). Water depth is $4\,\mathrm{mm}$ in (a) and (c) and $6\,\mathrm{mm}$ in (b) and (d).

analogous background subtraction techniques find also application in the detection of boundaries of moving shapes, as discussed for example in [84, 85]. The index $\mathscr{G}$ is expected to increase for high clay concentrations, where the bead boundaries tend to spread, thus resulting in larger pixel counts at brighter tones. In addition, note that the index $\mathscr{G}$ is highly dependent on the background illumination conditions and color homogeneity.

In Figure 6.11(a), the index $\mathscr{G}$ is evaluated for increasing clay-water concentrations at the bead immersion depth of $6\,\mathrm{mm}$. The parameter is minimized for clear water since the particle is very defined and its area comprises only a few pixels. On the other hand, as the turbidity increases, the number of brighter pixels increases and the index varies accordingly. The behavior shown in Figure 6.11(a) displays qualitative similarities with the experimental evidence collected from the fluorescence measurements. In particular, when comparing Figures 2.3(b) and 6.11(a), it can be noted that the output voltage and the index $\mathscr{G}$ present a peak at the same concentration of $4\,\mathrm{g/l}$. At very large concentrations, the index tends to increase due to the effect of the bead boundaries spreading, whereas the output voltage decreases as

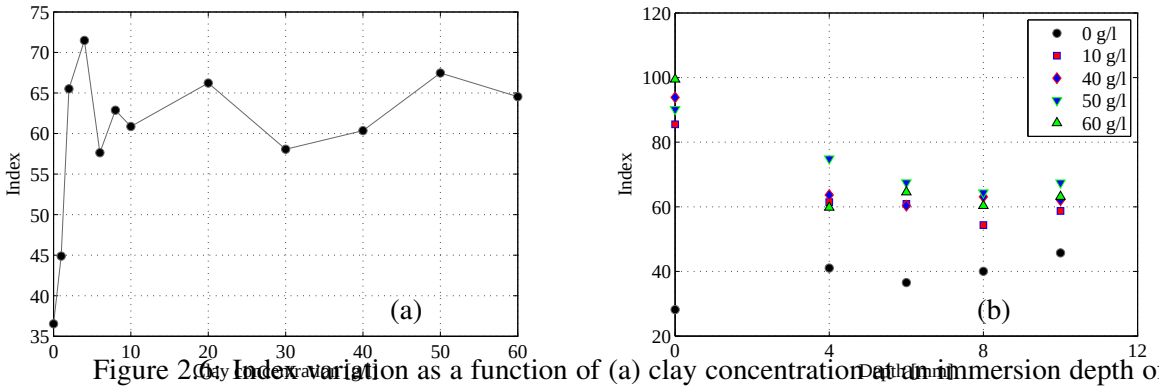

Figure 2.6: Index variation as a function of (a) clay concentration at an immersion depth of $6\,\mathrm{mm}$ and (b) bead immersion depth.

the photoresistors excitation level decreases.

In Figure 6.11(b), $\mathscr{G}$ is estimated for selected concentrations at varying bead immersion depths. It is here noted that different concentrations display a comparable behavior in the bead boundary spreading. As the turbid layer becomes thicker, the number of brighter pixels tends to increase. In addition, the effect of immersion depth on the visibility is similar to the increase in clay concentration.

Index values at the depth of $0\,\mathrm{mm}$ are also reported in Figure 6.11(b). In this case, data are obtained by positioning both the UV lamp and the camera at the relatively large distance of $40\,\mathrm{cm}$ above the sample. This selection simulates a practical implementation of the detection system for in-situ applications. Note that index values corresponding to depths of $0\,\mathrm{mm}$ tend to cluster around high intensity classes. However, the value of $\mathscr{G}$ that refers to clear water is much smaller than numerical values found in turbid water scenarios, due to effects of reflections in water. Indeed, in clear water, reflections produce a relatively large number of pixels which are as bright as the particle pixels and contribute to the reduction of $\mathscr{G}$.

Chapter 3

Buoyant fluorescent particles for shallow water flow measurements

3.1 Introduction

This chapter seeks to demonstrate and extend the use of off-the-shelf fluorescent particles in tracing shallow water flows in illuminated ambient conditions. In such severe conditions, the global index used in [70] to detect particles in illuminated conditions is not applicable and dedicated strategies need to be devised. The suitability of such particles in tracing water flows is theoretically assessed by conducting a parametric study where particle response to different flow velocities is computed through the Basset-Boussinesq-Oseen equation (BBO). An automated image analysis-based procedure is then implemented for automatic detection and real-time tracking of fluorescent particles in water flows and illuminated conditions. Particles are recorded as they transit in a custom-built reclinable miniature channel specifically developed for simulating shallow water conditions. The image processing scheme is based on a computationally inexpensive correlation algorithm between recorded video frames and a particle template image. The procedure allows for adjusting the template dimensions and intensity tones according to the particular experimental conditions and thus guarantees good versatility of the tracking algorithm. Additionally, particle velocities as extracted from the image analysis process are compared to PIV measurements for selected combinations of slopes and water depths in the water channel to validate the overarching approach.

The proposed methodology may be successfully integrated in tracing technologies for hillslope overland flow velocity measurements for its limited cost and versatility as compared to more complex flow measurement systems, that require massive hardware components and extensive in situ calibration. Findings in this work demonstrate that this approach can be used for real time water flow characterization in adverse conditions, such as illuminated environments and shallow water depths, and for moderately fast water flows, as high as 1 m/s.

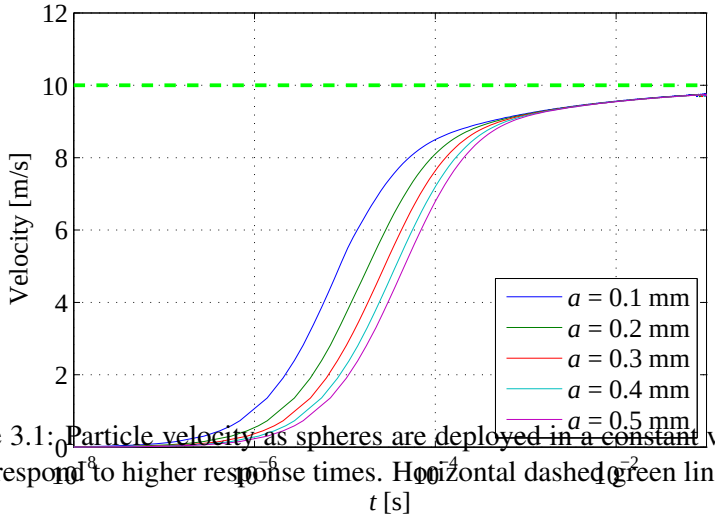

Figure 3.1: Particle velocity as spheres are deployed in a constant velocity flow. Increasing diameters, a, correspond to higher response times. Horizontal dashed green line refers to the carrier flow.

3.2 Parametric analysis of particle motion

A preliminary analytic study is conducted to assess the particles' suitability in tracing different flow regimes. More specifically, the BBO [79, 86–88] equation is here used to describe the bead dynamics in a time-varying and spatially uniform flow. The particle initial velocity is always set along the flow direction, so that the BBO reduces to a scalar integrodifferential equation with respect to the time variable t. The particle Reynolds number is assumed to be small so that the drag force on the sphere can be expressed according to Stokes' law [87]. The particle volume fraction that is not submerged in water is approximately equal to one hundredth the bead total volume and therefore, the classical BBO can be applied without further modifications, see for example [89]. Along the direction of flow, the BBO determines the evolution of the particle Lagrangian y velocity U_p as a function of the time-varying flow velocity U_f. This reads

$$\begin{aligned}\frac{4\pi}{3}a^3\rho_p\frac{\mathrm{d}U_p}{\mathrm{d}t} &= \frac{4\pi}{3}a^3\rho_p F(U_f-U_p)+\frac{4\pi}{3}a^3\rho_f\frac{\mathrm{d}U_f}{\mathrm{d}t}\\ &+\frac{1}{2}\frac{4\pi}{3}a^3\rho_f\frac{\mathrm{d}(U_f-U_p)}{\mathrm{d}t}+6a^2\sqrt{\pi\rho_f\mu}\int_{t_0}^{t}\frac{\frac{\mathrm{d}(U_f-U_p)}{\mathrm{d}\tau}}{\sqrt{t-\tau}}\mathrm{d}\tau\end{aligned} \tag{3.1}$$

with proper initial condition of the form $U_p(t_0) = U_{p0}$. In Eq. (3.1), ρ_p and ρ_f are the particle and carrier fluid densities, respectively; a denotes the particle radius; μ is the fluid viscosity; and t_0 is the initial time. The term F is the time constant for the momentum transfer due to drag force

$$F(t) = \frac{3}{8}C_D\frac{\rho_f}{\rho_p}\frac{1}{a}|U_f(t)-U_p(t)|, \tag{3.2}$$

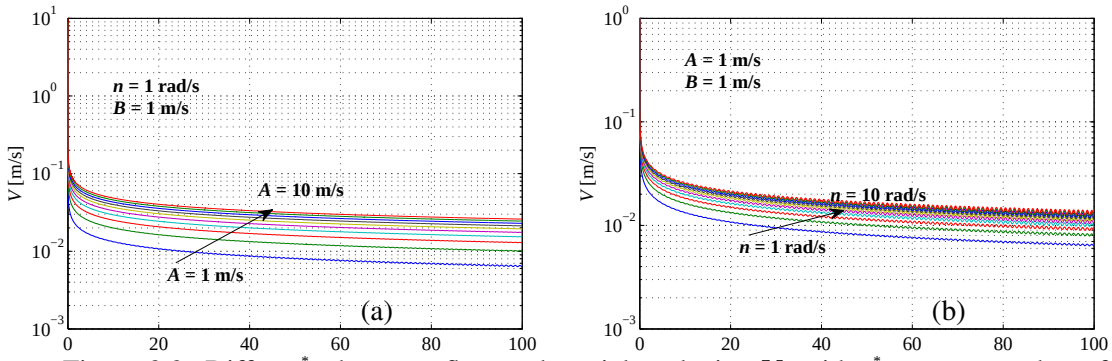

Figure 3.2: Difference between flow and particle velocity, V, with respect to number of time periods t/T^*. (a) A is varied from $1\,\mathrm{m/s}$ to $10\,\mathrm{m/s}$ with $B = 1\,\mathrm{m/s}$ and $n = 1\,\mathrm{rad/s}$; (b) n is varied from $1\,\mathrm{rad/s}$ to $10\,\mathrm{rad/s}$ with $A = 1\,\mathrm{m/s}$ and $B = 1\,\mathrm{m/s}$. Oscillations in the graphs correspond to the imposed values of n.

where C_D is the drag coefficient. In this study, the Oseen's approximation for the drag coefficient,

$$C_D = \frac{24}{N_{Re}}\left(1 + \frac{3}{16}N_{Re}\right) \tag{3.3}$$

is used, see for example [87]. Here, the particle Reynolds number, N_{Re}, is defined as $N_{Re} = (2a)V\rho_f/\mu$ where $V = U_f - U_p$.

The left-hand side term in Eq. (3.1) is the inertia of the sphere; the first term on the right-hand side is the drag force exerted on the particle by the carrier fluid; the second term on the right-hand side is due to a pressure gradient in the fluid that equals $\rho_f \frac{\mathrm{d}U_f}{\mathrm{d}t}$ since the flow is uniform, see for example [90]. The third term on the right-hand side in Eq. (3.1) refers to the force required to accelerate the apparent mass of the sphere moving in the fluid while the fourth term on the right-hand side, the Basset effect, accounts for the influence of the history of the particle velocity [42, 91–93].

Equation (3.1) is solved by assuming an expression for the flow velocity profile $U_f(t)$ and by setting the initial condition $U_p(t_0) = 0$. The explicit Runge-Kutta method of variable order (4,5) is used for the integration. The Basset term is approximated with the expression provided in [93–95], that is, $\int_{t_0}^{t} \frac{\mathrm{d}V}{\mathrm{d}\tau}\frac{\mathrm{d}\tau}{\sqrt{t-\tau}} \approx \frac{V(t)-V(t_0)}{\sqrt{0.5(t-t_0)}}$. This expression is derived from the mean value theorem for definite integrals by evaluating the integrand at $\tau = 0.5(t - t_0)$, that is, at the midpoint of the domain.

A representative plot of the sphere velocity as it is deployed in a constant velocity flow, with nought initial speed, is depicted in Figure 3.1. In this case, Eq. (3.1) is integrated in the time interval $t \in [0\,\mathrm{s}, 0.1\,\mathrm{s}]$ to capture the particle response time to a constant flow velocity. It is noted that, for a constant particle density, reducing the particle size decreases the response time, that is, the time the bead takes to reach $U_p = 0.9U_f$ from $U_p = 0$. The response time of the selected fluorescent particles, $a = 0.4\,\mathrm{mm}$,

in a constant flow of $10\,\mathrm{m/s}$ is of the order of $10^{-3}\,\mathrm{s}$.

A parametric study is conducted to assess the efficiency of the particle in tracing water. Specifically, Eq. (3.1) is solved by prescribing the flow velocity function $U_f(t) = A + B\sin nt$, where A represents the mean value of the flow velocity whereas B and n indicate the amplitude and frequency of the oscillation about its mean, respectively. The parameters are selected to vary the flow velocity from $1\,\mathrm{m/s}$ to $10\,\mathrm{m/s}$. The BBO is solved for representative combinations of A, B, and n and time traces of V are plotted against the number of time periods t/T^*, where $T^* = 2\pi/n$, in Figure 3.2. In Figure 3.2(a), the difference between the flow and the particle velocity tends to rapidly decrease in the time horizon of ten periods when A varies from $1\,\mathrm{m/s}$ to $10\,\mathrm{m/s}$ and B and n are held constant to $1\,\mathrm{m/s}$ and $1\,\mathrm{rad/s}$, respectively. Note that V does not decrease monotonically and shows a variation in time synchronous with the time variation of the carrier fluid, that is, at the radian frequency $n = 1\,\mathrm{rad/s}$. A similar behavior is displayed in Figure 3.2(b) where the oscillation frequency is varied from $1\,\mathrm{rad/s}$ to $10\,\mathrm{rad/s}$.

These results are representative of very extreme scenarios in which the flow is rapidly varying over time and are thus a solid evidence for the feasibility of inferring carrier flow speed from the particle motion. It is noted that a cruder estimate of the bead capability to trace a flow can be drawn through the relaxation time, $\tau_s = (2a)^2\rho_p/(18\mu)$ as defined in [40]. For the considered beads, this is approximately equal to $\tau_s = 3.5 \times 10^{-2}\,\mathrm{s}$ which suggests that particles can be well suited to trace flows whose time scale of variation is considerably larger than τ_s or, similarly, that tracing a background flow of a given constant speed using particles deployed from rest requires an elapsed time considerably larger than τ_s. Although this value is several order of magnitudes larger than the time of relaxation of typically used PIV particles [42], the parametric analysis in Figure 3.2 demonstrates that fluorescent beads can be successfully used as tracers for uniform flows.

3.3 Particle tracking

The automated detection and real-time tracking of the fluorescent particles in flowing water and illuminated environment conditions is achieved by using inexpensive video acquisition equipment for recording the particle motion as it travels in a custom-built miniature channel. After acquisition, videos are converted to frames and subsequently analyzed through an in-house developed image analysis-based algorithm that automatically identifies the particle in the pictures and tracks its trajectory through the channel. The algorithm is developed in a MATLAB environment [96].

The procedure takes advantage of the known shape of the particle as it appears in the frames, see Figure 3.3(a), and implicitly assumes that the particle follows a rectilinear trajectory towards the direction of flow as it crosses the area of interest, approximately equal to $20\,\mathrm{cm} \times 10\,\mathrm{cm}$. The characteristic oblate shape of the bead is due to the specific acquisition frequency of the Canon camcorder that is only $30\,\mathrm{Hz}$.

The algorithm is based on the correlation between a template image and frames extracted from the

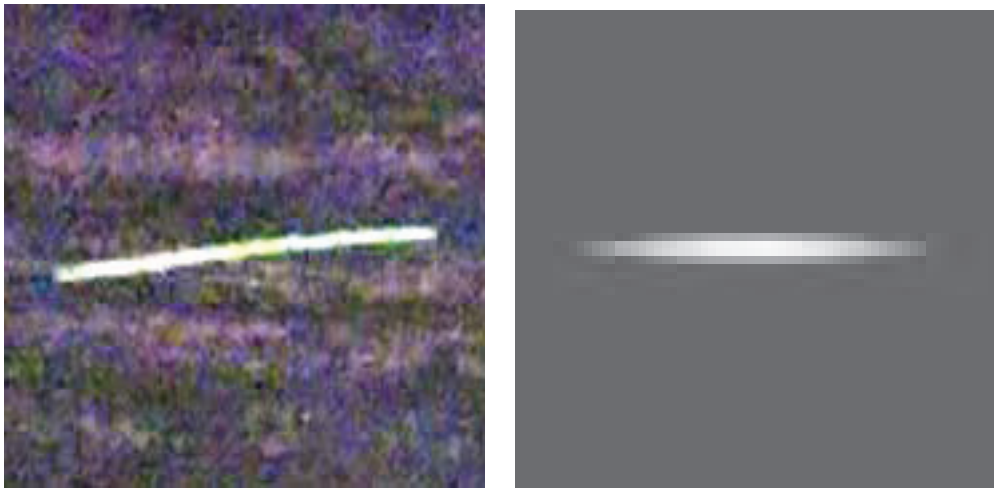

(a) (b)

Figure 3.3: (a) Representative bead shape as recorded by the Canon camcorder; and (b) artificial template.

videos. The sole green channel out of the extracted RGB frames is processed since the majority of the bead emissions is green when excited by the UV light. For reference, an artificial template that represents an ellipse against a gray tone background is generated, see Figure 3.3(b). A cartesian reference system centered in the ellipse's geometric center and aligned with its axes is introduced to describe the pixel position (κ, λ) in the artificial template. The ellipse major and minor axes are determined by averaging the pixel width and height of the particles as they appear in frames of available experiments or data taken during calibration. The pixel intensities within the ellipse are graded from white tones in the center to the background tone to account for the diffusion of particle's boundaries in the image [70]. Within the ellipse, the graded intensity is a function of pixel position as

$$\mathscr{I}(\kappa, \lambda) = 1 - \left[\frac{\kappa^2}{h^2} + \frac{\lambda^2}{w^2}\right]. \tag{3.4}$$

Here, h and w are the ellipse pixel semi-height and width. After proper rescaling and offsetting of the data obtained from Eq. (3.4), the pixel intensity is discretized and converted to gray scale tones. For simplicity, the artificial ellipse's dimensions $2h$ and $2w$ are kept constant to the average dimensions of the bead from the entire set of images acquired in this study where particles are present, that is, approximately 120 pixel $\times 10$ pixel. Consistently, the background nuance is fixed at the average intensity of the green channel of the recorded images' background, that is, class 76 out of the 255 gray intensity classes. The maximum intensity at the ellipse's center is 255 and the overall size of the artificial template is $l \times l$ pixel, where l is taken as 180. Notably, the template size corresponds to only 1.5% of the overall image area.

A statistical study is conducted to test the sensitivity of the correlation procedure to the artificial

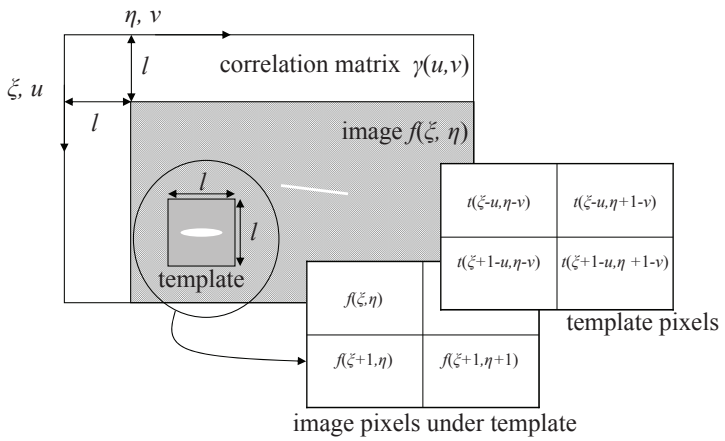

Figure 3.4: Sketch of the mechanism of correlation between particle image and template. The correlation matrix dimensions exceed the image size by the template edge that equals l pixels.

template dimensions and intensity tones. The test is performed by first correlating the artificial bead with frames where the particle is present and then by repeating the procedure with frames where the particle is absent. Frames are extracted from videos recorded for combinations of seven different values of the slope α and six water depths d. Two videos are taken for each condition.

The procedure is based on using the following normalized correlation γ_t between the image and a selected template, see [97],

$$\gamma_t(u,v) = \frac{\sum_{\xi,\eta}[f(\xi,\eta) - \bar{f}_{u,v}][t(\xi-u,\eta-v) - \bar{t}]}{\sqrt{\sum_{\xi,\eta}[f(\xi,\eta) - \bar{f}_{u,v}]^2 \sum_{\xi,\eta}[t(\xi-u,\eta-v) - \bar{t}]^2}} \tag{3.5}$$

where (u,v) is the coordinate system in the correlation matrix and (ξ,η) indicate the pixel position in the image, see Figure 3.4. In Eq. (3.5), $f(\xi,\eta)$, and $t(\xi,\eta)$ are the image and the template intensities as function of the pixel position (ξ,η), and $\bar{t}$ and $\bar{f}_{u,v}$ are the average template intensity and the average intensity of the image portion overlapping the translating template, respectively. The template size is always kept to a square of l pixels and when the artificial template is used κ and λ are aligned with ξ and η. The maximum correlation coefficient $\Gamma_{\max}$ for each frame is collected and displayed in Figure 3.5(a) where data are fitted with Weibull distributions [98]. Table 3.1 reports the scale and shape parameters for the fittings as well as distributions' mean and standard deviations. As expected, frames where the particle is present display higher correlation values. Note that the separation between frames with and without the particles is manually executed.

The correlation analysis can be further sharpened by preprocessing the images from experiments by a background subtraction as displayed in Figure 3.5(b) and corresponding entries in Table 3.1. The background subtraction procedure consists of a bottom-hat transformation [83], where the image is subtracted from its corresponding closing. Closing of the images is performed by a preliminary morpho-

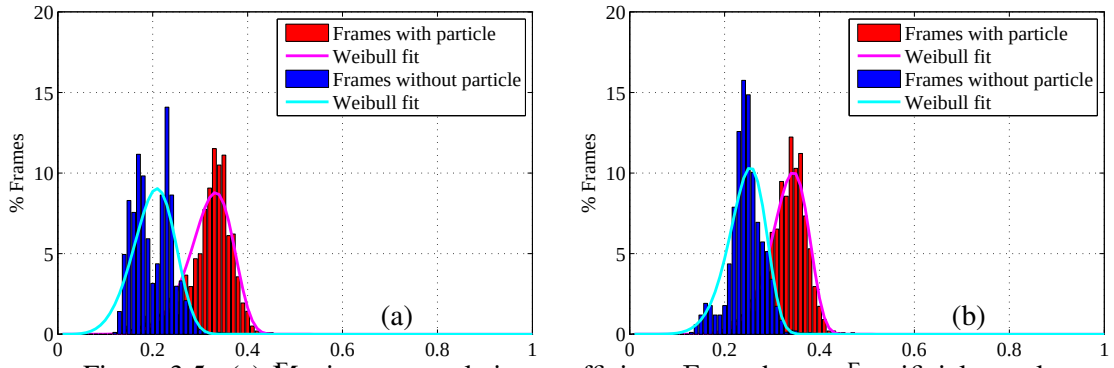

Figure 3.5: (a) Maximum correlation coefficient, $\Gamma_{\max}$, between artificial template and frames with particle (red) and without particle (blue); and (b) $\Gamma_{\max}$ between artificial template and frames with particle (red) and without particle (blue) in case of frame preprocessing with background subtraction fitted with Weibull distributions.

logical dilation and a successive erosion of the experimentally acquired picture by the artificial ellipse. More specifically, the image dilation through the template is obtained by translating the template over the image and then thickening the set of foreground pixels by adding the pixel intensity where the translated template overlaps some portion of the image foreground. On the other hand, erosion shrinks the image foreground by removing the pixel intensity where the translated template does not overlap any portion of the image foreground. These operations allow for simplifying the images by preserving their shape while eliminating irrelevant items, see also [99].

Table 3.1: Statistical summary for plots in Figure 3.5. Scale and shape parameters for the Weibull distribution fittings are reported as well as relative mean values and standard deviations. The acronym CDF indicates the Cumulative Distribution Function at $\Gamma_{\max} = 0.3$. Entries in the last two rows of the table refer to preprocessed images by background subtraction.

Correlation	**Scale**	**Shape**	**Mean**	**Standard Deviation**	**CDF** at $\Gamma_{\max} = 0.3$
With bead	0.34	8.02	0.32	0.05	31.92%
Without bead	0.22	5.25	0.20	0.04	99.54%
Preprocessed With bead	0.35	9.49	0.33	0.04	21.26%
Preprocessed Without bead	0.26	7.24	0.24	0.04	94.11%

The correlation introduced in Eq. (3.5) is used to perform the automatic detection and online tracking of the particle in the water flow according to the synthetic flowmap in Figure 3.6. The procedure consists of first performing the background subtraction described above on the acquired images and then computing γ_t in the entire image through Eq. (3.5) by using the artificial template. Additionally, the algorithm integrates a conditional updating procedure which allows for enhanced detecting performances. More specifically, after correlation with the first image of a video, the maximum correlation

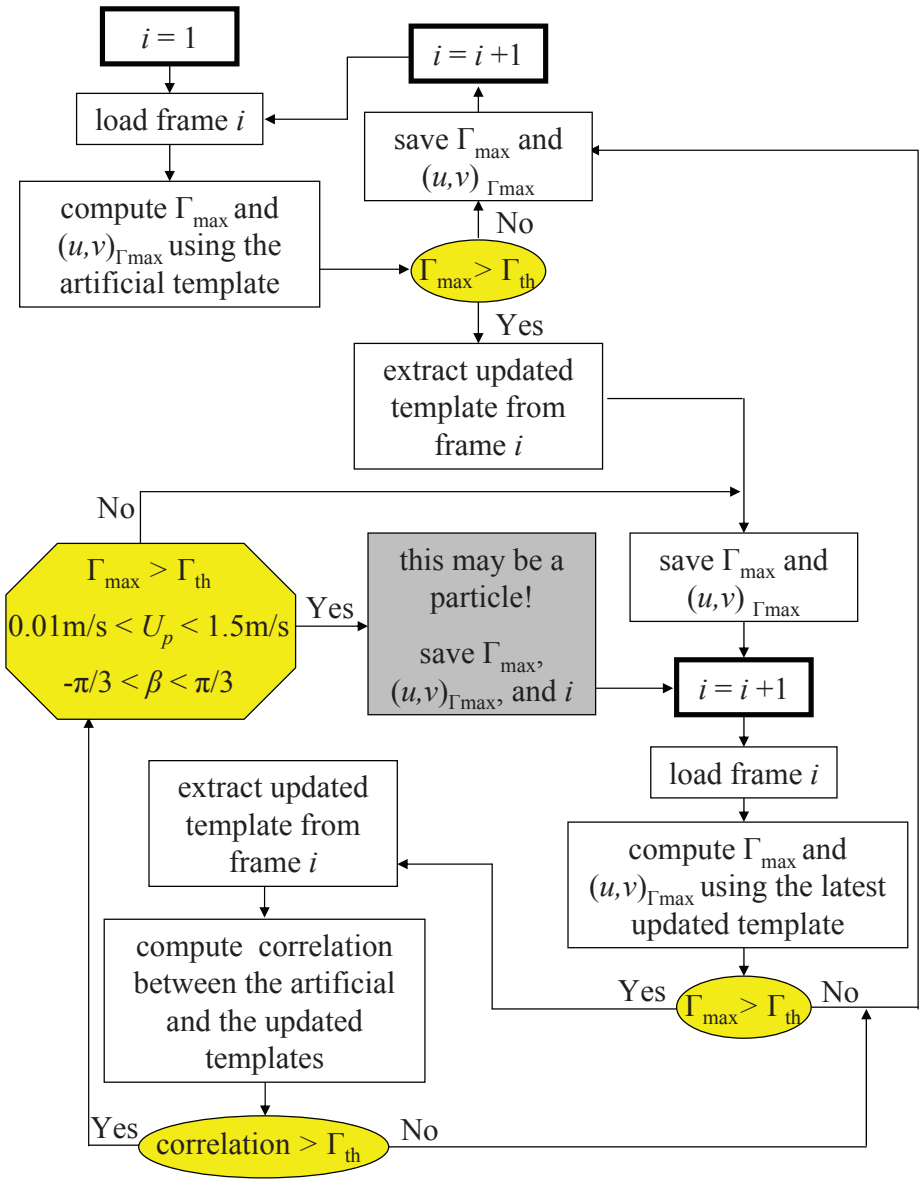

Figure 3.6: Synthetic flowmap of the tracking algorithm. At each iteration, the value of $\Gamma_{\max}$ along with its spatial coordinates $(u, v)_{\Gamma_{\max}}$ are saved.

coefficient is compared to an ad-hoc threshold value of $\Gamma_{\text{th}} = 0.3$. This value is selected based on results reported in Table 3.1, where it is shown that the mean correlation value relative to frames with particle is approximately equal to 0.3. If the value of the correlation coefficient obtained from Eq. (3.5) is greater than this threshold, a new template image is generated by cropping out of the previous image a square of dimension equal to l pixels centered about $(u, v)_{\Gamma_{\max}}$, where the maximum correlation is attained. The updated template is then used for correlation with the successive frame. It is observed that

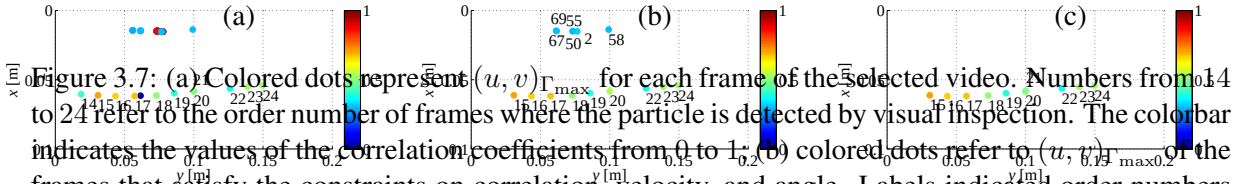

Figure 3.7: (a) Colored dots represent $(u, v)_{\Gamma_{\max}}$ for each frame of the selected video. Numbers from 14 to 24 refer to the order number of frames where the particle is detected by visual inspection. The colorbar indicates the values of the correlation coefficients from 0 to 1; (b) colored dots refer to $(u, v)_{\Gamma_{\max}}$ of the frames that satisfy the constraints on correlation, velocity, and angle. Labels indicated order numbers of the detected frames; and (c) colored dots represent $(u, v)_{\Gamma_{\max}}$ of frames after postprocessing labeled with their relative order number.

the values of $\Gamma_{\max}$ obtained by correlating the frames with the updated template are much higher than values obtained by using the artificial template. The value of $\Gamma_{\max}$ is compared to Γ_{th} at each step of the procedure and the coordinates of the maximum value of the correlation coefficient $(u, v)_{\Gamma_{\max}}$ that identify a possible location of the particle, if any is present.

The procedure of template updating is verified at each step of the algorithm by computing the cross-correlation between the updated template and the artificial template as they are overlapped. That is, Eq. (3.5) is computed with the update and artificial template taking the place of f and t and (u, v) selected at the templates' center. If the cross-correlation falls under Γ_{th}, the updating process is discarded and the artificial template is used to identify the bead location. This condition reduces biases in the updating methodology due to the presence in the images of objects similar to the bead in their shape and intensity.

Additionally, the algorithm encompasses the automatic and online detection of the particle as it flows in the channel. More specifically, when a value of $\Gamma_{\max} > \Gamma_{\text{th}}$ is obtained from the correlation with the updated template, the location where the maximum correlation is attained $(u, v)_{\Gamma_{\max}}$ is first considered as a potential particle. The velocity of the potential particle in the plane is estimated by collecting the values of $(u, v)_{\Gamma_{\max}}$ in the frame sequence and multiplying them by a scale factor to obtain metric units. The in-plane components of the velocity are calculated by taking the inverse of the camcorder acquisition frequency as the time interval. Furthermore, the angle between the line connecting $(u, v)_{\Gamma_{\max}}$ in the present frame and $(u, v)_{\Gamma_{\max}}$ in the previous frame and the y-axis is computed. If the value of the velocity is comparable to admissible flow velocities, the tracked point is more likely to pertain to a particle flowing in the channel. Since the flow is assumed to be uniformly developed in the positive direction of the y-axis, the angle between two successive particles is predicted to lie in a certain range. It is noted that velocity and angle ranges are regarded as input parameters to the algorithm therefore they can be adjusted to the specific flow regime of interest. In these experiments, feasible flow velocities are imposed by the inherent characteristics of the minichannel, that is, $0.01\,\text{m/s} \leq U_f \leq 1.5\,\text{m/s}$.

More specifically, only nonnegative velocity values, and therefore velocities that are not in the opposite direction of the flow, are considered in the average. In addition, values of the velocity that are higher than $1.5\,\mathrm{m/s}$ are discarded in the final estimation. This constraint allows for eliminating possible jumps in the trajectory that result in nonphysical velocities. Similarly, the angle is assumed to vary in the relatively broad range $-\pi/3 < \beta < \pi/3$. If $(u, v)_{\Gamma_{\max}}$ respects the above conditions, the tracked point is considered as a particle location and its position is saved along with the corresponding frame order number in the video. It is observed that by imposing these constraints, the first frame containing the particle is not likely to respect the velocity and angle limits and therefore is not sensed as a particle.

Further postprocessing of the data obtained from the tracking algorithm allows for preventing possible failures in the identification of the particles such as outliers and jumps in the trajectory. Specifically, the proximity of the sequence of frames with particle is exploited to recover all the images where the bead is present. This methodology verifies the proximity of the frame order numbers that respect the correlation, velocity and angle constraints as imposed through the tracking procedure. In particular, out of the total number of frames identified by the tracking algorithm, the largest sequence of consecutive frames is extracted; whereas frames pertaining to isolated order numbers are discarded. This is motivated by the assumption that the largest sequence of consecutive frames is highly probable to depict the bead trajectory. After the sequence is identified, the algorithm seeks for frames proximal to the initial and final images of the sequence. Proximal frames are defined as the six images whose order number is closest to the initial and final frames of the sequence. It is observed that neighbor frames may not be detected during the tracking if their associated value of $\Gamma_{\max}$ is smaller than Γ_{th}. The velocity and angle of the coordinates of $\Gamma_{\max}$ for the neighbor images are then compared to admissible values. In these experiments, the admissible velocity range is set to $0\,\mathrm{m/s} \leq U_p < 1.5\,\mathrm{m/s}$ while the angle limits are set to $-\pi/3 < \beta < \pi/3$. If the neighbor frame satisfies the velocity and angle constraints, it is considered as a particle and is therefore reinserted in the sequence.

The procedure above illustrated allows for rapidly detecting and tracking fluorescent particles moving in the channel without an external operator. A typical result is displayed in Figure 3.7(a), where colored dots represent the locations where $\Gamma_{\max}$ is attained for each frame of the processed video. Particle transit is identified by the change in color of the dots from their baseline blue. These dots are labeled with the corresponding frame order number for clarity. Bright blue dots in Figure 3.7(a) verify the condition $\Gamma_{\max} > \Gamma_{\mathrm{th}}$ and therefore indicate the initiation of the template updating. When the procedure of template updating begins, the values of $\Gamma_{\max}$ significantly increase above Γ_{th}. In particular, this occurs in correspondence of the particle transit in the field of view, that is, frames from 14 to 24. On the other hand, when frames without particle are processed, the values of $\Gamma_{\max}$ tend to decrease and the locations of the maximum values of correlation mostly cluster around fixed regions of the field of view where the object most similar to the particle is detected.

In Figure 3.7(b), the constraints on the correlation value, velocity, and angle are applied to the video and tracked points recognized as particles are labeled with the relative frame order number. It is noted

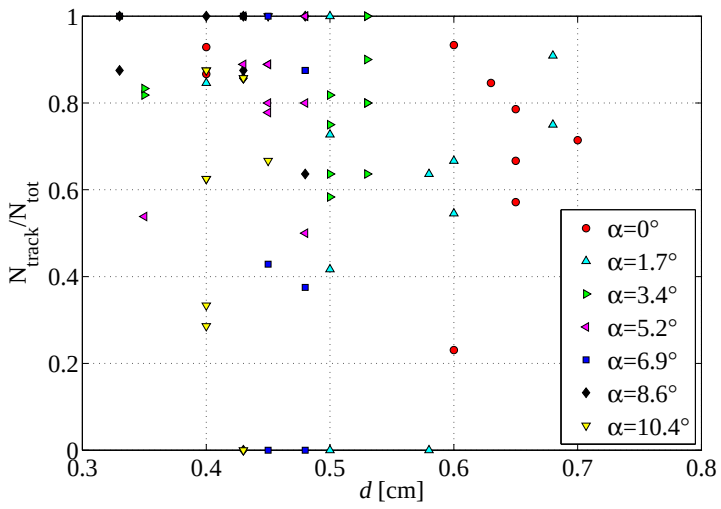

Figure 3.8: Number of particle frames detected by using the tracking algorithm, $\mathrm{N_{track}}$, out of the total number of pictures containing the bead, $\mathrm{N_{tot}}$, for different slopes α and depths d. Note that marker at $d = 0.43$ and $\alpha = 10.4°$ is overlapped to marker at $d = 0.43$ and $\alpha = 8.6°$.

that most of the frames pertaining to the particle transit are detected though some outliers are present, see points 2, 50, 55, 58, 67, and 69, and frame 21 is not sensed by the algorithm. In Figure 3.7(c), the postprocessed data obtained from Figure 3.7(b) are displayed. The sequence of frames with particles is now recovered and outlier data are eliminated. In addition, frame 21 is now reinserted in the sequence. Conversely, frame 14 does not satisfy the constraint on the angle and therefore is not retained in the postprocessing phase.

Therefore, both the maximum values of the correlations and the locations where they are attained are jointly used to substantiate the detection and tracking of the object of interest in the field of view. In particular, Figure 3.8 displays the number of particle frames detected by the algorithm after the postprocessing phase $\mathrm{N_{track}}$ out of the actual number of images containing the bead $\mathrm{N_{tot}}$. It is noted that $\mathrm{N_{tot}}$ is found by visual inspection of the frames. The plot is obtained by analyzing the entire set of videos for each combination of slopes and water depths, that is, 84 sequences of frames. The algorithm demonstrates high efficiency and robustness, in particular, on average more than the 70% of the particle frames is detected in the videos. Notably, in only 7% of the experiments, the particle is not detected in the entire recorded video, as evidenced by the six instances where $\mathrm{N_{track}}/\mathrm{N_{tot}} = 0$ in Figure 3.8. This demonstrates that the approach is robust in particle detection. Moreover, among the entire set of data, only 15% of the videos present values of the ratio $\mathrm{N_{track}}/\mathrm{N_{tot}}$ smaller than 0.5, that is, more than half of the frames containing the particle are detected for 85% of the image sequences, thus allowing for velocity identification in a broad set of conditions.

Chapter 4

A proof of concept in a natural stream

4.1 Introduction

As a proof-of-concept experiment of the feasibility of the presented methodology in natural settings, this fluorescent particle tracer is used to study the Rio Cordon natural mountainous stream in the Italian Alps. Two classes of experiments are conducted to provide a thorough characterization of the stream flow, that is, Flow Measurement Experiments (FMEs) at a selected stream cross-section and Travel Time Experiments (TTEs) on stream reaches of up to $30\,\mathrm{m}$. Specifically, FMEs are performed to estimate the flow velocity in an artificial section of the stream. Surface flow velocity in FMEs is estimated by deploying the fluorescent particles few meters upstream the experimental apparatus and then tracking their transit in the camera field of view. TTEs are conducted to estimate the travel time for varying amounts of fluorescent particles deployed in natural stream reaches of different lengths. Flow velocities are estimated by using the tracking algorithm developed by [71], whereas recorded videos for the travel time extraction are analyzed by using the index introduced by [70]. An array of traditionally used tracers, such as dyes and floating objects, is also considered in this experimental study to properly assess the advantages of the proposed methodology versus commonly used technologies.

Particles' passage is recorded as the beads transit under an experimental apparatus that hosts both the fluorescence excitation and video acquisition units, see Figure 4.1. The apparatus is composed of a horizontal telescopic system of aluminum bars that rests on adjustable steel tripods. The horizontal telescopic system includes three bars that allow for a total extension of the setup of approximately three meters. Another telescopic system of vertical aluminum bars is connected to the lamp case. The case contains an array of 14 UV $8\,\mathrm{W}$ lamps in parallel and series connections. On the upper side of the case, a heavy-duty aluminum plate connects the lamp unit to the aluminum bars. On the lower side of the case, a Poly methyl methacrylate plate protects the lamps from water. A low-cost CMOS Canon VIXIA HG20 camera is located on a tripod head connected to a vertical aluminum bar. The distance of the camera from the surface of interest is regulated through a compensating counterbalance. A metric ruler installed on aluminum bars allows for calibration of the acquired videos. The apparatus can be placed

Figure 4.1: Experimental apparatus including the lamp and video units. The telescopic systems allow for a remarkable flexibility of the setup in different environmental conditions.

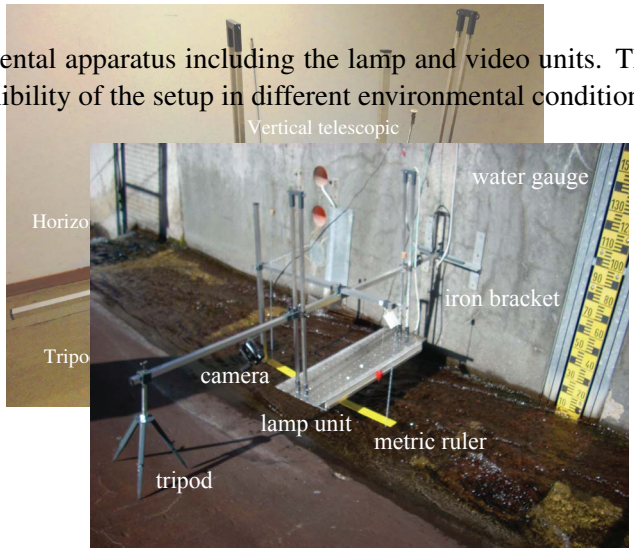

Figure 4.2: Experimental setup at the Rio Cordon station. The apparatus rests on a tripod on the hydrographic left bank and on an iron bracket on the right bank. The distance of the camera from the stream surface is adjusted through a compensating counterbalance.

along a stream cross-section and the distance of the lamp and video units from the water surface can be regulated according to illumination and flow conditions.

In this study, the experimental apparatus enclosing the lamp and video units is located along a cross-section of the artificial channel approximately $1\,\mathrm{m}$ downstream the water gauge, see Figure 4.2. The setup rests on a tripod on the stream left bank and on an iron bracket on the right bank concrete wall. During the preliminary calibration phase, the lamp unit is lowered at $12\,\mathrm{cm}$ from the water surface and the camera, at $17\,\mathrm{cm}$ from the surface, is inclined at a low angle to focus a $30\,\mathrm{cm} \times 15\,\mathrm{cm}$ area located upstream the video unit in the middle of the channel. The camera acquisition frequency is equal to $30\,\mathrm{Hz}$. Its resolution is set at $1440 \times 1080\,\mathrm{pixels}$ whereas the appropriate shutter speed is automatically adjusted according to the zoom position. Two black panel screens are inserted on the apparatus upstream the camera to reduce daylight reflections. The experiments are conducted during the same day from the

early afternoon to sunset to test various illumination conditions.

4.2 Flow measurement experiments

Flow velocity estimates are computed by using measurements from the fluorescent particle tracer and the traditional tracing systems. In experiments performed with the fluorescent particles, despite the tiny size of the spheres and the relatively low camera resolution and acquisition frequency, each of the 50 beads crossing the camera field of view is visible in the frame sequence. This evidence supports the feasibility of the methodology in natural settings.

Surface flow velocity for the fluorescent particle tracer is obtained by considering the selected five particle transits under the apparatus. In Figure 4.3, one of the five tracked sequence is displayed. Specifically, in Figure 4.3(a), the ortho-rectified green channels of three consecutive images containing the particle are depicted. Here, the particle appears as a brighter rectangle that advances from left to right from the time t_0 to t_2. A red box highlights the bead against the background. Brighter areas in the images are due to lamp reflections on the stream water surface. The plot in Figure 4.3(b) reports the locations $(u, v)_{\Gamma_{\max}}$ for the bead transit along with the values of the correlation coefficient.

The bead velocity in the image sequence is obtained by averaging values computed at each frame by the tracking algorithm. Further averaging over the values of the five sequences leads to the estimate reported in Table 4.1 along with the relative standard deviation.

Average flow velocities for the rhodamine and cork tracers are inferred from travel times measured along the artificial inlet. In Table 4.1, mean flow velocities are presented along with data from water gauge measurements and rating curves as provided by the Arabba Avalanche Center. The stream cross-sectional area at the gauge is calculated based on the water level measurement of $0.094\,\mathrm{m}$.

Table 4.1: Velocities $(\mathrm{m/s})$ for the FMEs for Each Tracing Methodology.

Tracer	Velocity	Standard Deviation
Rhodamine	1.76	n.a.
1/2 Cork	1.88	n.a.
Fluorescent bead	1.91	0.17
Water gauge	1.89	n.a.

As reported in Table 4.1, flow velocity estimations with rhodamine and corks tend to be lower than estimates with the fluorescent particles. The relatively low velocity predicted by rhodamine can be related to the fact that the tracer diffuses in water and thus traces the average stream velocity rather than the surface speed. On the other hand, the bulkiness of cork may be responsible for slowing the object's velocity on the water surface and therefore yielding conservative estimates. In addition, measurements with rhodamine and cork are performed over a flow path of $6\,\mathrm{m}$ whereas bead velocity is extracted from its transit below the apparatus, that is, a much smaller path. Therefore, the alternative tracers velocities are averaged over an entire stream reach that may be characterized by standing waves and turbulence

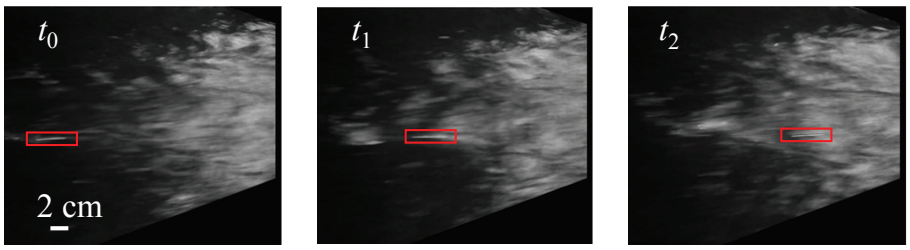

(a)

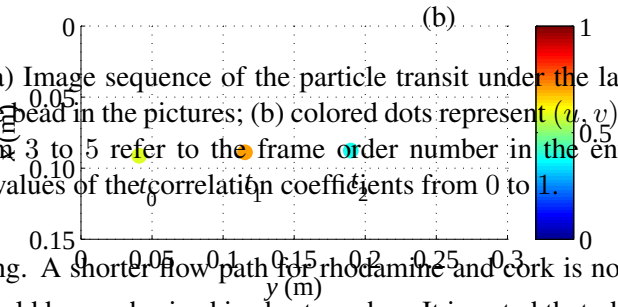

Figure 4.3: (a) Image sequence of the particle transit under the lamp unit. The red box identifies the location of the bead in the pictures; (b) colored dots represent $(u, v)_{\Gamma_{\max}}$ for each frame of the sequence. Numbers from 3 to 5 refer to the frame order number in the entire image sequence. The colorbar indicates the values of the correlation coefficients from 0 to 1.

at its beginning. A shorter flow path for rhodamine and cork is not considered due to synchronization issues that would be emphasized in short reaches. It is noted that, due to the smoothness of the concrete inlet, velocity is significantly higher than in the natural stream therefore, travel times are dramatically reduced. This fact may introduce errors due to slow reaction times of the operators, [58].

Water gauge levels are also affected by uncertainties mainly regarding the geometry of the channel cross-section and the accuracy of the gauge measurements. It is noted that the instrument is located approximately $1\,\mathrm{m}$ upstream the experimental apparatus on the river right bank, where the stream is slowed down by the effects of the wall and the hydraulic jump at the beginning of the artificial inlet. Nonetheless, velocity values are in good agreement with estimates obtained by using the fluorescent particle methodology.

Sources of uncertainties in estimates with the novel technique may reside into possible errors in the image ortho-rectification phase which may affect velocity estimation. Furthermore, the correlation algorithm may fail to detect the particle if the images contain objects similar to the beads in their geometry and intensity. This issue can be easily solved by adjusting the illumination of the field of view along with camera settings, such as the shutter speed and aperture. Moreover, given the rectangular shape of the bead, see Figure 4.3, the algorithm may correlate with pixels in different portions of the particle in subsequent images, that is, sometimes the tail of the rectangle and sometimes its head are identified as the location of the maximum correlation coefficient. This introduces some variations in the velocity

values that can be reduced by averaging over the entire sequence of frames.

4.3 Travel time experiments

Travel times are computed by using both the fluorescent particle technique and traditional tracers. Table 4.2 reports the main results grouped according to the flow length traveled by the tracer. The entry "none" refers to failed experiments where the deployed objects disperse or stop before reaching the final section of the path. Such events can be attributed to the extremely irregular stream channel bed. In particular, bulky tracers such as corks tend to stop at stream pool sections where small hydraulic jumps trap them thus nullifying the measurement. In travel time experiments, accuracy of the measurements lies in

Table 4.2: Average Velocities $(\mathrm{m/s})$ for the TTEs Performed with Different Tracing Methodologies. Values in parentheses are the standard deviations for measurements performed with the fluorescent particle tracer.

Lengths	4 m	12 m	27 m
Fluorescent beads	1.7 (0.21)	1.46 (0.16)	0.98
Rhodamine			0.68
1 Cork			0.55
1/2 Cork			none

the precise synchronization of the operators, [58], and the rigor of the operators in deploying the tracers at the center of the stream cross-section to have the objects flow along similar paths. These parameters play a crucial role in the experiments and may be responsible for slight variations in the values reported in Table 4.2.

Despite these sources of uncertainties, the results consistently highlight that longer flow paths corresponds to slower average velocities. This is reasonable since the uneven stream paths include step and pool tracts where water velocity continuously changes. It is noted that mean velocity estimated with rhodamine is usually lower than fluorescent particles' velocity. This is explained by the fact that rhodamine diffuses in water along the entire depth of the stream whereas the beads lie on the water surface where flow is usually faster than at deeper levels. Interestingly, a reasonable velocity index, which is defined as

$$\beta = v_{\mathrm{mean}}/v_{\mathrm{surf}}, \tag{4.1}$$

where v_{mean} and v_{surf} are the flow velocities averaged over the stream depth and at the stream surface, respectively, can be obtained from the travel time experiments. Specifically, for the $27\,\mathrm{m}$ flow path, flow velocity computed by using the rhodamine can be regarded as the stream average velocity, whereas the velocity of the fluorescent particles can be related to the stream surface velocity. Therefore, the value β equal to 0.7 is found, which is in good agreement with standard estimations used in the literature. It is commented that velocities obtained from the corks are significantly lower than estimates from other

tracers. In some cases, corks fail to accurately flow on the water surface and are trapped in lateral pool areas.

An additional tentative travel time experiment is performed on a $120\,\mathrm{m}$ flow path, not reported in Table 4.2. A sample of approximately $170\,\mathrm{g}$ fluorescent particles is deployed in the reach as well as rhodamine and floating objects such as polystyrene beads, corks, and $4\,\mathrm{cm}$ plastic spheres. Soon after the deployment, the dye disperses in the flow, whereas the floats are trapped into stream pools. This demonstrates that large batches of rhodamine are required for such long reaches while the geometry and density of the floats are inappropriate for the Rio Cordon complex bed structure. Conversely, some fluorescent particles reach the path final section thus crossing the camera field of view. Since only single particle transits are observed in the video, it is inferred that the particle cloud diffuses rather than compactly traveling in the stream flow. Therefore, the methodology may still be implemented on long stream reaches if larger quantities of tracing material are deployed.

Chapter 5

A proof of concept in a seminatural hillslope

5.1 Introduction

Hillslope overland flow controls multiple phenomena in natural watersheds, including surface runoff contributing to the basin hydrological response [56, 100–102]; rill development and erosion mechanics influencing soil roughness [67, 103, 104]; and pollutant diffusion and nutrient loss affecting agriculture and soil management [105].

Major challenges in the implementation of flow measurement systems in hillslopes are due to the ephemeral nature of microchannels along with shallow water depths and high turbidity, the presence of small scale vegetation, and the often poor geographical accessibility [106, 107]. Overland flow is experimentally monitored by excavating small trenches in hills [108–111] and collecting samples of water for laboratory or sediment analysis [112–115]. On the other hand, runoff discharge and flow rate measurements require more invasive procedures, wherein v-notch weirs and gauging flumes are installed in excavated trenches at the borders of experimental plots [100, 116–119]. Real time flow rate and water stage estimates can be computed by deploying sensors in such flumes, whereas overland flow rate can be automatically recorded by using tipping buckets [104, 120–123]. Erosion and runoff experimental studies are also conducted through physical sampling of overland flow water in tapped containers after precipitation events [124–126]. Such procedures are highly invasive for the environment and are hardly implemented on large scale plots. In addition, they are not adequate for real-time estimations in microchannel flows [127].

In overland flow settings, tracing techniques are valid alternatives to stream flow measurement systems, such as water gauging, electromagnetic, and acoustic sensors [62, 66]. In particular, experiments on natural or semi-natural hillslopes are often based on tracers, including chemicals, naturally occurring water isotopes, dyes, and salts [18, 58, 59, 128–130]. Tracer dispersion issues and losses are mini-

mized by conducting experiments on small scale plots [67, 127, 131]. Nonetheless, the tracer detection requires the deployment of probes or the collection of water samples, which can be hampered by the exiguous depths of natural rills [117, 127].

Interestingly, novel sensing instruments are recently being proposed for overland flow rate estimates. Specifically, in [16] spot measurements of surface flow rates are computed through an optical device exploiting reflectivity of floating objects. In [132], a sensor for sediment-laden flow rate is developed to estimate sediment concentration in runoff. Such promising devices provide local information on overland flows, yet their implementation is restricted to small scale and supervised experimental plots due to their limited resilience. In [133], Large Scale Particle Image Velocimetry (LSPIV) is coupled with laser scanning to estimate overland flow velocity and experimental results are compared against both hot film anemometry and salt tracing. This comparison suggests that LSPIV is a less invasive approach, which can also be easily automated [134]. Nonetheless, techniques based on image analysis are affected by ambient illumination, presence of patterns on the water surface [14, 135], and image distortions [136], which pose severe challenges in their implementation in uplands environments.

In this chapter, we present a novel tracing methodology based on the deployment and observation of enhanced fluorescence particles for surface flow measurements. Such approach aims at mitigating practical limitations of traditional techniques for monitoring overland flows. Specifically, the insolubility of the particles minimizes tracer adhesion to natural substrates and, therefore, is expected to reduce the requisite quantity of tracing material as compared to liquid dyes. Further, the enhanced visibility of the fluorescent particles allows for non-intrusively detecting the tracer through imaging techniques without deploying bulky probes and samplers in the water. These features along with the use of basic and resilient equipment provide grounding for applying the proposed methodology in an ample spectrum of scenarios, such as ephemeral micro-channels, high-sediment load flows, and heavy floods.

The feasibility of using buoyant fluorescent particles in static and dynamic water conditions in both daylight and dark is demonstrated in [70, 71] for laboratory settings. The transition of the methodology to natural environments is addressed through a proof of concept experiment performed in the Rio Cordon stream in the Italian Alps, [72]. This study mainly assesses the performance of the particles in stream flow settings, where high velocity regimes, presence of foam, and light reflections pose serious challenges to bead detection. Particles are therein used to conduct flow measurements at a stream cross-section and travel time experiments in stream reaches of up to $30\,\mathrm{m}$. Bead diameters of a few millimeters are selected to compensate for high flow rates.

Here, the proposed methodology is used for a proof of concept overland flow study on a semi-natural hillslope plot under high turbidity loads and soil and rain drops interaction. Such complex settings require the use of much smaller beads as compared to the stream flow analysis. Therefore, ad-hoc experiments are performed to assess the visibility and detectability of the particle tracers in these severe environmental conditions and their feasibility in estimating overland flow velocities. Experiments are conducted by using particles of varying diameters ranging from 75 to $1180\,\mu\mathrm{m}$. The particle detection

system, placed across a natural rill at the outlet of the studied experimental plot, hosts a light source for exciting the beads' fluorescence and a waterproof digital camera for video acquisition. Videos of beads' transit are processed through both supervised and unsupervised techniques to obtain average surface velocities of water flowing in the rill.

The buoyant fluorescent particles used in this study are purchased from Cospheric LLC. The spheres are white under daylight and emit yellow-green light ($561\,\mathrm{nm}$ wavelength) if excited by a UV light source ($365\,\mathrm{nm}$ wavelength). The particles are made of polyethylene and their fluorophore is embedded in the polymer matrix which allows for a long luminescence lifetime and enhanced and uniform visibility. The spheres are slightly buoyant and their nominal dry density is $0.98\,\mathrm{gcm}^{-3}$. Table 5.1 indicates the classes of particles used in this proof of concept experiment ordered in terms of their diameter. This wide spectrum of diameters is used to establish guidelines for particle selection in tracing shallow waters in natural conditions.

Table 5.1: Classes of particle diameters used for the experiments.

Class	1	2	3	4	5	6	7	8	9
Diameter (μm)	75-90	106-125	150-180	250-300	355-425	500-600	710-850	850-1000	1000-1180

Particles' transits are recorded as the beads float on the rill water surface underneath the experimental detection apparatus. The apparatus hosts both light source and video acquisition units, see Figure 5.1. A telescopic system of vertical aluminum bars is connected to the lamp case and allows for regulating image illumination by adjusting the distance of the light source from the water surface. The case contains an array of 14 UV $8\,\mathrm{W}$ lamps in parallel and series connections. A low cost water proof Bullet HD 1080p camera is located on a tripod head connected to a vertical aluminum bar. The Bullet camera is manually operated and set at $1920 \times 1080\,\mathrm{pixels}$ resolution for video recording at the acquisition frequency of $30\,\mathrm{Hz}$. A compensating counterbalance is used to adjust the distance of the camera from the surface of interest. A metric ruler installed on aluminum rods allows for calibration of the acquired videos. The distance of the video acquisition unit from the surface and light source can be adjusted according to illumination and dimensions of the field of view. In dim illumination conditions, a $568\,\mathrm{nm}$ optical filter is placed on the bullet camera to emphasize particle brightness.

Experiments are performed in a terrain parcel in the Azienda Agraria at the University of Tuscia, Viterbo, Italy, where a semi-natural hillslope is prepared out of $40\,\mathrm{m}^3$ of soil, see Figure 5.2. The plot is $1.7\,\mathrm{m}$ high, $6.5\,\mathrm{m}$ long, and $3\,\mathrm{m}$ wide and it is covered by grass only for the 10%. The granulometry of the soil is provided in Table 5.2. In the center of the plot a mild concavity is preliminary raked

Table 5.2: Granulometry of the experimental plot. The soil used for the plot can be classified as sand according to the International Society of Soil Science (ISSS).

Soil type	Clay	Silt	Sand
Portion (%)	11.55	21.76	66.69

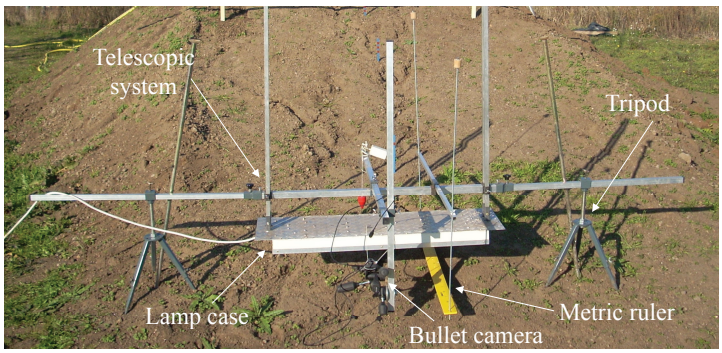

Figure 5.1: Experimental apparatus including the light source and the video acquisition units. The metric ruler is used for calibrating acquired videos.

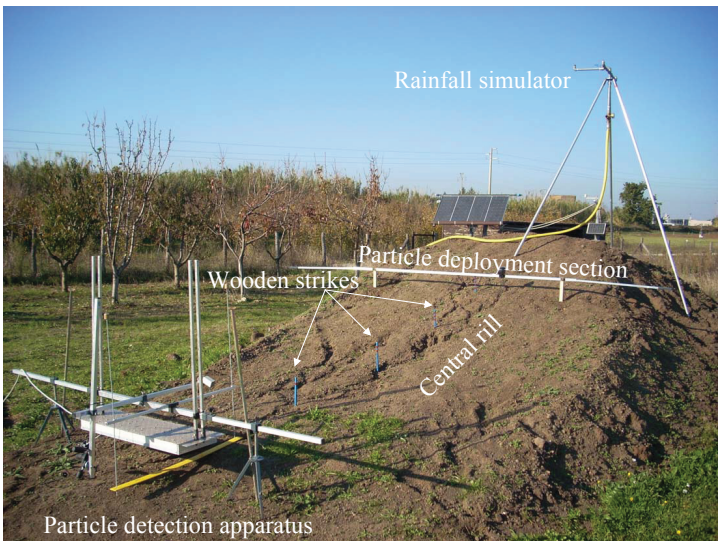

Figure 5.2: View of the experimental site depicting the particle detection apparatus and the rainfall simulator.

to create a preferential path to rainfall and then irrigated for a few hours. After irrigation, a $4\,\mathrm{m}$ long central rill is formed in the plot and the experimental detection apparatus is located at its terminal part, see Figure 5.2. The slope of the hill is approximately equal to 17° and shows a slight concavity after a few rainfall experiments. A rainfall simulator is placed on the top corner of the plot, see Figure 5.2, to provide a uniform rain distribution on the entire hill. The particle deployment section is marked with wooden strikes at approximately $4\,\mathrm{m}$ upstream the detection setup. Four additional wooden strikes are installed one meter apart along the rill from the upstream section.

5.2 Particle detection procedure

Travel time experiments are conducted by synchronizing particle deployment and video acquisition. Particle travel time is identified as the time the beads take to flow from the deployment section on the plot to the detection apparatus along the $4\,\mathrm{m}$ long rill. The arrival of the particles at the detection setup refers to when the particles enter the field of view of the camera. The transit of the particles is identified through image-based analysis tools by converting captured videos into RGB frames and then analyzing the sole green channel where particle emissions are more evident. In particular, gray-scale frames are processed by using a modified version of the index $\mathscr{G}$ defined in [70].

An automatic procedure for the identification of the beads is introduced to partially filter signal noise due to the presence of external and uncontrolled light sources, water surface reflections, and extraneous objects and sediments. Specifically, a moving average of the time trace of the index is computed for each experimental video by using subsets of ten consecutive images. For convenience, such filtered time trace is referred to as G. Then, peaks in the signal are automatically detected by fitting G with a gaussian function. This fit is first implemented using windows of 50 values of the filtered time history. In the fitting procedure, the length of the fitted window is iteratively increased up to 150 values to capture eventual occurrences of elongated particle trains. Fitting is executed by constantly skipping 15 values of the filtered time trace. The nonlinear least square method is used to perform the fitting. Goodness of the procedure is ascertained by imposing that the coefficient of determination is equal or greater than a threshold value equal to 0.85.

The sequence of frames identifying the transit of the particles are found by imposing further constraints on the fitted window which presents the highest coefficient of determination. In particular, the mean value of the fitting gaussian function is required to lay in the interval $[m - 0.15l, m + 0.15l]$, where m is the mean time in the window of interest and l corresponds to the length of the window. In addition, constraints are imposed on the minimum and maximum values of G in the analyzed window. Specifically, the presence of a peak in the intensity is assessed by imposing $0.4 \leq (\max G - \min G)/\max(G) \leq 1$ in the fitted interval. Experimental videos satisfying such constraints lead to the identification of particle transits. As the brightest frame sequences are determined, the frame order number corresponding to the first value of G in the fitted window is divided by the camera acqui-

sition frequency and used to calculate the beads travel time.

5.3 Experimental results

Travel time experiments are conducted by activating the rainfall simulator at the constant intensity of approximately $50\,\mathrm{mmh}^{-1}$ to produce a water head of a few centimeters in the rill. The particle detection apparatus is placed at the flat base of the hillslope, that is, at the terminal section of the rill with the bullet camera and the lamp unit at approximately $20\,\mathrm{cm}$ from the rill bed. To prevent excessive distortions in videos, the camera is angled at $70\,^\circ$ from the horizontal. The simulator nozzles are placed at an height of approximately $2.3\,\mathrm{m}$ from the soil on the top of the hillslope.

For each experiment, a sample of $4-5\,\mathrm{g}$ of particles of a selected diameter class is deployed at the rill onset at approximately $4\,\mathrm{m}$ from the detection apparatus. The instant of deployment and the beginning of the video are synchronized with a precision of approximately $0.1\,\mathrm{s}$. Such precision is achieved by using a chronometer synchronized with the camera. For each class of particle diameters, ten repetitions are performed. The rainfall simulator is active for the entire duration of the experiments. Once videos are taken, frames are processed to estimate surface flow velocity by dividing the total length of the rill by the particle travel time.

Before and after each experiment, the width and depth of the rill at the strikes sections and underneath the detection apparatus are measured to account for erosion and sediment transport phenomena and to monitor rill bed evolution. In addition, experiments are performed over one month and during sunny days in absence of strong wind to limit possible biases in the uniformity of the simulated rainfall. To prevent destructive rill bed erosion and sediment wash-off, the plot is covered with a waterproof cloth during rainy days.

5.4 Supervised analysis

Ten videos for each class of bead diameters are converted to frames and manually analyzed to observe the transit of the particles. This supervised visual analysis demonstrates the enhanced detectability of the fluorescent particles in complex conditions. Specifically, particles from all classes are generally visible in the area captured by the camera despite poor image quality.

Three different behaviors can be observed by visually analyzing recorded videos according to the specific dimensions of the particle tracer. For particles of diameters ranging from 75 to $180\,\mu\mathrm{m}$, deployed samples appear as a white powder as they flow along the rill, see Figure 5.3, where beads are trapped at the rill outside bend into small vortical structures. Particles are then released downstream the bend that are visible in the detection section depending on the size of the bead cloud. Figure 5.4 displays the transit of a cloud of $75-90\,\mu\mathrm{m}$ beads as captured by the camera. The powder crosses the region of interest, that extends for approximately $8\,\mathrm{cm}$, in 18 frames. Note that snapshots in Figure 5.4 are not

Figure 5.3: Beads of smaller diameters trapped at the outside bend of the rill, see red dashed ellipse.

orthorectified. Therein, the particle cloud compactly travels throughout the entire length of the region of interest making the beads easily detectable by the operator. In addition, fluorescence is clearly recognizable against the background even though water turbidity and suspended sediment load are remarkable.

Conversely, particles ranging from 710 to $1180\,\mu\mathrm{m}$ tend to disperse as they are deployed in the rill, see Figure 5.5, where particles of larger diameters disperse due to the presence of sediments and subrills. The samples travel in the form of isolated particles that are still visible at the detection section due to their relatively large size. In particular, Figure 5.6 displays the transit of isolated particles of $1000 - 1180\,\mu\mathrm{m}$ in diameter. In this case, the particle train is highly elongated and its entire passage is difficult to identify. Specifically, the transit of the sample is detected as a sequence of independent particles in the camera field of view.

Particles of intermediate sizes, that is, beads ranging from 250 to $600\,\mu\mathrm{m}$, are affected by a combination of the two formerly described behaviors. In particular, dispersal of the sample tends to occur from the very deployment into the rill as for the $710 - 1180\,\mu\mathrm{m}$. On the other hand, such particles are not distinctly visible when reaching the detection apparatus due to their rather small dimensions. These factors critically affect the detection of the particles by visual inspection.

Travel times computed through visual inspection are obtained by identifying the frame where beads first appear in the camera's region. Since the camera acquisition and particle deployment are synchronized, the time taken by the particle to reach the detection apparatus is easily found by dividing the frame order number by the camera acquisition frequency. Velocity is then obtained by dividing the

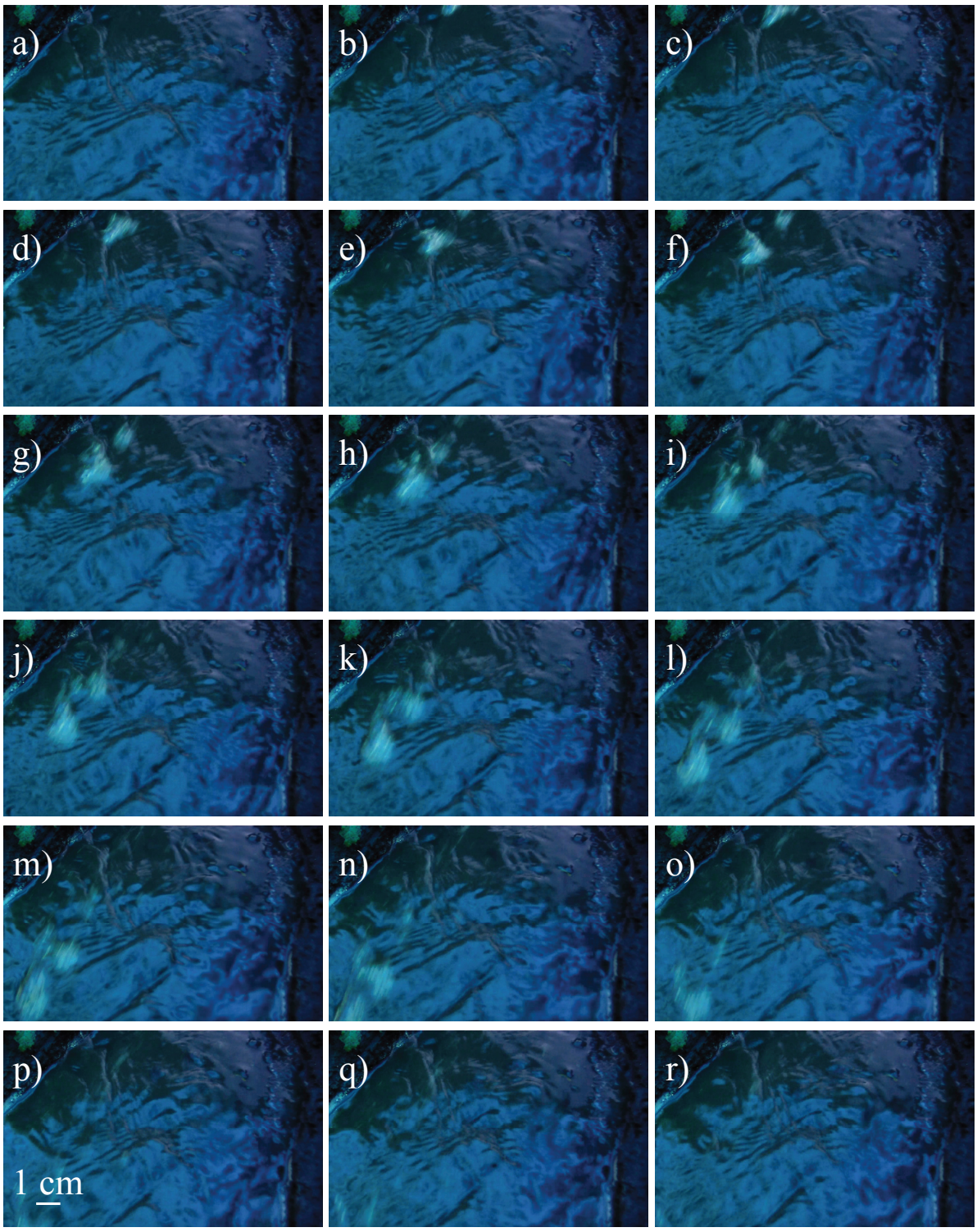

Figure 5.4: Sequence of snapshots depicting the transit of a cloud of particles flowing in the rill below the detection apparatus. The diameter of the beads lays in the range $75 - 90\,\mu\mathrm{m}$.

Figure 5.5: Beads of larger diameters diffuse in the channel due to the presence of sediments and subrills, see red dashed ellipses.

travel time by the approximate length of the rill, that is, $4\,\mathrm{m}$.

Two additional travel time experiments with rhodamine WT dye are conducted to compare the presented methodology with more commonly used approaches. Experiments with rhodamine are conducted by releasing $0.5\,\mathrm{mL}$ of dye at the deployment section and by synchronizing the release with the acquisition of the digital camera. The time the dye takes to flow along the $4\,\mathrm{m}$ long rill is found by converting experimental videos into frames and then manually analyzing images. The first frame at which the presence of the dye is observed is then divided by the acquisition frequency of the digital camera to recover the travel time.

Estimations of the travel time through visual inspection are generally possible for videos depicting transits of the $1000-1180\,\mu\mathrm{m}$ particles. In this case, the analysis gives an average velocity of $0.33\,\mathrm{ms}^{-1}$ over the ten experimental repetitions with a standard deviation of $0.02\,\mathrm{ms}^{-1}$. This value is in good agreement with velocity obtained by using the rhodamine dye, that is, $0.34\,\mathrm{ms}^{-1}$ with standard deviation $0.01\,\mathrm{ms}^{-1}$. Experiments with smaller particles do not lead to accurate estimations of travel time due to the poor visibility of first beads arrival.

5.5 Unsupervised analysis

The above discussion on particle visibility is supported by the calculation of the index $\mathscr{G}$ and its filtered version G on experimental videos. Specifically, Figure 5.7 displays the index $\mathscr{G}$ for three representa-

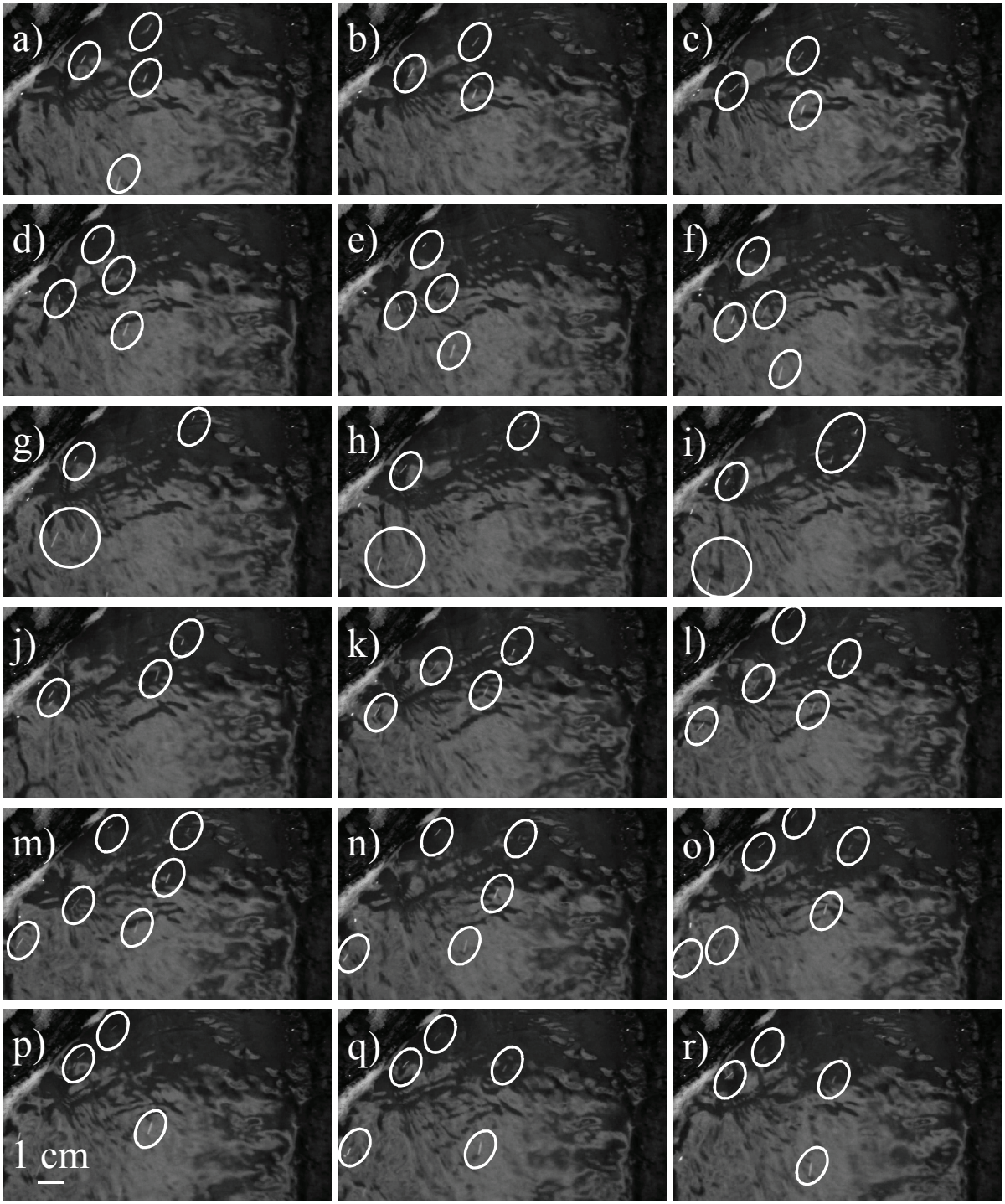

Figure 5.6: Sequence of snapshots depicting the transit of single particles flowing in the rill below the detection apparatus. Diameters of the beads are in the range $1000 - 1180\,\mu\mathrm{m}$. Only the green channel is reported for clarity.

tive experiments for particles of diameters equal to $75 - 90\,\mu\mathrm{m}$, $1000 - 1180\,\mu\mathrm{m}$, and $500 - 600\,\mu\mathrm{m}$, respectively. The peak at frame 1366 in Figure 5.7(a) pertains to the passage of the cloud of particles depicted in Figure 5.4. Two peaks and higher values of the index are observed from frame 694 to 791 in Figure 5.7(b), relative to the snapshots shown in Figure 5.6. On the other hand, in Figure 5.7(c), no peak is clearly evident. Such findings confirm that the index successfully detects the transit of bright clusters of particles even if it likely fails to identify the arrival of the first beads of small diameters. It is also observed that intensities in Figure 5.7(b) are lower than intensities of the peak in Figure 5.7(a). Therefore, higher index values in Figure 5.7(b) are more likely to pertain to isolated particles flowing through the region of interest as anticipated from the supervised analysis. Finally, particles of intermediate sizes are not detected by the index.

The unsupervised image analysis is applied to each of the ten experimental repetitions recorded for the studied diameters to automatically obtain particle travel time. The only green channel of the images is analyzed and frames are preliminary cropped to restrict particle search to the portion of the image depicting the rill bed.

Experimental videos fulfilling the constraints imposed through the fitting procedure are reported in Table 5.3. Specifically, two videos are fitted for the $75 - 90\,\mu\mathrm{m}$, five for the $150 - 180\,\mu\mathrm{m}$, one for the $710 - 850\,\mu\mathrm{m}$, and three for the $1000 - 1180\,\mu\mathrm{m}$ diameters. Travel time is estimated from the frame order number corresponding to the first value of G in the fitted window and velocities relative to each fitting are presented in Table 5.3.

Table 5.3: Velocities obtained through the image analysis procedure, IM Velocity, and visual analysis, VA Velocity. VA velocities are reported for the larger classes of diameters since experiments with smaller particles do not allow for accurate travel time estimations.

Diameter $\mu\mathrm{m}$	IM Velocity ms^{-1}	VA Velocity ms^{-1}
75-90	0.08	n.a.
	0.11	n.a.
150-180	0.11	n.a.
	0.18	n.a.
	0.11	n.a.
	1.47	n.a.
	0.46	n.a.
710-850	0.05	n.a.
1000-1180	0.29	0.33
	0.28	0.31
	0.26	0.34

Results in Table 5.3 show that unfeasible velocities are obtained for the smaller particles and therefore confirm that the index is not able to detect first arrivals for beads of diameters of $150 - 180\,\mu\mathrm{m}$ and

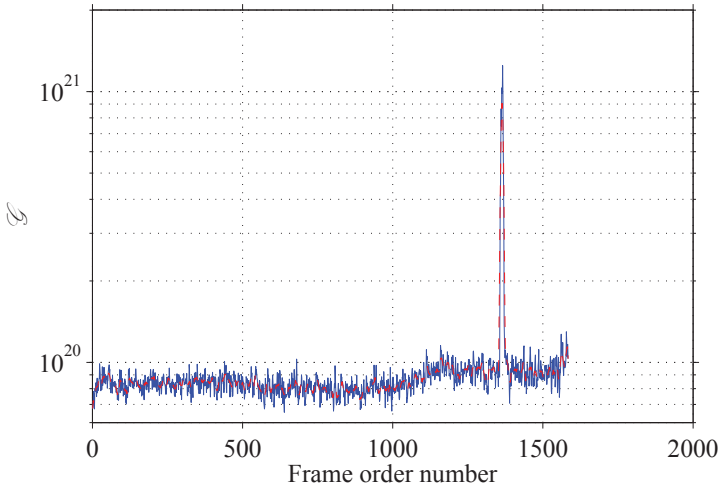

(a)

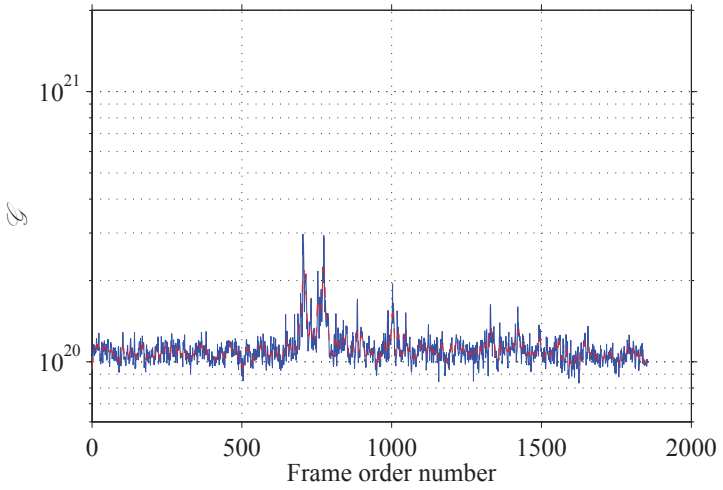

(b)

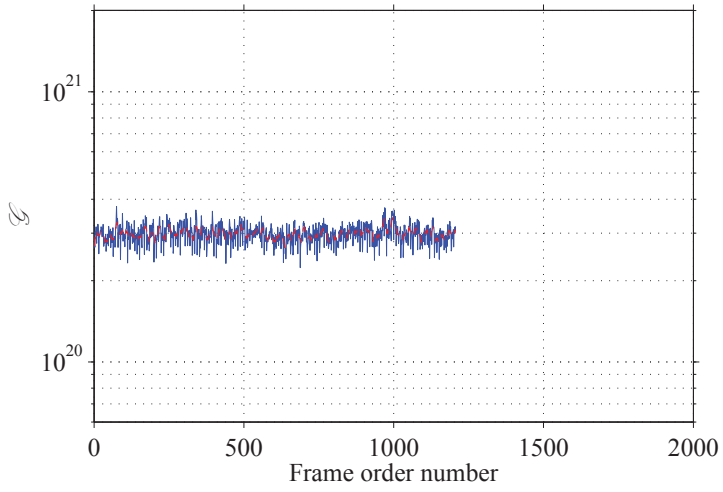

(c)

Figure 5.7: Index $\mathscr{G}$ as obtained from Eq. 6.3 for (a) beads of $75-90\,\mu\mathrm{m}$; (b) $1000-1180\,\mu\mathrm{m}$; and (c) $500-600\,\mu\mathrm{m}$. Moving averaged index, G, is presented in red.

smaller. Nonetheless, the fitting procedure can be used to sense the transit of particle clouds of small dimensions. Notably, four experiments out of the five reported in Table 5.3 for $150 - 180\,\mu\mathrm{m}$ diameters pertain to the actual transit of the beads whereas the velocity value equal to $1.47\,\mathrm{ms}^{-1}$ is biased by reflections on the water surface. On the other hand, larger particles, such as the $1000 - 1180\,\mu\mathrm{m}$ beads, are easier to detect and estimated velocities are comparable to values obtained from visual analysis and experiments with rhodamine. Such finding is also confirmed from analysis of Figure 5.7. Indeed, the group of $75 - 90\,\mu\mathrm{m}$ beads in Figure 5.7(a) is likely not the first cluster of particles to arrive at the detection apparatus since the peak only occurs $37\,\mathrm{s}$ after sample deployment, thus yielding an equivalent but unlikely flow velocity of $0.11\,\mathrm{ms}^{-1}$. Conversely, Figure 5.7(b) captures the whole transit of the particles as higher values of the index are measured for approximately $3 - 4\,\mathrm{s}$. It is further observed that larger fitted windows correspond to larger diameters due to the fact that particle samples of larger dimensions tend to diffuse in the rill and, therefore, bead trains take longer time to cross the region captured by the camera.

As evidenced by the supervised and unsupervised analysis, the $1000 - 1180\,\mu\mathrm{m}$ beads can be identified as the optimal particles to be adopted for the experimental settings of this study. In particular, velocities obtained from the automatic procedure are only 15% lower than estimates from visual analysis and results from both methodologies are close to the velocity estimated with the rhodamine dye. Promising results are also found for four out of ten experiments with the $150 - 180\,\mu\mathrm{m}$ beads, see Table 5.3. Specifically, the index is able to capture the passage of groups of particles of such small diameters for half of the experiments.

Chapter 6

Eco-friendly particle synthesis and characterization

6.1 Introduction

In this chapter, we describe a novel methodology for fabricating inexpensive environmentally-friendly fluorescent particles for quantitative flow visualization. Particles are synthesized from natural beeswax and a highly diluted solution of a nontoxic fluorescent red dye. The fabrication procedure allows for adjusting the size of the particles from tens of microns up to a few millimeters and their density from positively to negatively-buoyant with respect to water. An array of experimental techniques is employed to conduct a thorough characterization of the fluorescence and morphology of the tracers. In addition, ad-hoc experiments are designed to assess the fluorescence response due to Ultra Violet (UV) exposure and thermal processes. A proof-of-concept PIV study is conducted to illustrate the integration of the novel particle tracers in existing velocimetry methods for surface flow analysis.

Particles are synthesized from natural white beeswax pellets purchased from Stakich Inc., MI., whose density is approximately equal to $0.95\,\mathrm{g/cm^3}$. A batch of $20\,\mathrm{g}$ of beads is obtained by melting $23\,\mathrm{g}$ of wax at $60^\circ - 65^\circ$ C through a thermostatic bath and by stirring them at $350\,\mathrm{rpm}$ until melting is achieved. A $6 \times 10^{-3}\,\mu\mathrm{g/l}$ diluted solution is prepared from nontoxic Fluorescent FWT Red Dye Concentrate, Cole Parmer®. A volume of $8\,\mathrm{ml}$ of diluted solution and $1\,\mathrm{ml}$ of surfactant Polysorbate-20, $1.1\,\mathrm{g/cm^3}$ in density, are added to the melted wax and stirred at $350\,\mathrm{rpm}$ until homogeneous mixing is achieved. The emulsion is then poured in $100\,\mathrm{ml}$ of hot water at $60^\circ - 65^\circ$ C and kept under stirring at $600\,\mathrm{rpm}$ for $3-4$ minutes to facilitate the formation of wax drops. After drop formation, $125\,\mathrm{ml}$ of cold water at 5° C are added to the mixture and stirring is stopped. Cold water produces the instantaneous cooling of the wax drops that solidify and migrate to the surface of the suspension. Particles are then collected through filtering with a $20\,\mu\mathrm{m}$ sieve and desiccated with silica gel for $48\,\mathrm{hrs}$. The diameters of the beads obtained with a stirring frequency of $600\,\mathrm{rpm}$ range from less than 20 to $500\,\mu\mathrm{m}$. In particular,

40% of the particles lie in the range $250 - 420\,\mu\mathrm{m}$. The size of the beads can be adjusted by regulating the frequency of the rotation of the magnetic stirrer in the emulsion of wax and hot water. Specifically, higher frequencies lead to smaller particles, whereas frequencies as low as $300\,\mathrm{rpm}$ produce particles of a few millimeters. Particles are positively buoyant in water, yet, negatively-buoyant beads can be obtained by following a similar fabrication procedure where quantities of calcium carbonate of density in the range $2.7 - 2.8\,\mathrm{g/cm^3}$ are added to the emulsion of beeswax and fluorescent solution. Due to the low affinity of beeswax for calcium carbonate, diluted solutions of surfactant should be added to the emulsion and stirring performed for several minutes. The amount of calcium carbonate added to the emulsion can be adjusted to vary the density of the particles. In particular, particles are found to sink in water when amounts of calcium carbonate greater than $5\,\mathrm{mg}$ are released in the $100\,\mathrm{ml}$ hot emulsion. Advanced fabrication methods for mechanical emulsification based on high pressure or ultrasound homogenizers, microporous membranes, and microfluidizers [137] are expected to be relevant towards the massive production of fluorescent particle tracers of highly controlled shape and size. However, the need for regulating the temperature of the beeswax emulsion to guarantee the complete mixing of the matrix with the dye is anticipated to pose severe challenges in adapting such advanced methods.

When compared with the state of the art on tracers for surface flow physics analysis, the proposed fluorescent beeswax particles demonstrate several advantages. Differently from polyethylene, titanium, aluminum, and silver particles typically used in PIV [42, 72], beeswax is biodegradable with natural biodegradation time of $28\,\mathrm{days}$ [138]. Moreover, fluorescent FWT Red Dye Concentrate is nontoxic in contrast with fluorescent tracers traditionally used in environmental studies, such as Rhodamine WT, Rhodamine B, and Fluorescein [13]. Finally, the proposed particles can be inexpensively fabricated at a limited cost of $0.025\,\$/\mathrm{g}$ in contrast with commercially available fluorescent particles, whose costs [81] range from $0.8\,\$/\mathrm{g}$ to $9.9\,\$/\mathrm{g}$.

6.2 Fluorescence characterization

The characterization of the particle fluorescence is performed by conducting excitation and emission scans of solutions at different concentrations of Fluorescent FWT Red Dye and particle samples with PTI Quanta Master 40 spectrofluorometer. Specifically, diluted liquid solutions are prepared by varying the dye concentration from 0.01 to $0.1\,\mu\mathrm{g/l}$. The emission scan of liquid solutions with excitation at $450\,\mathrm{nm}$ results in the spectra displayed in Figure 6.1, where emissions are multiplied by 100 for improved readability. It is noted that more diluted solutions lead to higher fluorescence quantum yields accompanied by shifts towards lower wavelengths. Such behavior is attributed to collisional quenching effects which are typical of the rhodamine-family dyes [139–141]. Figure 6.1 also reports the emission and excitation scans for a volume of $2\,\mathrm{ml}$ of melted fluorescent particles. Notably, particles present a broad excitation spectrum which allows for stronger fluorescence under a wide range of wavelengths. This is crucial for conducting experiments in natural flow systems where sunlight can be used as the

excitation source [71–73]. In addition, particle emission spectrum is shifted towards lower wavelengths with a higher peak as compared to diluted solutions of the fluorescent dye. This is likely due to collisional effects' reduction from mixing wax and water with the highly diluted dye solution during the fabrication procedure, which contributes to decreasing the concentration of fluorophore molecules in the particles.

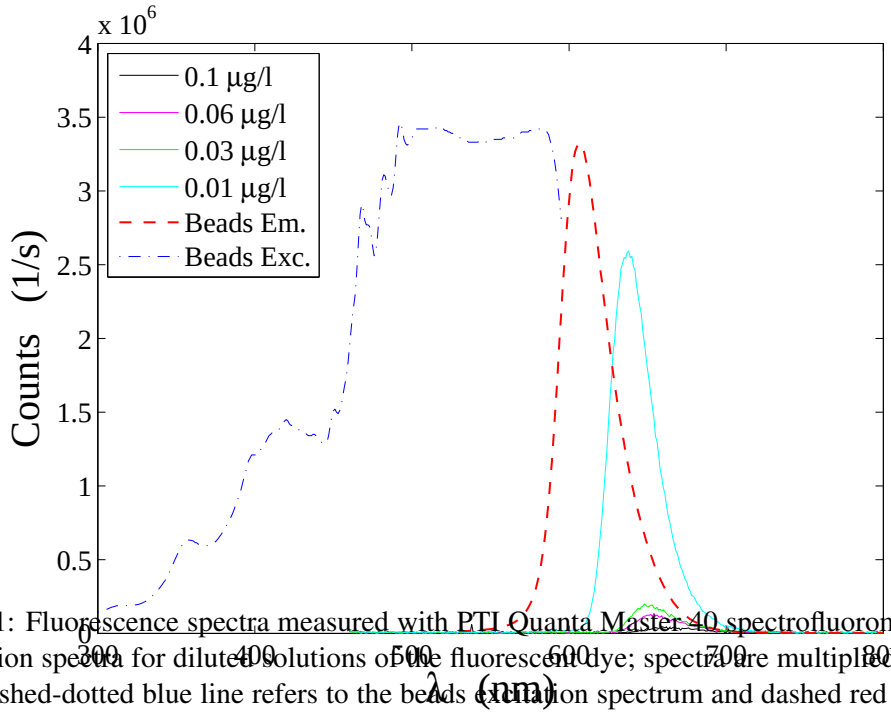

Figure 6.1: Fluorescence spectra measured with PTI Quanta Master 40 spectrofluorometer. Solid lines are emission spectra for diluted solutions of the fluorescent dye; spectra are multiplied by 100 for legibility. Dashed-dotted blue line refers to the beads excitation spectrum and dashed red line to the beads emission spectrum.

The effects of weathering agents on the lifetime and intensity of the particle fluorescence emissions are assessed by exposing beads to high-energy radiations and hot water and periodically measuring their emission through GloMax®-Multi Jr fluorometer. These nondestructive experiments are performed on the solid unmelted beads and, thus, preserve the total surface subject to external agents. The effect of high-energy light on the particle fluorescence is studied by continuously exposing ten samples of $0.5\,\mathrm{g}$ of beads to an $8\,\mathrm{W}$ UV lamp, $365\,\mathrm{nm}$ in wavelength, for two weeks. During the experiment, beads are stored in ten labeled petri dishes in an opaque environment at $15\,\mathrm{cm}$ below the UV lamp. Each sample is transferred in plastic methacrylate $10\times10\,\mathrm{mm}$ cuvette containers to perform the measurement. Before testing, samples are tapped to guarantee that the particles are closely packed in the cuvettes and, therefore, limit the presence of voids that may bias the optical data. The intensity of the fluorescence emission is measured with two optical kits: the green module (excitation wavelength: $525\,\mathrm{nm}$ and

emission wavelength: $580 - 640\,\mathrm{nm}$) and the UV-GFP module (excitation wavelength: $365\,\mathrm{nm}$ and emission wavelength: $515 - 570\,\mathrm{nm}$). Every other day, five acquisitions are taken at intervals of two seconds with both optical modules on each sample and averaged to characterize the sample behavior. Unexpectedly, the data recorded at the end of the two weeks are on average three times the initial values recorded with the green module and two times the values obtained with the UV-GFP kit.

Such time dependence is studied by performing a repeated measures analysis of variance on the collected data (ten particle samples and seven repeated measures for each sample). The analysis reveals a statistically significant time-effect (level of significance < 0.0001) suggesting that exposure to UV light modulates particle fluorescence. An additional test performed with PTI Quanta Master 40 spectrofluorometer at the end of the UV ray exposure allows for further investigating the increase in the emissions. Specifically, four samples of particles previously exposed to UV light are melted and used for emission scanning. The peak of the emission spectrum is shifted to $592\,\mathrm{nm}$ and the intensity is comparable to the maximum intensity detectable by the instrument ($3.76 \times 10^6\,1/\mathrm{s}$). Such phenomena are likely attributed to photobleaching effects induced by the high-energy rays which tend to degrade fluorophore molecules [142, 143]. A decrease in fluorescing molecules leads to reduced collisional quenching and, therefore, higher fluorescence quantum yield. These conclusions are confirmed by visual inspection of UV-exposed beads which present a faded pink coloring, suggesting that fluorophore molecules in the external layer of the particles are degraded by the high-energy light radiation.

The effect of hot water on particle fluorescence is evaluated by deploying a sample of $0.5\,\mathrm{g}$ of beads in $100\,\mathrm{ml}$ of tap water at $50^\circ\,\mathrm{C}$. Particles are continuously kept in hot water and under magnetic stirring at $350\,\mathrm{rpm}$ for 12 hours a day for two weeks. Fluorescence measurements are performed by filtering the suspension, desiccating the beads with silica gel for a few hours, and then transferring the sample in a methacrylate cuvette for acquisitions with GloMax®-Multi Jr fluorometer. Every other day, the emission intensities of the samples are analyzed following the procedure presented above. In particular, values measured with the green module are reduced of 91% and data recorded with the UV-GFP kit show a decrease of 84%. An additional test performed on the melted material with PTI Quanta Master 40 spectrofluorometer does not display significant peaks in the emission spectrum. More specifically, the material is not fluorescent when excited under a broad range of wavelengths. This suggests that fluorophore molecules are degraded and washed out during the thermal treatment as qualitatively confirmed by the opaque cyan coloring of the beads at the end of the experiment.

6.3 Microscopy characterization

Particle characterization is conducted by peering into the microstructure properties of the synthesized material. Specifically, this Section reports microscopy studies performed with a wide array of different techniques.

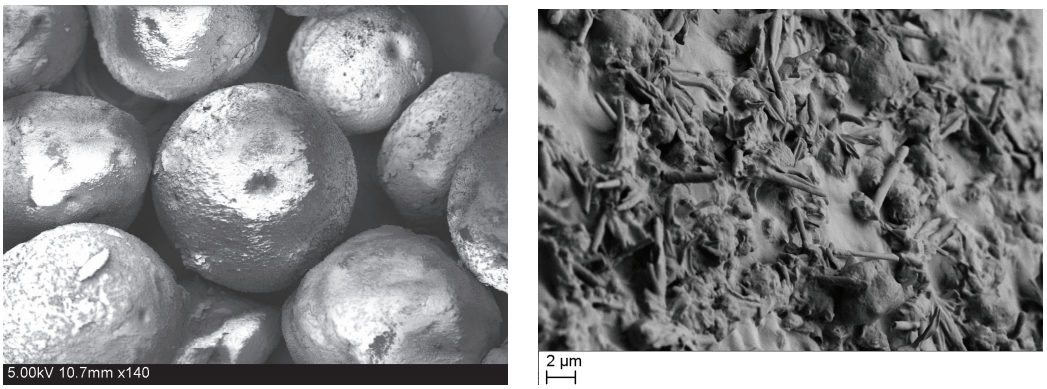

(a) (b)

Figure 6.2: Microscopies of (a) the fluorescent beads and (b) the beads' surface microfeatures.

6.3.1 Field emission scanning electron microscopy

Field emission scanning electron microscopy (FESEM) is used to study the morphological features of the particles. Specifically, low and high resolution images are recorded with Zeiss Sigma Field Emission SEM microscope equipped with energy dispersive spectroscopy, EDX Oxford INCA PentaFETx3 EDS system model 8100. Samples of undyed and environmentally friendly beeswax particles are coated with a layer of $20\,\mathrm{nm}$ of gold to minimize electron charging during observation with the microscope. Undyed particles are obtained by following the fabrication procedure without adding the fluorescent solution to the wax emulsion.

The particles are approximately spherical and with surface microfeatures attributable to the thermal fabrication procedure. The sphericity of the beads is largely due to the hydrophobic properties of wax in the emulsion. Figure 6.2(a) and (b) depict high magnification pictures of the untreated and fluorescent beads, respectively. It can be noted that treated beads exhibit microfeatures such as rods and platelets which are related to the presence of the dye and are further investigated in Section 6.3.3.

6.3.2 X-ray diffraction

X-ray diffraction (XRD) spectra are acquired for the unprocessed and environmentally friendly particles using Rigaku Miniflex X-Ray Diffractometer. Specifically, a few grams of $250 - 420\,\mu\mathrm{m}$ environmentally friendly beads and a few pellets of unprocessed wax are tested through XRD to highlight possible modifications of the wax due to the beads synthesis procedure. Figure 6.3 displays XRD spectra for the unprocessed wax and the environmentally friendly particles whereas characteristic peak patterns for the beads are reported in Figure 6.3.

As expected, XRD confirms the polycristalline nature of beeswax. Interestingly, such structure is preserved during the particle fabrication procedure as depicted in Figure 6.3, where peaks are found at comparable angles in the unprocessed and doped specimens. Spectral peaks located at $2\theta = 37^{\circ}$

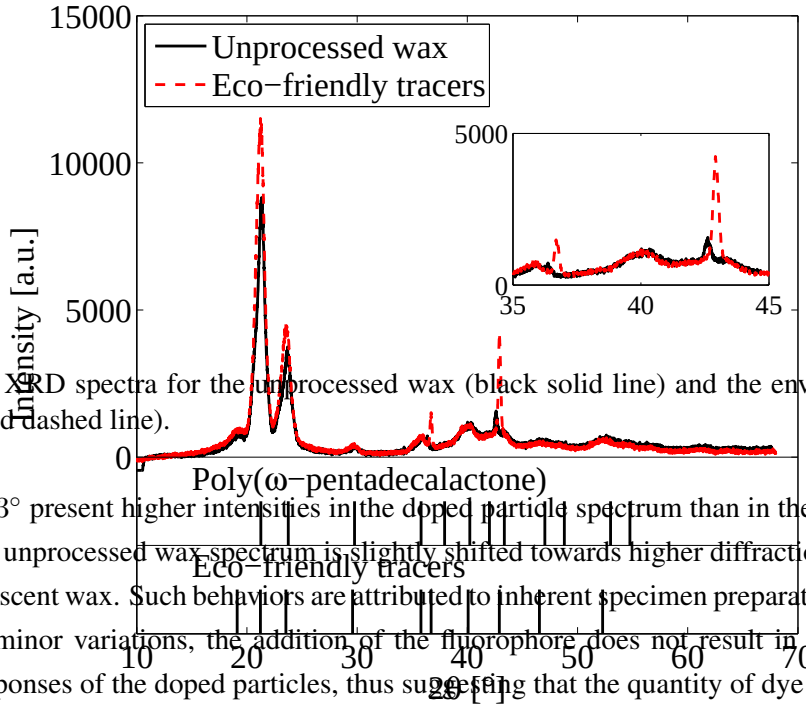

Figure 6.3: XRD spectra for the unprocessed wax (black solid line) and the environmentally friendly particles (red dashed line).

and $2\theta = 43°$ present higher intensities in the doped particle spectrum than in the unprocessed sample. Further, the unprocessed wax spectrum is slightly shifted towards higher diffraction angles with respect to the fluorescent wax. Such behaviors are attributed to inherent specimen preparation differences. Apart from such minor variations, the addition of the fluorophore does not result in significantly different spectral responses of the doped particles, thus suggesting that the quantity of dye inside the wax matrix is undetectable through XRD.

6.3.3 Transmission electron microscopy

Transmission electron microscopy (TEM) is performed on the environmentally friendly particles by using Topcon 002B and STEM-JEOL 2010F microscope equipped with electron energy loss and energy dispersive spectrometers (EELS and EDS) and operating it at $200\,\mathrm{kV}$. Samples are prepared by dispersing the particles in ethanol and sonicating the solution for 3 minutes. After sonication, a drop of the homogenous mixture is dropped on a lacey carbon film and allowed to dry before TEM observation. Results on particle morphology, crystal size, and elemental dye distribution are reported in Figure 6.4.

Specifically, Figure 6.4(a) is a bright field TEM image of the environmentally friendly beads showing the particles' surface morphology, including the nanorods and platelets visible in Figure 6.2(b). Figure 6.4(b) is a high resolution image of beads displaying a homogenous distribution of spherical

dye particles embedded in the beeswax matrix. Dye particles' size is estimated to range in the interval $1.51 - 3.73\,\mathrm{nm}$, with average diameter equal to $2.51\,\mathrm{nm}$. Figure 6.4(c) presents a dark field acquisition of the sample showing diffracted dye crystals. Figure 6.4(d) is a high resolution dark field image displaying surface texturing on the beads surface. Crystals are arranged along lines, which is likely due to self-assembly, quenching, or texturing phenomena. In Figure 6.4(e), a selected area diffraction pattern of the dyed beeswax is reported, demonstrating that the crystalline nature of the beeswax is preserved through the fabrication process. Calculation of characteristic inter-planar spacings (d-spacings) of the crystals from the diffracted pattern leads to d-spacing values comparable to those obtained from XRD analysis, see Table 6.1 and Figure 6.3. This result confirms that the minimal quantity of dye does not affect the particle crystal structure. On the other hand, the fluorophore is homogeneously embedded into the external layer of the beads, thus guaranteeing particles' visibility.

Table 6.1: Characteristic peaks from TEM analysis for the environmentally friendly particles as obtained from Figure 6.4(e).

TEM		
2θ	Intensity	d-spacing (Å)
19.11	1427	4.085
21.23	11960	2.868
23.54	4972	2.501
29.59	918.3	2.103
35.79	1105	1.237
36.72	1967	1.161
40.07	1565	1.069
42.91	4688	0.811
46.54	1005	0.707
52.28	1083	0.623

6.3.4 X-ray photoelectron and raman spectroscopies

X-ray photoelectron spectroscopy (XPS) is performed on the unprocessed and environmentally friendly particles and on the red dye fluorophore to assay their chemical composition. Thermo Scientific K-Alpha XPS system is used for the experiments. Measurements are performed with a monochromatic Ka Al source set to $1486.6\,\mathrm{eV}$ with a base pressure of approximately $2 \times 10^{-8}\,\mathrm{mbar}$. The resolution is determined from the full width at half maximum (FWHM) of the metal lines in a reference sample and is found to be approximately equal to $1.5\,\mathrm{eV}$ using pass energy of $50\,\mathrm{eV}$ for survey and $20\,\mathrm{eV}$ for high resolution spectra. The binding energy scale is aligned through the C1s peak at $284.2\,\mathrm{eV}$. In addition, flood gun is used when necessary to limit surface charging.

Survey spectra for the unprocessed and environmentally friendly wax beads and the red dye are conducted by operating the analyzer in the constant analyzer energy (CAE) mode and setting the energy to $200\,\mathrm{eV}$. A total of ten scans are performed on a field of view of $400\,\mu\mathrm{m}$ for each sample. The

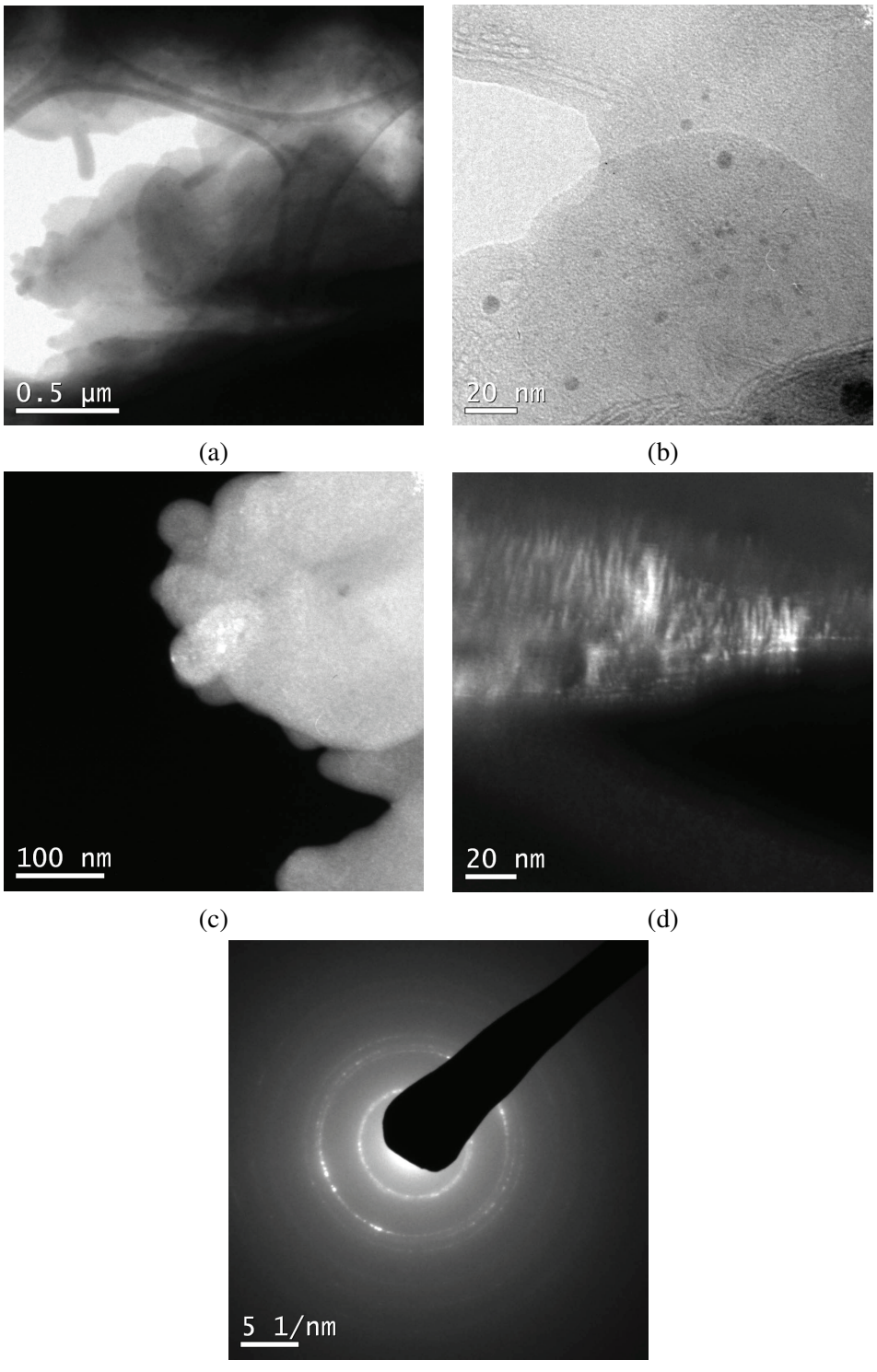

Figure 6.4: (a) Bright field TEM image of environmentally friendly beads showing the particles' surface morphology; (b) high resolution image of beads displaying homogenous distribution of spherical dye particles embedded in the beeswax; (c) dark field image showing diffracted dye crystals with an average size of $2.51\,\mathrm{nm}$; (d) high resolution dark field image showing surface texturing on the beads surface; and (e) selected area diffraction pattern.

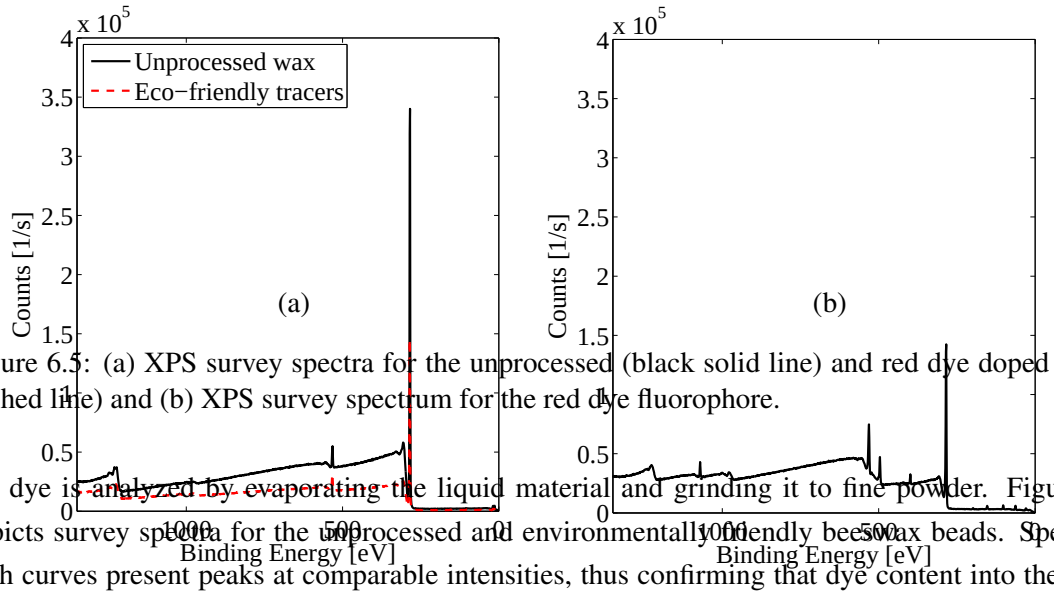

Figure 6.5: (a) XPS survey spectra for the unprocessed (black solid line) and red dye doped wax (red dashed line) and (b) XPS survey spectrum for the red dye fluorophore.

red dye is analyzed by evaporating the liquid material and grinding it to fine powder. Figure 6.5(a) depicts survey spectra for the unprocessed and environmentally friendly beeswax beads. Specifically, both curves present peaks at comparable intensities, thus confirming that dye content into the beads is minimal. On the other hand, differences in curves' intensity are not related to variations in materials' properties.

Figure 6.5(b) displays the survey spectrum for the red dye fluorophore. Further relevant parameters are reported in Table 6.2. Red dye analysis leads to the identification of the main chemical constituents of the fluorophore. Results show that there is no other element other than carbon and oxygen, which are the main constituents of unprocessed and doped beeswax, are detected. The presence of the dye in the doped wax is confirmed by the slight Si content (0.28% atomic content) see Table 6.2.

An etching test is performed where material on the surface of the environmentally friendly particles is incrementally scraped to assay the integration of the dye into the wax matrix. It is found that the Si content decreases after removing a layer of approximately $12\,\mathrm{nm}$ of material, thus suggesting that the fluorophore is mainly incorporated onto the surface of the beads.

Characterization of the samples is also conducted with Microraman spectroscopy (Renishaw Micro-Raman 2000 spectroscope) to study dye loading into the beeswax matrix. Due to particle fluorescence, a red laser at a near infra red $785\,\mathrm{nm}$ wavelength is used to maximize the Raman scatter of the specimens. Measurements are performed at room temperature. Figure 6.6 reports Raman spectra for the unprocessed wax and environmentally friendly beads. It is observed that specimens display intensity peaks at similar shifts. Conversely, an increasing broadening of the spectra is recovered around low Raman shifts

Table 6.2: Summary of the XPS surveys for the unprocessed and red dye doped wax and the red dye fluorophore. BE stands for binding energy, CPS for counts per second, FWHM for full width at half maximum, At. for atomic content, and PP for photoelectric peaks.

Sample	Element	Peak (BE)	Peak Height (CPS)	FWHM (eV)	Peak Area (CPS×eV)	At.%	PP Height (CPS)	PP At.%
Unprocessed wax	C1s	284.39	299321.25	1.59	927415.78	97.35	336420.29	97.86
	O1s	532.39	17289.16	3.24	62135.14	2.65	18080.94	2.14
Environmentally friendly beads	Si2p	101.93	75.5	1.17	132.12	0.28	88.61	1.39
	C1s	284.73	33320.49	1.27	49968.26	97.74	33744.34	96.21
	O1s	532.36	931.26	2.42	2482.35	1.98	1036.24	2.4
Red dye	C1s	284.46	124749	1.87	443108.95	80.94	138239.04	82.31
	O1s	531.3	38378.85	3.82	162439.93	12.07	42183.88	10.21
	N1s	399.07	7434.28	2.94	26186.15	2.87	8393.39	3
	Na1s	1071.07	11405.15	2.89	38668.3	1.8	12815.41	1.94
	Si2p	101.99	3051.52	2.87	10040.94	2.01	3445.68	2.25
	Cl2p	198.33	1014.16	3.72	4051.69	0.31	1129.66	0.28

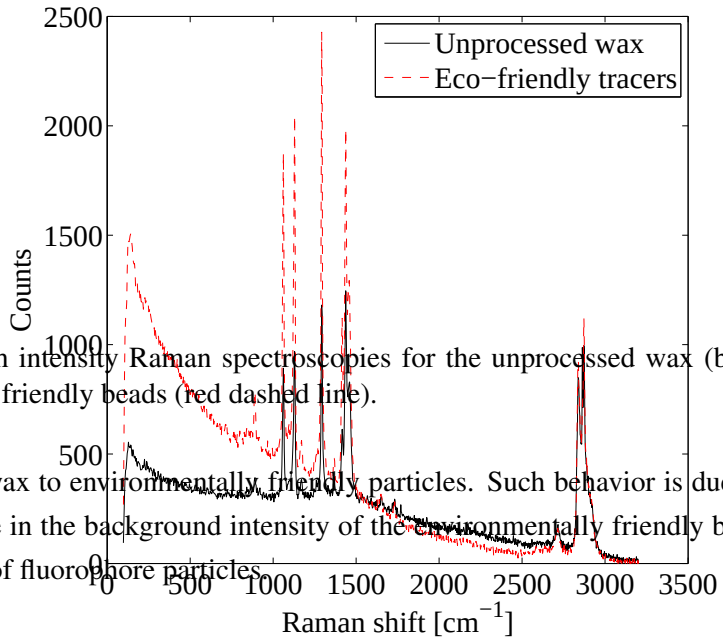

Figure 6.6: High intensity Raman spectroscopies for the unprocessed wax (black solid line) and the environmentally friendly beads (red dashed line).

from pure beeswax to environmentally friendly particles. Such behavior is due to fluorescent material doping. Increase in the background intensity of the environmentally friendly beads is another instance of the presence of fluorophore particles.

6.4 Exposure to weathering agents

Weathering agents, such as high energy light radiation and temperature can impact the lifetime of the fluorescence and affect the beeswax matrix. Specifically, photobleaching effects may cause the decay and disappearance of fluorescence emissions [144], whereas temperature may lead to shifted spectra [145]. The effects of high energy light and temperature on the fluorescence particles are preliminarily studied in [71] by designing ad-hoc experimental setups where the beads are continuously exposed to UV light at $365\,\mathrm{nm}$ and where a sample of $2\,\mathrm{g}$ of beads is deployed in stirred tap water at $50^{\circ}\,\mathrm{C}$ for approximately 12 hours per day. It is noted that similar studies are performed in case of fluorescence dyed organisms, see for example [146].

Fluorescence emissions are periodically monitored through nondestructive GloMax®-Multi Jr fluorometer measurements. These nondestructive tests allow for preserving the external bead surface, whereas measurements performed with the spectrofluorometer would require melted samples. The intensity of the specimens is acquired in fluorescence units (FSU) with two optical kits: the green module (excitation wavelength: $525\,\mathrm{nm}$ and emission wavelength: $580 - 640\,\mathrm{nm}$) and the UV-GFP module

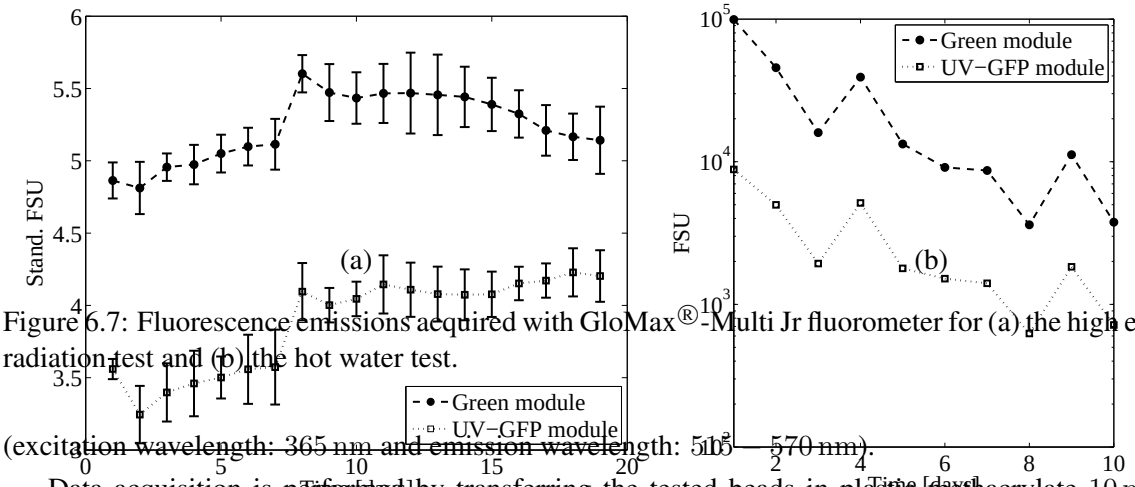

Figure 6.7: Fluorescence emissions acquired with GloMax®-Multi Jr fluorometer for (a) the high energy radiation test and (b) the hot water test.

(excitation wavelength: 365 nm and emission wavelength: 510 − 570 nm).

Data acquisition is performed by transferring the tested beads in plastic methacrylate $10\,\mathrm{mm} \times 10\,\mathrm{mm}$ cuvettes in the fluorometer. Before recording, samples are tapped to guarantee that the particles are closely packed in the cuvettes and, therefore, limit the presence of voids that may bias the optical data. After the weathering tests, samples are melted and analyzed with PTI Quanta Master 40 spectrofluorometer to compare emission spectra with initial fluorescence yields.

6.4.1 High energy radiation

In the high energy light experiment, samples of $0.5\,\mathrm{g}$ of environmentally friendly beads are stored in labeled petri dishes in a dark environment at $15\,\mathrm{cm}$ below an $8\,\mathrm{W}$ UV lamp and transferred in the methacrylate cuvettes for testing with GloMax®-Multi Jr fluorometer. The experiment is conducted for 26 days, for a total of 19 measurements. For each measurement, five acquisitions are taken at intervals of two seconds with both optical modules on each sample and averaged to characterize the sample behavior.

In Figure 6.7(a), fluorescence measurements for five and six environmentally friendly samples tested with both optical modules are reported. These findings suggest a significant increase in fluorescence yield for the initial eight measurements for both optical kits. Thereinafter, a decrease in the fluorescence intensity is detected with the green module. On the other hand, acquisitions with the UV-GFP module exhibit increasing or stable behavior probably due to permanent shifts of the spectra. These results suggest that overexposure of environmentally friendly beads to UV light radiation leads to irreversible fluorescence decay from molecule degradation.

6.4.2 Hot water

In the hot water exposure test, experiments similar to those in [71] are conducted for 12 hours a day for 20 days. Specifically, one sample of $0.5\,\mathrm{g}$ of beads is deployed in $100\,\mathrm{ml}$ of tap water kept under magnetic stirring at $350\,\mathrm{rpm}$ and at $50°\,\mathrm{C}$. Every other day the suspension is filtered with a $20\,\mu\mathrm{m}$ sieve and the particles are desiccated with silica gel for a few hours and then stored in methacrylate cuvettes for measurements with GloMax®-Multi Jr fluorometer. Five acquisitions of the emission intensities are taken at intervals of two seconds with both optical modules and averaged to characterize the sample behavior. Results are depicted in Figure 6.7(b). Fluorescence values measured with the green module are reduced of 96% and data recorded with the UV-GFP kit show a decrease of 92%.

Consistently with [71], emission scans performed on the melted material with PTI Quanta Master 40 spectrofluorometer do not display significant peaks in the emission spectra, conversely, spectra are constant at intensity values close to zero. Such behavior confirms the complete extinction of the fluorescence and suggests that fluorophore molecules are degraded and washed out during the thermal treatment. This is confirmed by qualitatively analyzing the opaque cyan coloring of the beads at the end of the experiment.

6.5 Laboratory feasibility analysis

The ability of the particles to trace complex surface flows is investigated by performing a proof-of-concept PIV laboratory experiment on the circular hydraulic jump generated by a water jet impacting a rigid wall. Hydraulic jump is studied using the setup in Figure 7.1, where water is recirculated through a piping system via a submersible Beckett Corp G210AG20 210 GPH pump and regulated through a diverting three-port ball valve and a butterfly valve. An electronic GPI A109GMN025NA1 digital flow meter is placed at proper distances from the valves to monitor the flow discharge. The jet is spread out from a brass straight-hose tapered nozzle, whose output diameter, $2a$, is equal to $5\,\mathrm{mm}$. The nozzle is located $5\,\mathrm{cm}$ above a horizontal $30 \times 30\,\mathrm{cm}$ polycarbonate plate. The plate rests on the bottom of a water tank through four aluminum legs; the lower side of the plate is covered with opaque material to enhance the fluorescence of the beads and improve their visibility. The depth of the water on the horizontal surface, d, is set to $2.5\,\mathrm{mm}$ through aluminum L-brackets installed along the edges of the plate. During each experiment, a few grams of fluorescent particles are seeded into the flow through an injection system and ejected through the nozzle onto the plate. A fluorescent $50\,\mathrm{W}$ lamp placed along a side of the water tank at $5\,\mathrm{cm}$ from the water surface excites the particle fluorescence. Figure 7.1 shows the particle motion for a representative case scored with a CMOS Canon VIXIA HG20 camcorder at approximately $50\,\mathrm{cm}$ from the plate.

PIV analysis are conducted with an IDT MotionPro 3 Series $1\,\mathrm{k} \times 1\,\mathrm{k}$ pixel color CMOS camera placed at $14\,\mathrm{cm}$ from the plate for image acquisition. Camera acquisition frequency is set to $300\,\mathrm{Hz}$, exposure time to $2353\,\mu\mathrm{s}$, and sensor gain to $+6\,\mathrm{dB}$. PIV experiments are performed by varying the

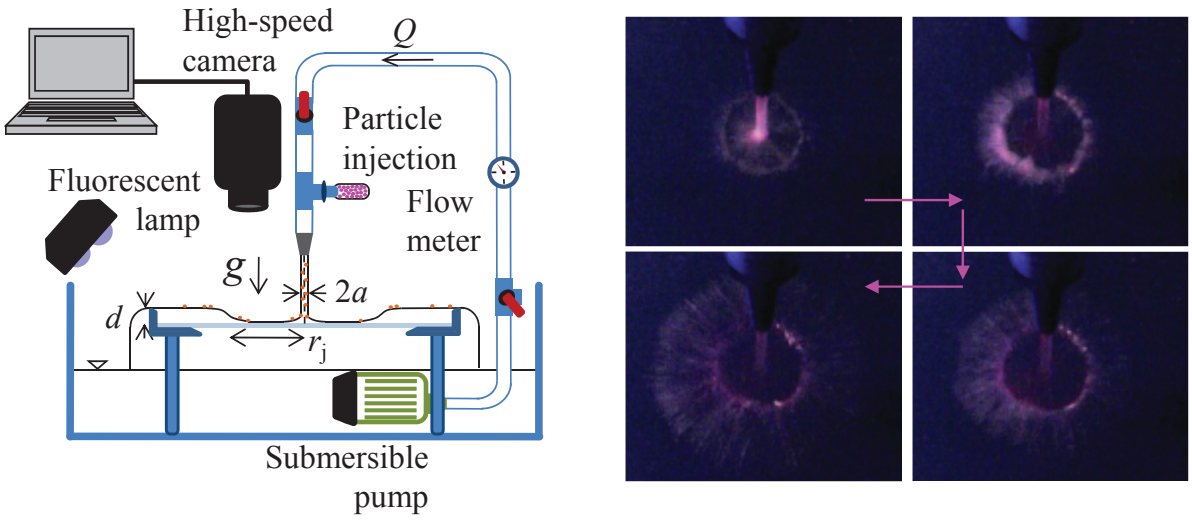

Figure 6.8: Left, experimental setup for the circular hydraulic jump experiment and right, snapshots depicting particle tracer ejection on the horizontal plate.

flow rate from 2.5×10^{-5} to $6.7 \times 10^{-5}\,\mathrm{m}^3/\mathrm{s}$ in increments of $0.8 \times 10^{-5}\,\mathrm{m}^3/\mathrm{s}$. After acquisition, a sequence of 50 frames sampled at intervals of $6.67\,\mathrm{ms}$ from the entire sequence of 2000 frames of a single experiment is used for processing. The sequence of 50 frames illustrates the trajectory of the particles from the impact of the water jet to few centimeters outside the circle. The processed field of view is equal to $7 \times 8\,\mathrm{cm}$ where the physical dimension of $1\,\mathrm{cm}$ corresponds to $122\,\mathrm{pixels}$ in images. The sequence of frames is analyzed through ed-PIV software. Each image is subdivided into $32 \times 32\,\mathrm{pixels}$ interrogation regions and cross-correlation is performed using a multi-pass fast Fourier transform.

For the analysis, a polar coordinate system is defined such that the origin is located at the center of the impact of the jet and the angle θ spans from $0°$ to $180°$, see Figure 6.9. After PIV processing, the radial component of the flow velocity is obtained and averaged over the 50 pairs of frames. Figure 6.9 depicts the contours of the time-averaged radial velocity field for the flow discharge $5.83 \times 10^{-5}\,\mathrm{m}^3/\mathrm{s}$. It is observed that the velocity inside the circular jump is much larger than outside; thus, particles in this inner region are scored as oblate ellipses, limiting the accuracy of PIV therein. This results in null velocity values inside the circular jump, see the blue contours inside the jump showed in Figure 6.9. Higher camera acquisition frequencies would be necessary to obtain better quality pictures and apply PIV inside the circle. On the other hand, particles are clearly visible outside the jump and they allow for reliably estimating the velocity field. The radial velocity field is experimentally estimated by computing time-averaged radial velocity profiles as a function of the distance from the jet impact for sectors of $10°$ spanning from $\theta = 45°$ to $\theta = 135°$, see Figure 6.9. Such sectors are selected due to the fact that they are located underneath the camera lens and are not affected by optical distortion and scarce illumination issues. The maximum radial velocity value in the $90°$ sector is referred to as U and the radius at which it is attained is termed $r_{\max}$. As a validation of PIV measurement, Fig. 6.10 compares

the direct measurement of the flow discharge $Q^{\star}$ with its estimate $Q = U(2\pi r_{\max} d)$ obtained PIV data. Results reported therein indicate that ratio between PIV and direct measurement is 0.860 with a standard deviation of 0.239, thus supporting the feasibility of using the proposed particles to study hydraulic jump especially for smaller values of flow discharges.

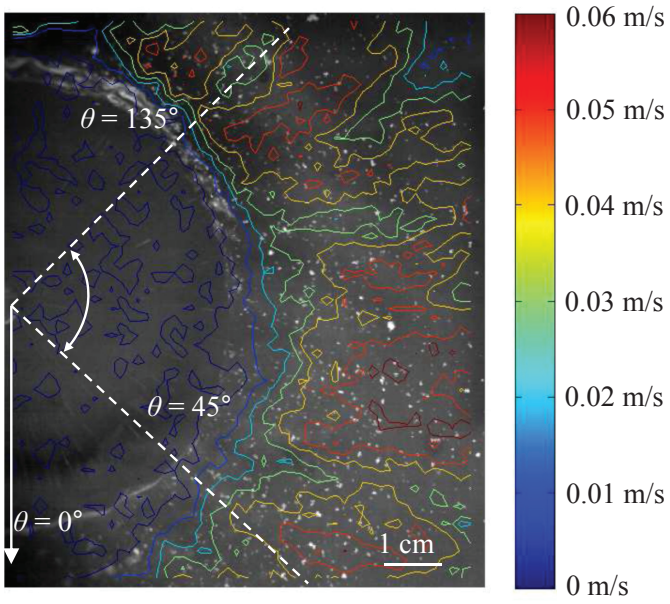

Figure 6.9: Radial flow velocity field for the circular hydraulic jump experiment depicting the polar coordinate system used for analysis. Flow discharge is $5.8 \times 10^{-5}\,\mathrm{m}^3/\mathrm{s}$.

To further investigate the potential of the proposed tracers in studying surface flow physics, PIV images are further analyzed to extract the radius of the circular jump [1] r_{j}, which is then used in conjunction with the estimate of the flow discharge Q to partially validate the model presented in [1]. Specifically, it therein demonstrated that r_{j} depends on relevant flow parameters through

$$\frac{r_{\mathrm{j}} d^2 g a^2}{Q^2} + \frac{a^2}{2\pi^2 r_{\mathrm{j}} d} = 0.01676 \left[\left(\frac{r_{\mathrm{j}}}{a} \right)^3 R^{-1} + 0.1826 \right]^{-1} \tag{6.1}$$

for $(r_{\mathrm{j}}/a) R^{-1/3} \geq 0.3155$, and

$$\frac{r_{\mathrm{j}} d^2 g a^2}{Q^2} + \frac{a^2}{2\pi^2 r_{\mathrm{j}} d} = 0.10132 - 0.1297 \left(\frac{r_{\mathrm{j}}}{a} \right)^{\frac{3}{2}} R^{-\frac{1}{2}} \tag{6.2}$$

for $(r_{\mathrm{j}}/a) R^{-1/3} < 0.3155$, where g is the gravitational acceleration and R is the jet Reynolds number, which is defined as $R = Q/\nu a$ with ν being the kinematic viscosity of water. Comparison with theoretical results is presented in Figure 6.10 where relations (6.1) and (6.2) are presented as a solid curve and markers refer to experimental results. Following [147], the left hand sides of Eqs. (6.1) and (6.2) are plotted against $(r_{\mathrm{j}}/a)^3 R^{-1}$ to facilitate comparison. The theoretical prediction in [1] is found to

generally overestimate experimental results with an error which increases as the Reynolds number increases. Similar evidence is reported in [1], where measurements are obtained without using a PIV system, yet, discrepancies between experimental and theoretical results observed therein are smaller than those found in this study. Such discrepancies may be due to theoretical factors, such as neglecting fluid surface tension [147], and experimental uncertainties associated to PIV practice, including spatial heterogeneities in particle seeding, light reflections from the water surface, distortions from the camera lenses, and unfavorable illumination conditions as compared to the high acquisition frequency.

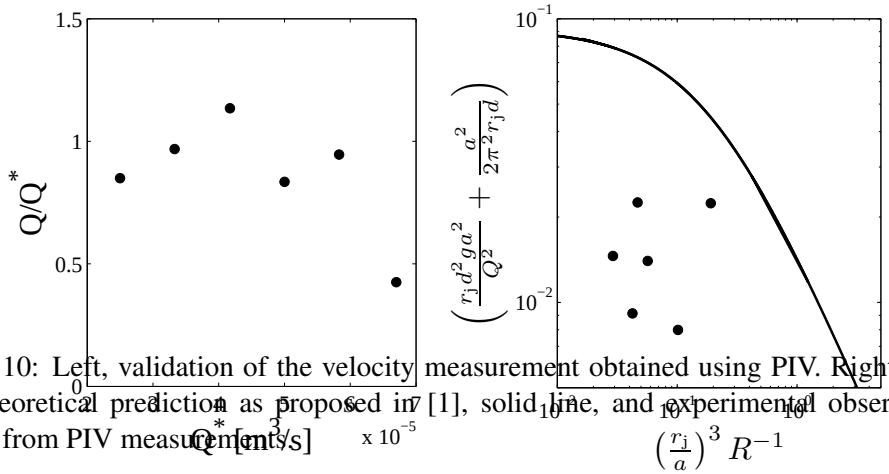

Figure 6.10: Left, validation of the velocity measurement obtained using PIV. Right, comparison between theoretical prediction as proposed in [1], solid line, and experimental observations, markers, obtained from PIV measurements.

6.6 Outdoor experimental application

A proof of concept experiment is conducted with the biocompatible fluorescent particles to assess their feasibility in tracing water flows in outdoor conditions by following the procedure in [76]. This represents a first step towards the development of an automated tracing methodology for surface hydrology. Specifically, a video depicting the transit of the particles in a water channel is analyzed through image analysis tools developed in [70, 72]. Such procedure allows for identifying the brightest objects in acquired videos, which are highly probable to depict the particle fluorescence.

The experiment is conducted in an outdoor environment where an ad-hoc setup is developed to detect the transit of the fluorescent beads. Specifically, the setup encloses a $2\,\mathrm{m}$ long and $22\,\mathrm{cm}$ wide reclinable polyvinyl chloride water channel and a portable sensing station, [73]. The water channel cross-section is concave and its bed is covered with soil and painted with bitumen to create a naturally rough surface. Water is injected into the channel through a hose and a valve is used to regulate flow discharge. The sensing station is composed of a $40\,\mathrm{cm} \times 100\,\mathrm{cm}$ wooden plate which rests on adjustable

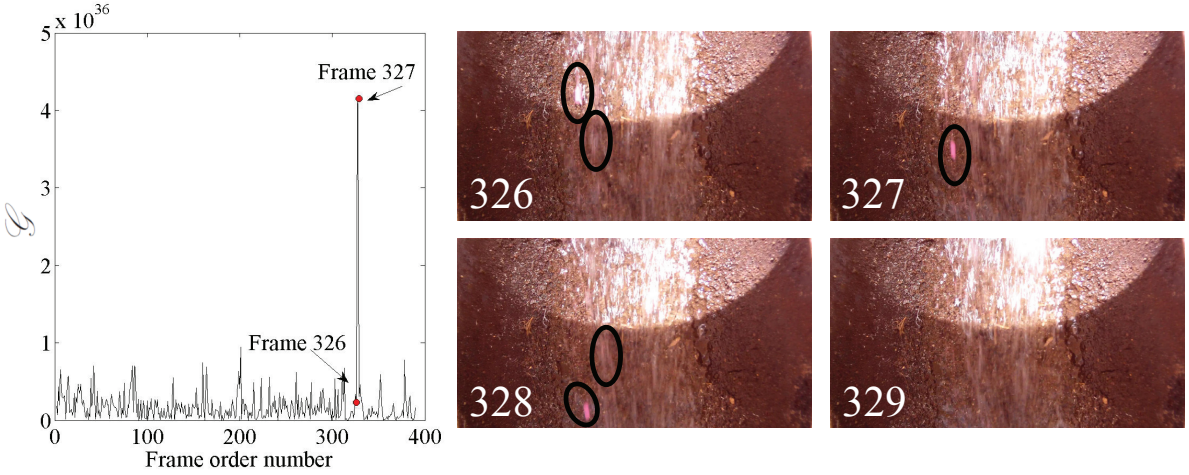

Figure 6.11: Left, time series of the index $\mathscr{G}$ for the analyzed video and right, snapshots depicting the transit of the particles underneath the camera. Black ellipses enclose environmentally friendly beads transiting in the field of view captured by the camera.

steel tripods. The bottom side of the plate hosts $80\,\mathrm{cm}$ strip of white LEDs mounted in series connection and a miniature water proof Bullet HD 1080p camera. In this test, the light source and camera are set to $40\,\mathrm{cm}$ from the water surface and flow velocity is estimated to be $2\,\mathrm{m/s}$ from preliminary measurements. Further, camera settings are fixed to Full HD resolution and $30\,\mathrm{Hz}$ frame rate. Environmentally friendly $250-420\,\mu\mathrm{m}$ are deployed for the proof of concept experiment.

The transit of the particles in the water channel is identified by converting recorded videos to RGB frames and then isolating the red channel. Gray scale images are then analyzed by using the index $\mathscr{G}$ defined in [72], that is,

$$\mathscr{G} = \frac{\sum\limits_{i\in\mathscr{I}} c_i^{\alpha} n_i}{\sum\limits_{i\in\mathscr{I}} n_i}, \quad \mathscr{I} = \{i \in \{0,1,...,255\} : n_i > 0\}, \tag{6.3}$$

with $n_i = n_i^p - n_i^b$. Here, n_i^b and n_i^p refer to the pixel count for the background and particle images, respectively. The term c_i^{α} represents the intensity classes from 0 to 255 where the power α is introduced to emphasize brighter pixels. In this experiment, the value of the power is set to 16 after preliminary analyses where α is varied from a low value of 2 to 20. Background images are obtained from the original ones by starting videos before particle deployment and then selecting initial frames. The introduced index $\mathscr{G}$ is computed on the cropped images where the only water surface is captured [83, 99].

Figure 6.11 reports image analysis findings for the selected video. Specifically, Figure 6.11(a) depicts the time series of $\mathscr{G}$. It is noted that a peak with value two orders of magnitude greater than the background values is found at frame 327. Snapshots corresponding to the peak are showed in Figure 6.11(b), where the transit of fluorescent pink particles is visible.

Chapter 7

Large scale flow monitoring

7.1 Introduction

Recently, profound interest has been devoted to the development of innovative observational methodologies for improved understanding of hydrological processes [148]. Among non-contact river gauging techniques, large scale particle image velocimetry (LSPIV) is a remote surface flow measurement methodology that enables the nonintrusive and continuous characterization of water bodies based on digital image acquisition [46, 149]. Such a technique has been utilized to estimate flow discharge in riverine environments [14, 41], flow patterns in limnological ecosystems [150], and hydrodynamic features in natural water bodies [151]. Different from river gauging measurements through current meters [152], acoustic doppler current profilers [153], and dye or chemical tracing [13, 18], LSPIV does not require either physical sampling or the presence of human operators for data acquisition [154, 155]. In fact, the methodology allows for safely monitoring extended areas in varying flow regimes, spanning from heavy floods to low flows [156, 157].

LSPIV is an extension of classical particle image velocimetry (PIV), an optical flow measurement technique that is used in laboratory environments to estimate the instantaneous flow velocity of seeded fluids [38–40]. More precisely, LSPIV implementations include: (a) a digital image acquisition system that is often installed at a considerable height (several meters) and angled with respect to the water surface to capture extended fields of view (FOVs); (b) highly visible surface flow tracers or patterns, which are carried by the flow; and (c) a processing unit to extract flow velocity from images [15, 134, 135]. After acquisition, digital images are orthorectified to eliminate distortions introduced by the angled camera and calibrate image dimensions and analyzed through cross-correlation PIV algorithms. Image orthorectification is performed by a photogrammetric relation between fixed ground reference points in the real environment and objects captured in digital images. The accuracy of this phase is crucial for velocity estimation and increases with the number of ground reference points [158]. Once orthoimages are generated, the motion of surface tracers or flow patterns is used to estimate surface flow velocity. Specifically, images are subdivided into interrogation windows that are cross-correlated

with larger search windows in consecutive frames to estimate the displacements of the tracers. During the process, interrogation windows are translated on a pixel grid superimposed on the pictures, and the flow velocity at each node of the grid is obtained by considering the time delay between consecutive images [40].

According to [158], LSPIV measurements are highly sensitive to the camera tilt angle and the associated process of image orthorectification. In particular, angled cameras introduce perspective distortions, in which near field objects are better resolved than the far field. After reconstruction, orthoimages may still display blurred shapes, thus leading to inaccuracies in velocity estimations greater than 17% [158]. Further, image orthorectification procedures rely on the acquisition of a minimum of four ground reference points, which are typically identified by means of a total station [158]. The identification of such points is deemed as the second major source of inaccuracies after seeding density [159], and represents a major hurdle in the implementation of LSPIV in inaccessible environments [155].

To mitigate inaccuracies related to image orthorectification and calibration, this chapter proposes a mobile and inexpensive sensing system, including a horizontal telescopic mast, a miniature and waterproof GoPro Hero 3 video camera, and a system of two lasers. The setup avoids image orthorectification by mounting the camera at one end of the mast with its axis perpendicular to the water surface. The reduced image coverage due to the camera orthogonality is compensated by the wide-angle GoPro lens, which enables large view capture of the center of the stream. The laser system creates visible points at a known distance on the water surface, allowing for nonintrusive calibration without dimensioning reference objects in the real environment through ground control points. The apparatus can be easily transported and utilized to survey diverse water bodies. Further, to allow for continuous monitoring of large scale environments, the system can be properly customized to be permanently installed underneath bridges or hosted on traveling-block cableways. Future applications of the system may also include its integration in autonomous aerial vehicles for environmental sensing [160].

To assess the performance of the apparatus, we conduct measurements on two different streams, the Aniene and Tiber rivers in Rome, Italy, to provide cases of varying flow regimes, illumination conditions, and surface tracer seeding densities. Specifically, the Aniene river exhibits torrential flow regime, abundant ripples induced by water reflections, and a meager number of buoyant tracers. On the other hand, the Tiber river presents lower surface flows, mirror-like reflections, and several inhomogeneously seeded floating objects. Captured images are corrected for camera lens distortion and analyzed with commercially available PIV software. Surface flow velocity estimations are compared to supervised measurements performed by visually tracking objects floating on the stream surface in acquired images and to rating curves developed by the Ufficio Idrografico e Mareografico (UIM) at Regione Lazio, Italy.

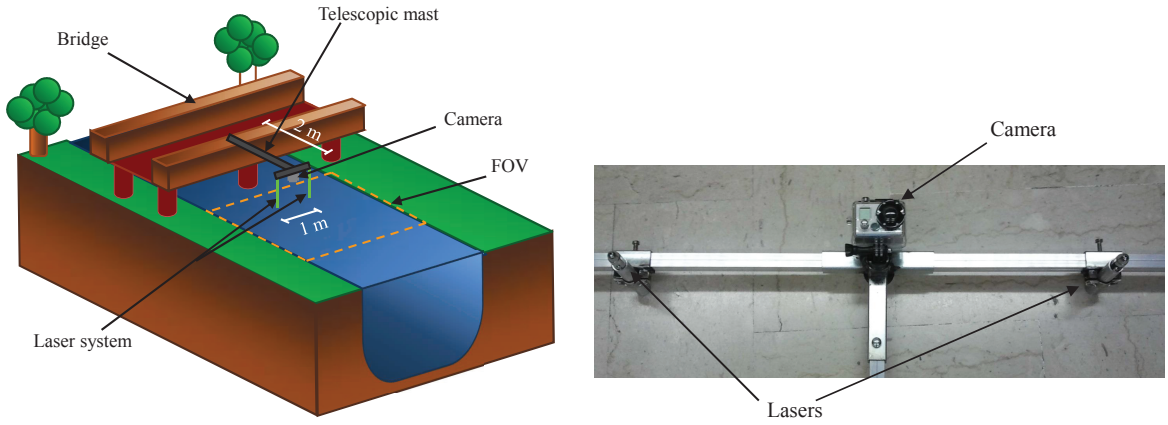

(a) (b)

Figure 7.1: (a) Sketch of the proposed LSPIV implementation and (b) close-up view of the aluminum frame hosting the camera and the laser system.

7.2 Experimental materials and methods

The video acquisition system includes a telescopic hollow aluminum bar that can be extended up to $2\,\mathrm{m}$. At one end of the bar, an orthogonal aluminum pole is connected as displayed in Figure 7.1(a). The pole is $1\,\mathrm{m}$ long and hosts two $1\,\mathrm{mW}$ green lasers at its ends, which emit at $532\,\mathrm{nm}$ wavelength. At the intersection of the pole and the bar, a GoPro Hero 3 video camera is encased in a waterproof box, see Figure 7.1(b). The camera axis is consistently kept perpendicular to the water surface throughout the experiments. Measurements are performed from river parapets by anchoring one end of the bar on the bridge railing and with the pole hanging out parallel to the stream surface.

Two vastly different study sites are selected for LSPIV tests. Specifically, one class of experiments is conducted on the Aniene river, Italy, where we deal with a torrential flow-regime and free-surface waviness. To assess the feasibility of the methodology in a more challenging scenario, we also execute measurements on the Tiber river, Italy, in low flow conditions and adverse visual settings.

Experiments on the Aniene river are performed at Ponte Salario ($41°56'22.20''\,\mathrm{N}$, $12°30'30.24''\,\mathrm{E}$) at the UIM gauging station $\mathrm{APS\_17}$. The station is located on a bridge and is equipped with the ULM20 ultrasonic water meter fabricated by CAE S.p.a. and positioned underneath the mid-span of the bridge at the upstream cross-section. Water levels are recorded at time intervals of 15 minutes, and discharges are obtained from the available rating curve. Further, UIM provides the bathymetry for the upstream and downstream cross-sections. Due to the larger presence of ripples, foam patterns, and water reflections, the downstream section is selected for LSPIV experiments, and its bathymetry is used for surface velocity estimations from the rating curve. At the time of the video based measurements, the water meter recorded a level of $1.6\,\mathrm{m}$ and a corresponding discharge of $32.52\,\mathrm{m}^3/\mathrm{s}$. From graphic estimates on the available bathymetry, the total wetted area for the measured water level is $27.24\,\mathrm{m}^2$, and, by assuming a velocity correction factor of 0.85, see [41], the average surface velocity is approximately $1.78\,\mathrm{m}/\mathrm{s}$.

Measurements on the Tiber river are conducted at the Ripetta monitoring station ($46°42'31.30''$ N, $29°05'34$ E) located at the mid-span of the local five-span bridge (Ponte Cavour). The UIM gauging station features a ULM20 ultrasonic water meter located underneath the mid-span of the bridge at the upstream cross-section, which records level measurements every 15 minutes. From the available bathymetry for the upstream and downstream cross-sections, a discharge of $354.17\,\mathrm{m}^3/\mathrm{s}$ is estimated for a level of $7.13\,\mathrm{m}$. By using the available bathymetric data, the total wetted area is estimated to be $680.77\,\mathrm{m}^2$, thus leading to an average surface velocity of $0.61\,\mathrm{m}/\mathrm{s}$ for the velocity correction factor set to 0.85. LSPIV videos are recorded at the center of the mid-span of the bridge at both the upstream and downstream cross-sections during the falling stage of the flood event that occurred on November, 14th, 2013, corresponding to meager quantities of floating material transported by the river.

The experimental dataset encompasses a set of eight videos recorded at Ponte Salario and ten recordings acquired at Ripetta. At Ponte Salario, videos of the downstream cross-section are acquired at time intervals of few minutes in the same day. At Ripetta, nine videos are captured from the upstream and one from the downstream cross-sections in a time span of three hours during the same day. Throughout the experiments, the camera is set to Full HD ($1920 \times 1080\,\mathrm{pixels}$) resolution and $60\,\mathrm{Hz}$ frame rate. Each video is approximately two minutes long, which corresponds to 7200 images.

Supervised flow velocity is estimated by manually tracking visible floating objects in consecutive sets of images. Image calibration is performed by equating the pixel distance between laser points from captured images to the known metric distance of the laser pointers on the aluminum pole. Specifically, for the Aniene river, the camera FOV captures a region of approximately $60 \times 35\,\mathrm{m}^2$, whereas videos performed on the Tiber river monitor an area of $37 \times 21\,\mathrm{m}^2$. Flow velocity is estimated to be equal to $4.50 - 4.70\,\mathrm{m}/\mathrm{s}$ in the Aniene river and to $2 - 2.3\,\mathrm{m}/\mathrm{s}$ in the Tiber river as per visual analysis on floaters transiting in the center of both streams. Such values are remarkably different from estimations from the rating curves, which are obtained by dividing the depth averaged streamwise velocity by the velocity correction factor.

7.3 LSPIV implementation

LSPIV is conducted by extracting consecutive sequences of 100 frames from each video. Images are corrected for lens distortion through the GoPro lens intrinsic parameters, as obtained from a preliminary calibration procedure. Further, two alternative methodologies are explored to minimize the effect of the vibrations due to the flexibility of the aluminum bar. Specifically, LSPIV implementations relying on the use of mast-mounted cameras or cableways may be severely affected by wind gusts, which result in slightly varying FOVs and inaccurate flow measurements. Techniques for the removal of unwanted vibrations are similarly developed in [161–163] to display identical FOVs in subsequent LSPIV images captured from aerial vehicles and in [164] to reconstruct images from a dual-camera system. More precisely, one FOV matching methodology entails the cross-correlation between a template image and

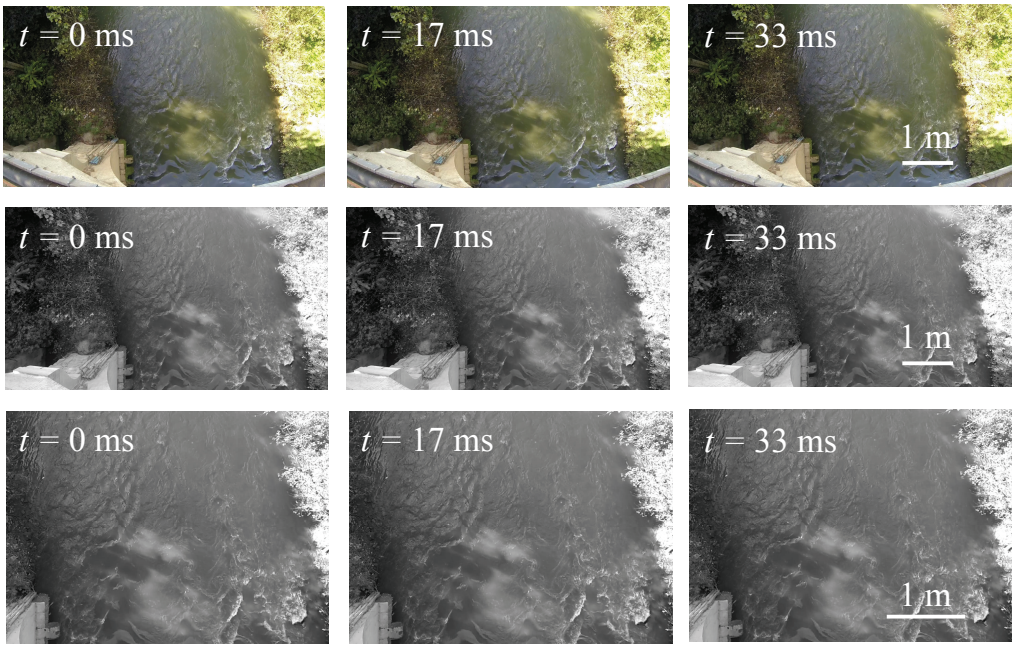

Figure 7.2: From top to bottom, raw, undistorted, and matched snapshots captured at 60 Hz of the Aniene river.

the sequence of pictures. Images are properly trimmed to depict overlapping FOVs as imposed by LSPIV processing. The template image represents objects on the river banks which are present in every picture. The alternative methodology consists of performing LSPIV on the raw sequence of pictures and then subtracting velocity components relative to fixed objects in the images, such as portions of the bridge, from the velocity of the water surface. PIV analyses are performed with the commercial software EDPIV [165].

7.4 Results

7.4.1 Aniene river

Figure 7.2 displays a sequence of frames captured at Ponte Salario on the Aniene river recorded at a 60 Hz frame rate from a representative experiment. In the top row, colored raw images from the GoPro camera are reported, and, in the second row, snapshots are corrected for fish eye lens distortions. Such correction results in gray scale pictures displaying smaller FOVs. In the last row, images are processed and trimmed to display identical FOVs for PIV analyses. Despite the considerable height of the camera with respect to the water surface (around 15 and 13 m for the Aniene and Tiber, respectively), the GoPro fish eye lens results in severely distorted FOVs. Further, it is noted that vegetation on the river banks creates large dark areas on the sides of the FOV, while a directly illuminated area is visible in the bottom central region of the pictures. The stream reach presents ripples and waves due to the high flow regime.

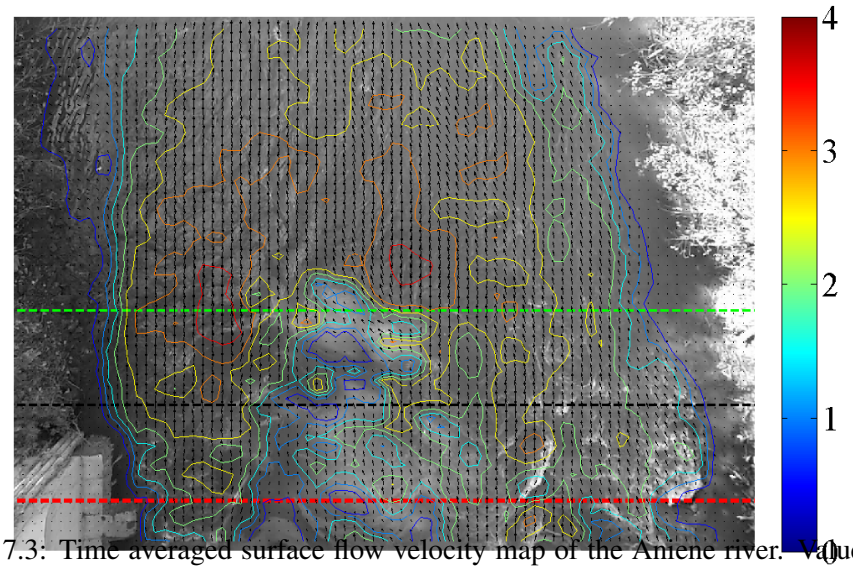

Figure 7.3: Time averaged surface flow velocity map of the Aniene river. Values are in $\mathrm{m/s}$. Dashed red, black, and green lines indicate cross-sections at 3, 8, and $13\,\mathrm{m}$ from the bridge, respectively.

In the right bottom corner of the images, stationary waves due to the stream bed roughness are also identifiable.

Figure 7.3 depicts a surface flow velocity map for a representative video, where black arrows are velocity vectors and colored contours indicate velocity values in $\mathrm{m/s}$. Velocity values are computed by averaging PIV estimations in time over the entire sequence of 100 images. No filtering or data post-processing is applied on displayed LSPIV data. Interestingly, PIV analysis accurately captures flow direction whereas low velocity values are obtained along the river banks in proximity of the vegetation. Unrealistic low velocity values are found in the bottom central region of the picture, where sunlight directly illuminates the water surface, see also Figure 7.2. Unrealistic low flow velocities are also obtained in the bottom right corner of the picture in correspondence of the stationary waves. By averaging the velocity values in the entire spatial domain, a mean flow velocity value of $2.05\,\mathrm{m/s}$ is obtained with index of variation equal to 0.41. Similar values are reported in Table 7.1 for the entire set of experiments.

In Figure 7.4(a), time averaged surface flow velocity profiles are reported for stream cross-sections located at 13, 8, and $3\,\mathrm{m}$ from the bridge for the same representative experiment in Figure 7.3. Specifically, for each selected section, velocities at each node of the PIV grid along the stream cross-section are averaged in time over the sequence of 100 frames. Due to the sunlight reflections in the bottom central area, low velocity values are gathered at $15 - 20\,\mathrm{m}$. Similarly, the surface flow profile in Figure 7.4(b) depicts lower values at $15 - 20\,\mathrm{m}$ and velocities up to $3\,\mathrm{m/s}$ are found in the center of the stream. Such profile is obtained by averaging velocities in time and over the entire set of stream cross-sections captured in the FOV.

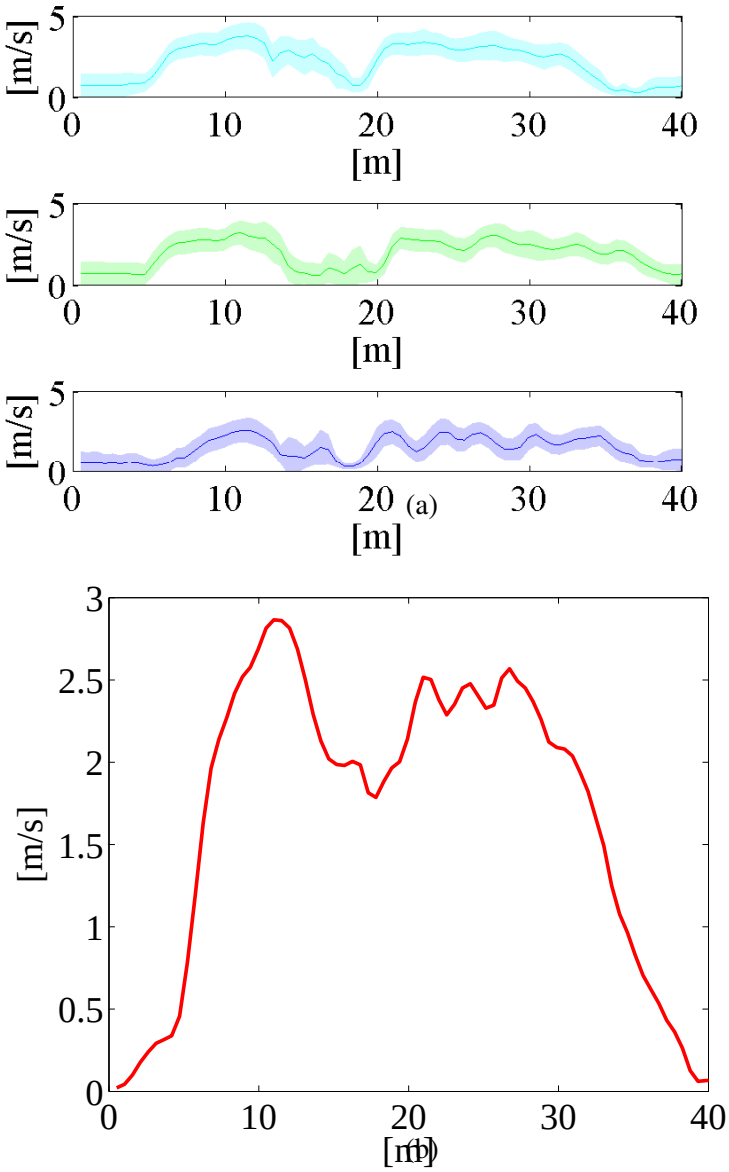

Figure 7.4: (a) From top to bottom, time averaged surface flow velocity profiles for the river cross-sections at 13, 8, and 3 m from the bridge obtained from a representative experiment. Shaded areas indicate the standard deviation over the sequence of 100 frames analyzed in this experiment. (b) Time averaged surface flow velocity obtained by averaging over the entire set of river cross-sections captured in the FOV for the same representative experiment. For this experiment, $v_{\mathrm{m}} = 2.05\,\mathrm{m/s}$ and $\beta_{\mathrm{v}} = 0.41$.

Table 7.1: LSPIV estimations and indices of variation for experiments performed on the Aniene and Tiber rivers. Values for v_{m} are in $\mathrm{m/s}$, whereas the parameter β_{v} is dimensionless.

Aniene			Tiber		
Test	v_{m}	β_{v}	Test	v_{m}	β_{v}
1	2.05	0.41	1	0.99	0.80
2	2.46	0.23	2	0.72	0.98
3	2.37	0.34	3	0.70	0.96
4	2.56	0.24	4	0.81	0.93
5	2.50	0.20	5	0.74	0.99
6	2.57	0.24	6	0.68	1.16
7	2.44	0.29	7	0.95	0.91
8	2.02	0.51	8	0.73	0.98
			9	0.91	0.78
			10	0.90	0.62

7.4.2 Tiber river

In Figure 7.5, a sequence of snapshots recorded at a $30\,\mathrm{Hz}$ frame rate is presented. In the top row, colored raw images are reported, whereas in the subsequent rows, images are corrected for fish eye lens distortion, matched to display identical FOVs, and reduced in resolution, respectively. Despite the bridge shadow, which creates a darker area in the bottom half of the pictures, images are homogeneously illuminated and water surface reflections are scarce. Several floating objects and debris are concentrated in the center of the stream. Yet, the limited dimensions of the objects and poor contrast with respect to the homogeneous background reduce the tracer visibility.

Figure 7.6 presents a time averaged surface flow velocity map of the Tiber river as obtained from PIV analyses, where each value of the grid is computed by averaging over the selected sequence of frames. Notably, velocity vectors do not describe realistic flow patterns and velocity values are almost everywhere close to zero due to the absence of appropriate tracers. Areas of higher flow velocities are concentrated in the center of the stream where the transit of floating objects is observed. Consistently, the time averaged velocity value over the entire spatial domain is estimated to be $0.99\,\mathrm{m/s}$ with index of variation equal to 0.80. Similar results for the entire set of experiments are illustrated in Table 7.1.

Figure 7.7(a) reports time averaged surface flow velocity profiles for cross-sections located at 13, 10, and $3\,\mathrm{m}$ from the bridge, where each value on the PIV grid along the river cross-section is averaged over the selected sequence of frames. Profiles are obtained for the same representative video analyzed in Figure 7.6. In this case, velocity values are almost constant for the entire stream span and do not sensibly decrease at the bridge piers. In Figure 7.7(b), the time averaged surface velocity profile further averaged over the stream cross-sections is equal to $1\,\mathrm{m/s}$ everywhere along the entire cross-section.

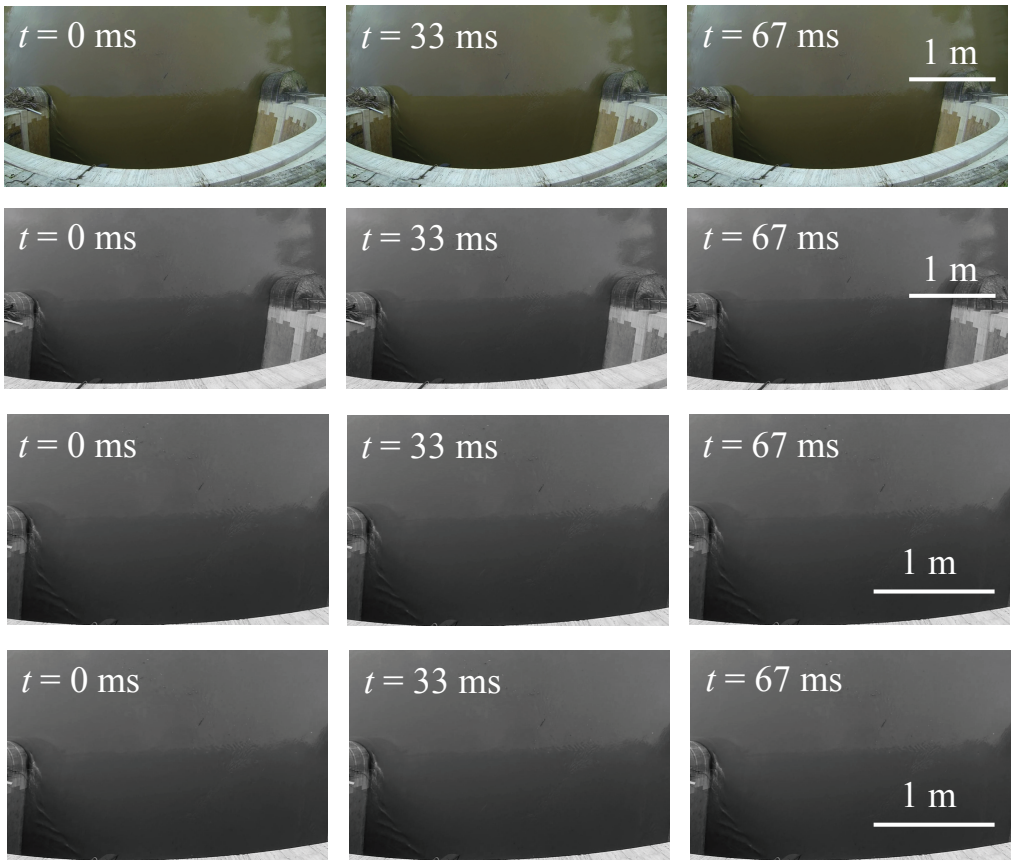

Figure 7.5: From top to bottom, raw, undistorted, matched, and lower resolution snapshots of the Tiber river captured at 30 Hz.

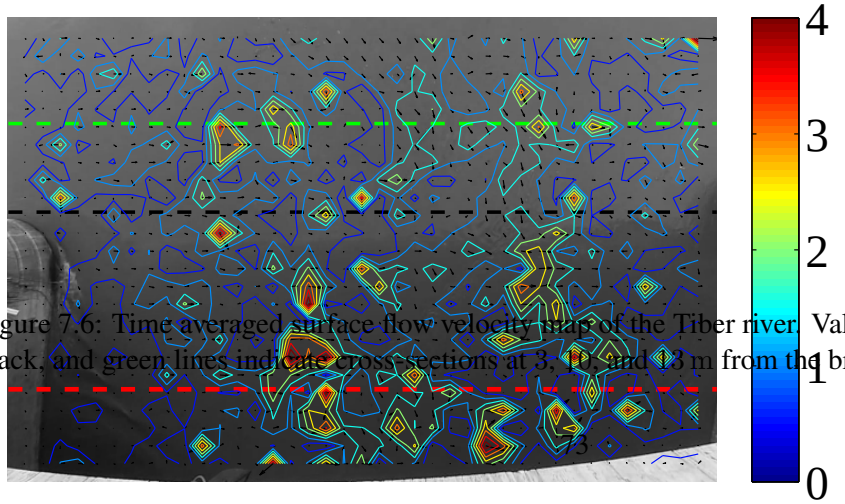

Figure 7.6: Time averaged surface flow velocity map of the Tiber river. Values are in $\mathrm{m/s}$. Dashed red, black, and green lines indicate cross-sections at 3, 10, and 13 m from the bridge, respectively.

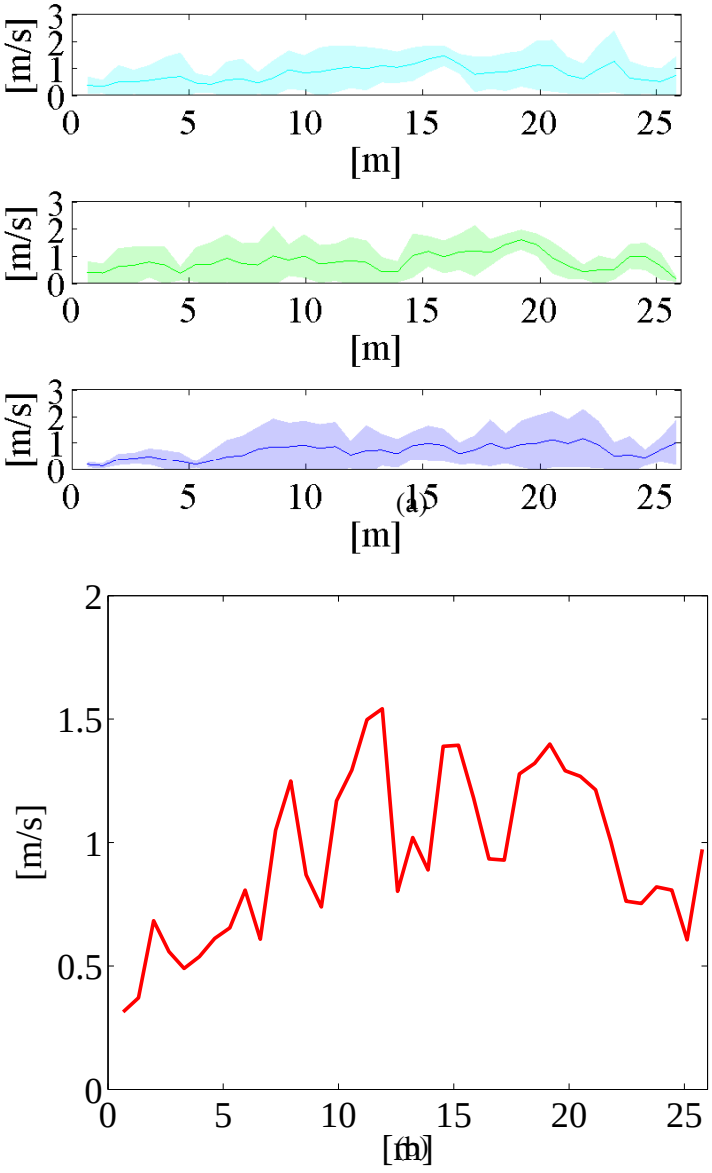

Figure 7.7: (a) From top to bottom, time averaged surface flow velocity profiles for the river cross-sections at 13, 10, and 3 m from the bridge obtained from a representative experiment. Shaded areas indicate the standard deviation over the sequence of 100 frames analyzed in this experiment. (b) Time averaged surface flow velocity obtained by averaging over the entire set of river cross-sections captured in the FOV for the same representative experiment. For this experiment, $v_{\mathrm{m}} = 0.99\,\mathrm{m/s}$ and $\beta_{\mathrm{v}} = 0.80$.

7.5 Discussion

While our results can be considered encouraging given the challenging experimental conditions, they draw the attention to two major issues. Specifically, flow velocities are consistently lower than estimations from the supervised methodology, and indices of variation are remarkably high. Flow underestimations are mainly attributed to the inhomogeneous density, or absence, of surface tracers. Indeed, in both experimental datasets, flow velocities that are close to predictions from the supervised analysis are observed at isolated locations in the center of the streams, where floaters are more likely to transit. High flow spatial heterogeneity is attributed to the large areas of null flow values recovered in proximity of the stream sides, in poorly illuminated regions, and in homogeneous visibility zones. For instance, with regards to the Aniene river, even if foam patterns and ripples were observable, several structures were stationary, thus resulting in unrealistic low velocities. In experiments on the Tiber river, given the poor contrast with the background and practical challenges in homogeneously seeding the entire river cross-section, little improvements were observed with the deployment of wax particles. Such unrealistic null velocity values highly contribute to lowering spatial averages and increasing indices of variation in Table 7.1.

Despite few locations in the stream center, velocity values obtained by averaging PIV data over the entire duration of the experiments also led to significant velocity underestimations. For instance, in Figure 7.8, we expand on Figure 7.4(a) by reporting boxplots for velocity values obtained at each node of the PIV grid along the selected cross-sections for the entire 100 frame sequence. Specifically, edges of the filled boxes indicate the 25% and 75% percentiles, circles refer to mean velocity values, error bars display minimum and maximum data points, and squares show outliers. The shaded red horizontal stripes indicate flow velocities estimated through manual tracking on floaters transiting in the center of the stream. From Figure 7.8(a) to (c), the distance from the bridge, and therefore from the adversely illuminated area, decreases, thus resulting in generally lower velocity profiles. As expected, the variability and the number of outliers are high, suggesting that velocity estimations depend on the irregular transit of surface tracers and flow patterns. Conversely, in the poorly illuminated area (see values from 16 to $21\,\mathrm{m}$ from the left river bank), the density of outliers decreases, thus indicating a region of critical visibility. Resting upon evidence in Figure 7.8, we plot in Figure 7.9 velocity contour and color maps obtained by considering the 85% percentile rather than averaging velocity values with respect to time. In this case, surface velocities are much closer to estimations from the supervised tracking procedure, while still accurately describing flow regime in the entire FOV. Low flow values faithfully relate to the side of the stream and to the critical visibility area.

While our findings confirm the promise of LSPIV for monitoring water bodies, they indicate that its accuracy is highly dependent on the transit of visible flow patterns. In case of torrential flows, LSPIV is expected to lead to more reliable surface velocity fields than low flows. Nonetheless, the detrimental effect of irregularly transiting tracers and stationary patterns should be accounted for by analyzing variations of the velocity field estimated by PIV during the time of observation. For this purpose, we

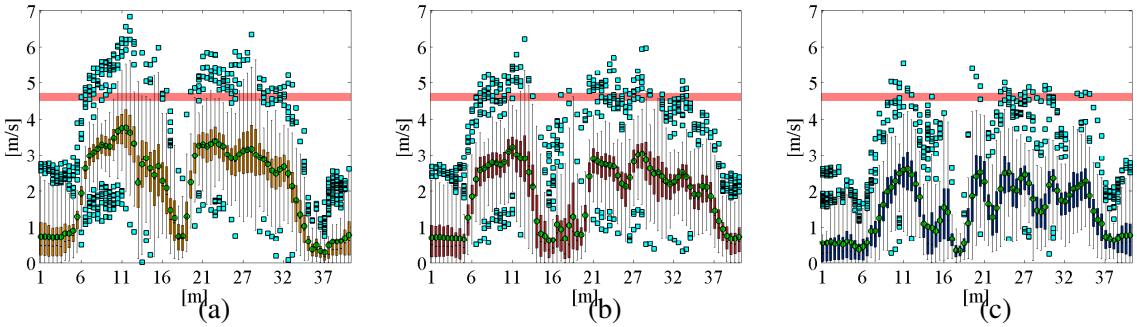

Figure 7.8: Boxplots for velocity values obtained from PIV analyses at cross-sections located at (a) 13, (b) 8, and (c) 3 m from the bridge on the Aniene river. Red stripes show supervised benchmark flow values.

expect that sensitivity analyses on the dependence of LSPIV data on flow conditions will aid in the selection of adequate velocity percentiles to systematically create velocity maps analogous to those in Figure 7.9. These preliminary calibration analyses can also contribute to the improvement of LSPIV-based rating curves [68]. Specifically, LSPIV-based discharge estimations are currently performed on selected cross-sections by considering the time averaged surface velocity values computed at the nodes of the PIV grid. Based on our findings, more accurate estimations may be attained by: (i) studying time variations of velocity data and investigating their relationship with flow conditions; (ii) removing null or unrealistic velocities attributable to the absence of tracers or poor illumination in the entire FOV; and (iii) developing a representative cross-section by averaging over the stream transects captured in the FOV.

While such measures could improve estimations on the Aniene river, in the low flow conditions experienced on the Tiber river, flow measurements were particularly challenging due to the almost complete absence of clearly visible surface patterns. According to [134], the accuracy of LSPIV estimations is highly related to the presence of properly seeded water surfaces and the combination of tracer poor visibility and scarce illumination has led to a maximum error of 35% in flow velocity estimations in [134, 159]. In some instances, artificial seeding has been necessary to compensate for the absence of moving patterns, see for example [44, 68]. Alternatively, LSPIV implementations have been performed in proximity of water falls or bridge piers, thus exploiting surface foam and ripples as tracers [41, 136]. In our study, even manually seeded floaters on the Tiber river were not sufficient to improve velocity estimations, and we expect such challenges to be exacerbated in case of larger FOVs, where massive seeding apparatuses would be necessary. In this framework, we suggest that LSPIV measurements should be preceded by feasibility studies on the identification of proper highly visible tracers to accurately seed the flow. In future studies, we will investigate the combined use of buoyant fluorescent particles [74–76], UV or LED illumination, camera filters, and polarizers to remarkably enhance LSPIV measurements.

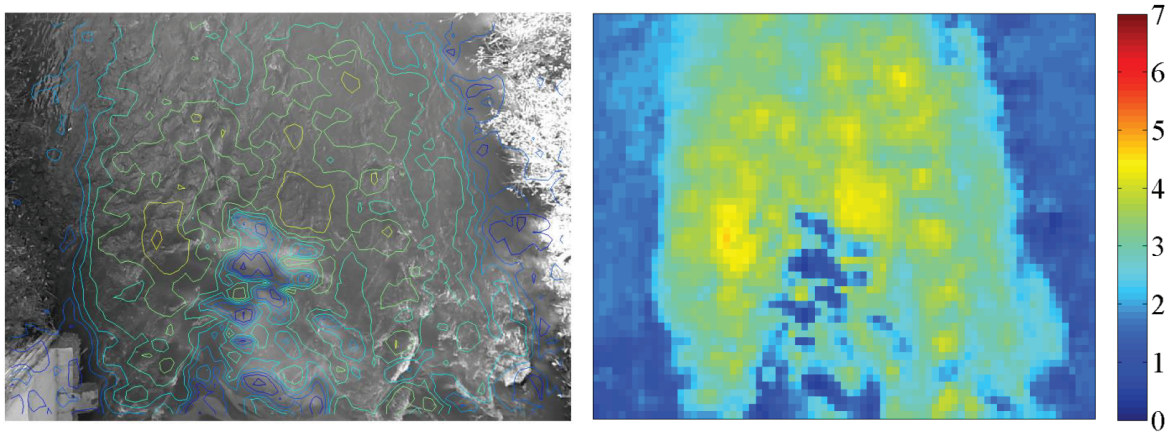

Figure 7.9: Left, contour and right, color maps for the 85% percentile velocity values estimated from PIV. Values are in $\mathrm{m/s}$.

7.6 Aerial LSPIV

In this paragraph, we present results based on the use of an aerial vehicle for LSPIV. The design, development, and feasibility tests of the vehicle were conducted by Mr. Christopher Pagano in the framework of his Master's thesis. I served as Mr. Pagano's graduate mentor during his B.S. and M.Sc.

To compensate LSPIV limitations due to the acquisition of ground reference points and image orthorectification, here, we present the development of a custom-built unmanned aerial platform for surface flow monitoring through LSPIV. Specifically, we design and develop a quadricopter equipped with a digital acquisition device to acquire image sequences of water bodies for PIV processing. We select a quadrotor helicopter design, which is an unmanned aerial vehicle that consists of four fixed pitch propellers, allowing for vertical takeoff and landing (VTOL). Such capability is of fundamental importance to perform flow measurements in confined areas typical of remote and ungauged environmental settings, where the absence of runways and open spaces prevents the use of alternative types of aircraft [160]. In addition, due to the simplicity of their fixed propulsion system, quadricopters are highly stable while requiring much less maintenance than helicopters [166]. The vehicle is equipped with an ad-hoc camera gimbal that isolates the camera from the quadricopter's vibrations and maintains its axis perpendicular to the water surface. This approach prevents the need for the acquisition of ground reference points for image orthorectification. To further mitigate inaccuracies due to mobile image capture, we develop a computationally fast procedure for identifying overlapping FOVs in sequences of consecutive frames. Experiments are conducted to assess the performance of the vehicle, including its flight time and hovering ability. To demonstrate the feasibility of environmental monitoring, we conduct preliminary tests in an outdoor controlled environment where the quadricopter acquires pictures of particle tracers flowing on the surface of a miniature water tunnel. In addition, we perform LSPIV on a stream in Prospect Park, Brooklyn, New York, to experiment with natural conditions. In both tests, surface flow velocity

Figure 7.10: View of the vehicle realization.

estimations are compared to measurements performed on videos acquired from a fixed camera.

7.7 Hardware description

Here, we describe the quadricopter design and sensing components. The vehicle's multirotor configuration enables a wide range of flight speeds, from hovering up to velocities of several meters per second, and also offers enhanced speed control when compared to fixed wing aircrafts and dirigibles [160, 167, 168]. Accurate and flexible speed control is crucial for the sensing platform to perform LSPIV analyses in natural settings, where flow regimes often exhibit large spatial and temporal variations [156]. To allow for high quality measurements in complex outdoor conditions, such as heavy wind gusts, the quadricopter is built with a resilient frame structure and hosts an active camera gimbal. The quadricopter design is modular and customizable to enhance its portability and minimize the maintenance, while being able to host a sensory payload of up to $500\,\mathrm{g}$. The cost of the prototype is approximately $1,700, including all the electronics and hardware components, thus offering a valid alternative to off-the-shelf aerial vehicles [169, 170]. Specifically, the upgrade of commercially available quadricopters to LSPIV would either require a considerable weight increase at the expense of maneuverability or the use of highly expensive industrial platforms [166, 171].

The quadricopter frame is based on an "X" configuration, where four equal length arms are connected in the center of the vehicle to allow for large payloads and enhance the vehicle stability. In particular, the "X" frame is characterized by equivalent moments of inertia about the roll and pitch axes, which is beneficial for accurate position-holding and high quality video acquisition. Such configuration also provides good maneuverability and minimum obstruction of the FOV to the ground-facing camera when the vehicle changes its orientation. The quadricopter adopts a high wing configuration, whereby the center of gravity (COG) is located above the vehicle's center of mass (COM), further enhancing its stability. This generates a moment about the COG that resists the variation in orientation [172]. The frame arms are built out of $3/8'' \times 3/8''$ aluminum c-channels surrounded by $1/32''$ carbon fiber strips.

Aluminum plates are used to reinforce the joints connecting the arms in the center of the frame. Carbon fiber plates house the electronics and are connected to each other independently of the frame through standoffs. This allows to build modules that can be easily mounted on the rest of the structure, through four bolts with locknuts placed through the frame. Such a design facilitates the transportation of the quadricopter in a disassembled form.

The landing gear consists of aluminum u-channels that are supported on the bottom of each leg just below the motor by larger aluminum u-channels. The larger u-channels are used to create a hinge that allows the remainder of the leg to pivot when landing, thus compressing a spring loaded piston. The compression of the piston absorbs some of the energy of the impact due to landing, and, thus, reduces the likelihood of damage to the vehicle. The bottom of the leg holds a light-weight plastic wheel that allows the leg to pivot without friction.

The quadricopter's thrust is produced by four $35\,\mathrm{A}$ Great Planes Rimfire brushless DC motors. The motors are mounted at the far ends of the four frame arms, and are configured such that adjacent motors spin with opposing direction. When the motors produce the same thrust, this configuration leads to a null net angular velocity, whereby the vehicle does not rotate about the yaw axis [160]. Each motor is connected to a $35\,\mathrm{A}$ Great Planes Silver Series electronic speed controller (ESC) with a battery eliminator circuit through three $3.5\,\mathrm{mm}$ bullet connectors. The Ardupilot, an open-source Arduino based microcontroller, controls the motors through a pulse width modulation (PWM) signal. The motors and the Ardupilot are powered by a $3\mathrm{S}\ 11.1\,\mathrm{V}$ (3-cells at $3.7\,\mathrm{V}$ each) lithium polymer (LiPo) battery with a $5000\,\mathrm{mAh}$ capacity. The quadricopter is controlled using a Spektrum DX6i 6-channel remote transmitter and a Spektrum DSMX 6-channel receiver. The receiver is connected to the transmitter, and the channels are connected to the appropriate input pins as defined in the Ardupilot manual [173]. The electronics account for approximately half of the weight of the vehicle.

The GoPro Hero3 Black edition is selected for image acquisition based on its limited weight ($\approx 53\,\mathrm{g}$) and small size ($41\,\mathrm{mm} \times 59\,\mathrm{mm} \times 31\,\mathrm{mm}$). The GoPro is able to capture videos at high frequency and with sufficient resolution for PIV ($240\,\mathrm{Hz}$ at WVGA resolution) [40]. The camera also allows for creating a Wi-Fi network, in which the device can be controlled through a remote or smartphone application. Therefore, camera's settings, including frame rate and FOV, can be modified midflight. The camera is characterized by a considerable fish eye effect, which allows for capturing data over large FOVs. On the other hand, images require significant preprocessing to remove lens distortion for PIV analysis.

A camera gimbal is designed to alleviate the effect of the quadricopter vibrations and to maintain the camera axis perpendicular to the water surface. The gimbal is engineered to compensate for two degrees of freedom, namely, pitch and roll, which affect the perspective of the captured images. Further, it is designed to be attached to the quadricopter, while being isolated from the frame. This prevents the vehicle vibrations from being directly transferred to the camera, thus reducing unwanted distortion in the images.

7.8 Image processing

Here, we describe the offboard image-based analysis procedures that are developed and implemented to perform LSPIV from the quadricopter. Briefly, pictures are first analyzed to remove the camera lens fish eye effect, and, then, a FOV matching methodology is applied on the frames before PIV analysis.

7.8.1 Lens calibration

To remove the GoPro fish eye effect, the MATLAB image processing toolbox "Camera Calibration Toolbox for Matlab" is implemented on sequences of acquired pictures [174]. This open-source toolbox aids in determining the calibration parameters controlling the degree of distortion of the lens as described in [175, 176]. Specifically, a calibration is preliminary performed by estimating the degree of distortion of a sequence of images of a checkboard grid captured with the camera, where each image depicts different perspectives of the grid. Calibration parameters obtained for the grid, such as the grade of radial and tangential distortion, are used to undistort experimental pictures. Since the fish-eye distortion compresses a large area into each frame, the undistorted frames appear stretched and larger than the original images.

7.8.2 FOV matching

Due to limitations in the hovering capability of the quadricopter, consecutive images acquired from the vehicle depict slightly different FOVs. Application of PIV on these images would result in unrealistic displacements; thus, images are reoriented and trimmed to depict overlapping regions of interest. The methodology entails the selection of a fixed portion of a picture, a so-called template, which is treated as a reference to reorient images. More precisely, by cross-correlating the template with a sequence of images and reorienting the pictures to overlap the locations of the template, identical region of interests are obtained. The reorientation is achieved using an affine transformation that preserves points, straight lines, and planes. Such a method works efficiently when the template lies on the same plane of the region of interest, that is, the water surface. In particular, while the locations of the template are kept undistorted for optimal matching, most of the picture is deformed and objects lying on planes different from the template's plane may appear slightly stretched.

7.8.3 PIV analysis

PIV analyses are performed by using PIVlab 1.32 MATLAB toolbox [177]. Particle seeding is often not feasible in LSPIV implementations, so that PIV is performed on floating objects on the water surface [41]. This requires a delicate trial and error procedure to calibrate the parameters of PIV analysis. In this study, the interrogation window size is set to be small enough to allow for the observation of small variations in velocity across the area of interest, yet it is chosen to be large enough to depict

densely seeded areas. Further, the optimal step size is defined as half the interrogation window size, so that each area is covered twice during analysis.After PIV analysis, instantaneous flow velocity maps are developed for each image. Time-averaged velocity fields are subsequently evaluated by computing average flow values over a sequence of consecutive images.

7.9 Results

Here, we present results for the experimental characterization of the feasibility analyses conducted in outdoor settings.

7.9.1 Water tunnel testing

Feasibility experiments are conducted by using the portable water tunnel described and calibrated in [73]. Disc-shaped paper particles of $7\,\mathrm{mm}$ diameter are used as tracers, and images are captured from the quadricopter as it hovers over the midpoint of the tunnel. To provide a reference flow velocity, results from these experiments are compared to findings from pictures captured with a fixed camera positioned above the water tunnel following the procedure presented in [73]. Specifically, the GoPro camera is installed at $1\,\mathrm{m}$ above the water surface and perpendicular to the flow for static acquisitions. The camera FOV captures an area of $1.5 \times 0.9\,\mathrm{m}^2$ at Full HD resolution and $60\,\mathrm{Hz}$ frame acquisition rate. Flow velocity data are obtained by visually tracking objects in consecutive sets of images [73].

Images from the quadricopter are taken at Full HD resolution and $60\,\mathrm{Hz}$ frame rate. Each image depicts a region approximately equal to $10 \times 30\,\mathrm{cm}^2$ and three experimental repetitions are performed. Preliminary PIV tests are conducted on a sequence of 22 consecutive frames by varying the interrogation window size and step. Mean velocities are obtained by averaging the values in the entire FOV and by further averaging over the captured sequence of frames. The optimal interrogation area size is set to 32×32 pixels, which leads to average velocities comparable to values estimated from the fixed camera. Further, such interrogation window size corresponds to an area sufficiently larger than the seeded tracers' dimension. Consistently with reference values from the fixed camera, an average velocity of 0.5 m/s is gathered across the water tunnel.

7.9.2 Experiments in Prospect Park, Brooklyn

Experiments are also conducted over a natural water stream in Prospect Park, Brooklyn. Full HD videos are taken at 60 Hz acquisition frequency from the quadricopter flying over the Binnen Falls, whereby algae blooms are used as surface water tracers. Images are reoriented and transformed using a 250×250 pixels template.

PIV analyses are performed on a sequence of 12 Full HD resolution images depicting an area of approximately $3.5 \times 2\,\mathrm{m}^2$ and by setting the interrogation window size to 32×32 pixels. Frame rate is

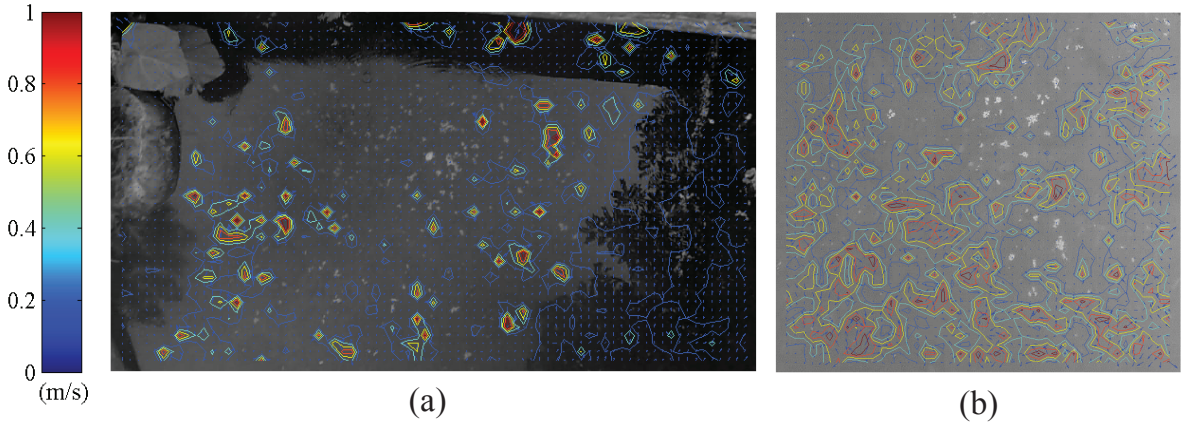

Figure 7.11: Time averaged surface flow velocity maps for images captured from (a) the quadricopter's onboard GoPro while hovering above the Binnen Falls, Prospect Park, Brooklyn and (b) a fixed camera.

set to $60\,\mathrm{Hz}$. Figure 7.11 displays time averaged surface flow velocity maps for images captured by the quadricopter and a set of 27 pictures acquired from a fixed Canon VIXIA HF R300 camcorder installed at $4\,\mathrm{m}$ from the water surface. These acquisitions capture an area of $2.7 \times 1.6\,\mathrm{m}^2$ and are recorded at $30\,\mathrm{Hz}$ frame rate and Full HD resolution. An average velocity of $0.12 \pm 0.08\,\mathrm{m/s}$ is estimated for images from the aerial vehicle, which is in good agreement with flow data from the fixed camera. Specifically, flow velocity evaluated from a sequence of 27 images captured with the Canon camera and analyzed through PIVlab with $32 \times 32\,\mathrm{pixels}$ interrogation window size is equal to $0.08 \pm 0.07\,\mathrm{m/s}$. The slight velocity overestimation obtained from images acquired from the quadricopter should be attributed to inaccuracies introduced by the FOV matching procedure. Specifically, since the template is slightly above the water surface, perspective errors in the image transformation may distort the FOV.

7.9.3 Discussion

In this chapter, we have discussed the design and development of a compact aerial sensing platform for LSPIV measurements in outdoor environments. Unlike commercially available amateur-grade quadricopters, our design is highly resilient to perform accurate digital video acquisitions in inclement weather conditions and has a remarkable payload capacity to host several sensing components. Despite heavy payload and power-hungry onboard sensing units, we obtained flight times of $4 - 5$ minutes, which are sufficient for characterizing natural surface flows. Further, from a maneuverability perspective, flight avionics allowed for good hovering performance in windy conditions, up to $16\,\mathrm{mph}$.

Experimental findings demonstrated that the platform can be effectively used for aerial LSPIV measurements. In particular, the use of the active gimbal prevents time-consuming image processing required by frame orthorectification and has reduced uncertainties related to the identification of ground control points. Notably, surface flow velocities from quadricopter-based LSPIV are comparable to fixed

LSPIV and particle tracking measurements.

While acquisitions from the ground-facing orthogonal camera did not require image orthorectification, the identification and measurement of ground control objects by human operators was needed for calibrating the images. This issue is currently being addressed by developing a calibration system which includes multiple onboard laser pointers. Ground-facing lasers installed at known distances on the quadricopter landing gear are expected to create reference shapes on the water surface that will be used to both calibrate images and infer the altitude of the vehicle. The laser shapes on the water surface are also likely to simplify the FOV matching procedure by providing a reliable ground reference pattern to be used as template. The system will not dramatically affect payload and will be only periodically activated to minimize power consumption.

To further minimize uncertainties introduced by the FOV matching procedure, we are currently working on the enhancement of the quadricopter attitude control through flight autonomy. Specifically, we plan to use global positioning system and machine learning to improve the vehicle's position-holding ability. This will allow the quadricopter to independently determine and continuously correct its position, thus reducing variations related to the remotely piloted system.

Chapter 8

Flow patterns characterization and identification

8.1 Introduction

In this Chapter, we present an innovative technique for unsupervised flow characterization based on nonlinear manifold learning. While this approach relies on video feed analysis, it provides a fundamentally different perspective on flow feature extraction. Indeed, previous efforts reported in this dissertation focus on the detection of a priori known objects in captured images through image manipulation, template-based correlation, and PIV. Such methodologies rely on the presence of surface tracers and aim at estimating surface velocity in selected locations of the analyzed field of view. Here, we propose an alternative approach, where the inherent structure of observed flows is captured through the global analysis of large image data sets. This methodology allows for the unsupervised classification of varying flow regimes and does not require the presence of visible tracing objects, thus paving the way to large scale remote flow analysis.

The characterization of complex flows and the identification of fluid structures are major challenges in climatology, biology, and engineering [178, 179]. The detection of salient flow features is traditionally addressed through the analysis of velocity fields, obtained from flow visualization, numerical, and analytical methodologies [180–183]. Specifically, flows are classified by estimating relevant physical parameters [184], through pattern tracking procedures [185, 186] or flow topology analysis [187–189]. These approaches rely on the availability of computationally expensive measurements to accurately describe the flow field. Beyond flow characterization, an even more elusive problem in fluid mechanics is the real time control of flow structures in biology, biomedicine, aerodynamics, and environmental science [190, 191]. Despite recent technological advances, such as the use of microelectromechanical systems and the introduction of feedback control, flow manipulation is still affected by limitations in measuring relevant flow parameters, data storage, and computational time [192]. Such drawbacks

hamper real time autonomous flow monitoring of complex systems.

In this chapter, we propose the implementation of a machine learning framework for unsupervised characterization of fluid flows. Different from established flow visualization techniques that require a-posteriori intensive processing of high resolution images [39, 40], our approach uses raw video data to rapidly disclose and examine relevant flow phenomena. Moving forward from pattern tracking, machine learning demonstrates remarkable potential in identifying features underlying complex phenomena [193, 194]. Specifically, manifold learning aims at uncovering the low dimensional structures "hidden" in high dimensional data. For instance, the isometric feature mapping (Isomap) embeds large scale data sets on lower dimensional manifolds approximated by undirected graphs, whose topology is utilized to compute geodesics on the true nonlinear manifolds [195]. This machine learning algorithm focuses on the extraction of relevant features directly from images without requiring the intermediate phase of quantitative parameters estimation [196]. In particular, the Isomap algorithm is effectively applied to the problem of face and human motion recognition [197] and collective behavior in biological systems [198]. These efforts support the feasibility of using Isomap in fluid dynamics.

To demonstrate our approach, we study the flow past a circular cylinder by processing flow visualization video data with Isomap for Reynolds numbers ranging from 50 to 1732. For such range, the fluid experiences steady separation, the formation of regular vortex patterns (that is, von Karman vortex streets), and the initiation of turbulence. We anticipate Isomap to detect flow regimes through varying dimensionality of the embedding manifolds, similarly to the problem of collective behavior of animal groups, where dimensionality is showed to relate with the degree of coordination between individuals [198]. The flow around a circular cylinder is widely studied in the literature [199–203] for its numerous instances in nature [204] and engineering [205]. In our study, this phenomenon is instrumental to experiment with an array of different flow regimes, spanning from steady to periodic and unsteady. We design an experimental setup including a hollow circular cylinder of outer diameter D positioned vertically at the cross-section of a water tunnel. A dye-injection system is developed for improved visualization of the flow streaklines around the cylinder through a digital camera (see the Methods for further details). We vary the flow regime by changing the free stream velocity, U.

In the framework of nonlinear machine learning, we regard experimental video frames as the Isomap ambient space and seek to characterize the flow by studying the embedding manifolds. We demonstrate that the topology of the embeddings can be associated with the flow regime, whereby lack of flow separation is manifested through one dimensional manifolds and the presence of coherent structures through higher dimensionality. Further, we show that manifold inspection can be used to estimate the frequency of vortex shedding and study flow pattern variations due to externally-induced perturbations. Once embedding manifolds are constructed from experimental conditions, they can be utilized to infer relevant flow properties of independent experiments without the need of performing computationally expensive kinematic or kinetic measurements. As an example, we use Isomap to analyze experimental videos obtained with a cylinder of unknown aspect ratio and infer the corresponding Reynolds number

from the learned manifolds.

8.2 Experimental setup and methodologies

Experiments are conducted in an open-test section water tunnel (Engineering Laboratory Design 502S). The tunnel cross-section is $15\,\mathrm{cm} \times 15\,\mathrm{cm}$. Along the water flume, a working cross-section is selected at approximately $50\,\mathrm{cm}$ in between two honeycomb grids for improved uniformity of the velocity profile. A hollow copper cylinder of outer diameter equal to $5\,\mathrm{mm}$ and aspect ratio of 0.042 is positioned vertically in the center of the working cross-section. Two $0.4\,\mathrm{mm}$ injection ports located at the mid-span of the cylinder at an angle of 90° from the front stagnation point allow for homogeneous and continuous rhodamine WT injection in the flow through a syringe system. Dye streaklines are captured by a Canon Vixia HG20 digital video camera, located $22\,\mathrm{cm}$ underneath the water tunnel and $10.4\,\mathrm{cm}$ downstream the working cross-section, with its axis perpendicular to the plane of vortex shedding. The camcorder acquires a field of view equal to $31.5\,\mathrm{cm} \times 18\,\mathrm{cm}$; its resolution is set to Full HD ($1920 \times 1080\,\mathrm{pixels}$); and its acquisition frequency is kept at $30\,\mathrm{Hz}$. Experiments are performed for Reynolds numbers equal to 50; 149; 159; 192; 246; 331; 389; 503; 546; 645; 816; 1041; 1178; 1292; 1461; 1598; and 1732. Different flow regimes are generated by varying the free stream velocity in the tunnel. This is achieved by adjusting the flume motor frequency from 1 to $14\,\mathrm{Hz}$, corresponding to an average flow velocity varying from approximately 0.010 to $0.346\,\mathrm{m/s}$ at the mid-span of the working cross-section as per an independent PIV analysis.

Flow detection is demonstrated through an independent experiment where a cylinder of diameter of $8.7\,\mathrm{mm}$ and aspect ratio of 0.0725 is used for generating video data. Two $0.4\,\mathrm{mm}$ injection ports are created at the cylinder mid-span (equivalent to the height of the smaller cylinder mid-span) for rhodamine deployment. Further, a Hero3 Black Edition GoPro video camera is installed $24\,\mathrm{cm}$ underneath the water tunnel to capture fluid motion. The camera focuses a field of view comparable to the one analyzed in the flow characterization experiments and its resolution and acquisition frequency are set to $1920 \times 1080\,\mathrm{pixels}$ and $30\,\mathrm{Hz}$, respectively.

The Isomap algorithm is a nonlinear manifold learning methodology for dimensionality reduction problems [194]. Differently from the classical multidimensional scaling method (MDS), Isomap uses geodesic rather than Euclidean manifold distances between data points [198]. The algorithm objectives are: i) embedding a data set of n d-dimensional data points on a manifold, ii) defining the manifold dimensionality, and iii) finding such dimension to be much less than d. In particular, for the data set $\mathcal{Z} = \{z_i\}_{i=1}^{n} \subset \mathbb{R}^d$, Isomap constructs a corresponding data set $\mathcal{Y} = \{y_i\}_{i=1}^{n} \subset \mathbb{R}^{\bar{d}}$ and assesses if $\bar{d} \ll d$. The $\bar{d}$-dimensional embedding is represented through the parametrization $\mu : \mathcal{Y} \to \mathcal{Z}$, where each j-th coordinate of the i-th data point is parameterized as $z_{ij} = \mu_j(y_{i1}, ..., y_{i\bar{d}})$, for $j = 1, ..., d$, and for each data point $i = 1, ..., n$. The second subscript is used to identify vector components. The algorithm follows these steps [195]:

1. *Construction of the neighbor graph $\mathcal{G} = \{\mathcal{V}, \mathcal{E}\}$ to approximate the manifold.* The elements of the set of vertices $\mathcal{V} = \{v_i\}_{i=1}^n$ match the data points $\mathcal{Z} = \{z_i\}_{i=1}^n$ and the elements of the set of edges $\mathcal{E}$ are unordered pairs of vertices in $\mathcal{G}$. Edges connect k-nearest neighbors vertices. Specifically, edges $\{v_i, v_j\}$ correspond to the k-closest data points z_j to z_i, for each $i = 1, ..., n$, with respect to the Euclidean distance in the ambient space (the pixels space), denoted by $d_{\mathcal{Z}}(z_i, z_j)$. The matrix $M_n \in \mathbb{R}^{n \times n}$, encoding the weighted graph of intrinsic manifold distances corresponding to $\mathcal{G}$, is computed. For each $\{v_i, v_j\} \in \mathcal{E}$, the distance equals the ij-th entry of M_n, that is, $M_n(i, j) = d_{\mathcal{Z}}(z_i, z_j)$. For all $\{v_i, v_j\} \notin \mathcal{E}$, $M_n(i, j)$ is set equal to ∞ to prevent jumps between branches of the underlying embedding.

2. *Computation of the graph geodesic matrix D_M to approximate the geodesic of the manifold.* Floyd's algorithm [206] is utilized to compute shortest paths. From M_n, an approximate geodesic distance matrix $D_M \in \mathbb{R}^{n \times n}$ is computed, whose ij-th entry is the shortest path length from v_i to v_j, being an approximation of manifold geodesic distances.

3. *Approximation of the manifold distance by k-nearest neighbor distance.* The matrix D_M computed in the previous step is used to approximate the geodesic distances of the manifold between z_i and z_j by the graph distance between v_i and v_j. If the data density is too low, a poor representation of the manifold could be obtained with some neighbors lying on separate manifold branches.

4. *Computation of the projective variables $\mathcal{Y}$ applying the classical MDS on the matrix D_M.* Classical MDS [207] is performed on a matrix of dissimilarities between pairs of input and candidate embeddings, which minimize the distance in the embedded manifold. For a survey on MDS, see [198].

The outputs of Isomap are the transformed data points on an embedding manifold for the input data set $\mathcal{Z}$ and the vector f of residual variances, which represents the fraction of data points not embedded on the manifold for different dimensions.

Experimental videos are decompressed into ".jpg" image files and sequences of 500 consecutive frames are selected for manifold learning. Such sequences are retained by performing a preliminary test where the homogeneity in image intensity is assayed and sets of images with marked differences in coloration discarded. This test is conducted to prevent the algorithm from relating data dimensionality to nonhomogeneities in dye injection. Before processing, images are cropped around the plane of vortex shedding to display a field of view of $11.5\,\mathrm{cm} \times 4.3\,\mathrm{cm}$ corresponding to $700 \times 260\,\mathrm{pixels}$. Only the red channel (where pixel intensity varies from 0 to 255) is extracted for Isomap processing. For each flow regime, Isomap is applied to data sets comprising $n = 500$ arrays of $d = 182000$ dimensional data points, where each array corresponds to a reshaped raw image. The nearest neighbors parameter is set to $k = 20$ based on similarity among consecutive images. To test the stability of the methodology, the Isomap algorithm is rerun on subsets of subsampled images and varying the value of k. We find that

embedding manifold topologies are consistently recovered for values of k ranging from 15 to 25 for the same data set. The vectors of the residual variances for the first three embedding dimensionalities are plotted against the respective Re for each experimental video. Such data points are fitted through the nonlinear least squares method with functions of the type $\alpha Re \exp(-\beta Re)$, where α and β are fitting parameters. The 95% confidence intervals are estimated based on the fitting model coefficient covariance matrix.

Vortex shedding frequency is evaluated for experiments conducted at $Re = 149$; 159; 192; 246; 331; and 389. For such data sets, the frequency obtained from images located at comparable angular positions on the annular embedding projection is compared to vortex shedding frequencies estimated through the analysis of randomly selected sets of 10 to 40 consecutive images of the same videos. Similar to [208], frequencies are found by counting the number of vortices convected past a selected reference point in consecutive pictures in known time intervals. The duration of the time intervals is computed from the camera acquisition frequency.

8.3 Results

8.3.1 Flow regimes and embedding dimensionality

We process experimental video data recorded with a commercial camcorder with the Isomap algorithm and study the relationship between the topological features of the embedding manifolds and the flow regime, controlled by the Reynolds number Re (see the Materials and Methods for the full set of Re adopted in the experiments). The Reynolds number is defined as $Re = UD/\nu$, where ν is the kinematic viscosity of water (set to $1 \times 10^{-6}\,\mathrm{m}^2/\mathrm{s}$ in this study). In line with our expectations, we find that data relative to steady flow separation, that is, $Re = 50$, are embedded onto one dimensional manifolds, see Figure 8.1(a). Conversely, for $Re = 149$ up to 546, that is, for flow regimes characterized by a transition from laminar to turbulent von Karman vortex streets [199], cylindrical manifolds are obtained, see Figure 8.1(b). From $Re = 645$, when turbulent flow coexists with periodic fluctuations in the cylinder wake [209], larger amounts of data points are not embedded onto cylindrical surfaces and rather fall onto irregularly shaped manifolds that are well approximated by nearly one dimensional structures, see Figure 8.1(c).

8.3.2 Global coordinates for von Karman vortex streets

Figures 8.2(a-c) display the cylindrical manifold, residual variance, and distance matrix obtained by setting $Re = 192$. We find that data points are arranged onto a thick cylindrical structure; specifically, 90% of the data set is represented by a three dimensional manifold (see the residual variance for dimensionality equal to three). Further, the distance matrix highlights the periodicity of the flow through the presence of regular sets of points that are closer to their neighbors (see the diagonal stripes

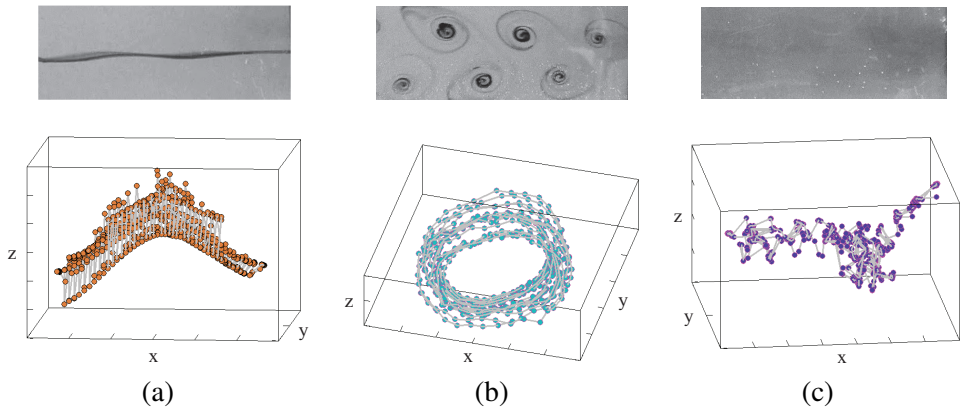

(a) (b) (c)

Figure 8.1: (a) Enhanced contrast pictures and three dimensional embedding manifolds for experimental data sets at $Re = 50$, (b) $Re = 159$, and (c) $Re = 1732$.

in Figure 8.2(c)).

We further show that the topology of the embedding is related to two major features underlying the experimental data set. Specifically, in the two dimensional projection in Figure 8.2(d), all data points are symmetrically distributed along an annulus, suggesting a periodic behavior. By counterclockwise inspection of the annulus, we observe that data are consecutively ordered along the flow direction. Moreover, data points located at similar angular positions tend to depict comparable shapes. Variations along the thickness of the cylinder, corresponding to its radial coordinate, are related to varying image contrast during the experiment. Diametrically opposed locations on the annulus show vortex shedding phases that differ by $180°$. Thus, one of the Isomap global coordinates, corresponding to the angular coordinate along the cylinder mantle, identifies the periodicity of the observed flow. Projecting the three dimensional embedding on a plane parallel to its axis, we find that images are horizontally ordered in the direction of flow, Figure 8.2(e). Further, variations of the flow pattern in the data set are arranged along the vertical direction, corresponding to the axial coordinate of the cylinder, with images displaying differently shaped vortices arranged far apart on the manifold.

8.3.3 Flow parameter estimation from manifold topology

We quantify the vortex shedding frequency by inspection of the annular projections recovered for $Re = 149$ to 389 (for Re higher than 389, vortices are hardly distinguishable). Specifically, we manually compute from the video feed the number of vortices, $n_{\mathrm{v}}^{\mathrm{I}}$, formed between images laying at comparable angular positions on the annulus, see Figure 3(a) for the randomly selected sector between $210°$ and $240°$. Further, we compare our results to estimations obtained by counting in the video feed the number of vortices shed in known time intervals. For the sector of the cylinder in Figure 8.3(a), computed values, $n_{\mathrm{v}}^{\mathrm{I}}$, are consistent with findings from vortex counting, $n_{\mathrm{v}}^{\mathrm{VI}}$, see Figure 8.3(b) (root mean squared error, RMSE, equal to 0.45 with respect to the bisectrix).

8.3.4 Flow characterization and identification

Our analysis of the dimensionality of Isomap embeddings demonstrates a close correspondence between the algorithm outputs and the flow physics. We further elucidate such relations by studying the residual variances for the first three dimensionalities of the data sets, which capture the vast majority of the experiments (more than 75% of the data). In Figure 8.4(a), we present residual variances for all the experimental data sets fitted by functions of the form $\alpha Re \exp(-\beta Re)$, with α and β being unknown parameters ($\mathrm{RMSE}_{f_1} = 0.12$, $\mathrm{RMSE}_{f_2} = 0.13$, and $\mathrm{RMSE}_{f_3} = 0.10$), where shaded regions denote the 95% confidence intervals. As expected, we find that at low and high Re, the flow can be described with nearly one dimensional embeddings, which capture the translational motion in the video feed. On the other hand, as coherent structures are shed by the cylinder, data points are fit on higher dimensionality manifolds, which also account for the shape of the vortices. We observe that increasing the degree of turbulence of the flow corresponds to "hiding" periodic fluctuations in the flow. Indeed, Isomap captures the prevalently translational nature of the data.

The relations illustrated in Figure 8.4(a) are independent of the specific experimental conditions they are learned from. Indeed, they can be used as ground truth data for the identification of the flow regime of data sets acquired at unknown settings. As a proof-of-concept, we study the flow past a circular cylinder of unknown diameter, where the only provided information is the free stream velocity. Experimental frames are processed through the Isomap algorithm and recovered residual variances for the first three dimensionalities are used to estimate the Reynolds number (see the Methods for further details). Specifically, the total squared error between learned and experimental residual variances is minimized to obtain the flow degree of turbulence. We predict that Re of the independent experiment is within 182 and 359 with 95% confidence interval, see Figure 8.4(b). The actual Re of the flow lays in the range of values detected by the procedure. Interestingly, the three dimensional representation of the embedding manifold is a cylinder with features comparable to previously illustrated structures.

Our results show that the dimensionality of the embedding manifold and its topology are landmarks of the flow regime, whereby smooth one dimensional manifolds are constructed from steady flows, cylindrical embeddings from von Karman vortex streets, and irregular structures from turbulent flows. With respect to von Karman vortex streets, our results are in agreement with the analysis presented in [188], where proper orthogonal decomposition is conducted on particle image velocimetry (PIV) and analytical velocity fields for flow characterization. In fact, we obtain striped distance matrices and two dimensional annular embedding projections for vortex shedding similar to [188]. This is achieved by directly processing video images through Isomap rather than performing computationally expensive PIV. Notably, we recover such annular projection also when the Isomap input space is constituted of unordered sets of experimental video frames, suggesting that our procedure can be successfully used to independently sort the ambient space in time.

In line with our expectations, we also find that Isomap global coordinates of the embedding manifolds relate with relevant features of the flow. For example, the axial coordinate of the cylinder in

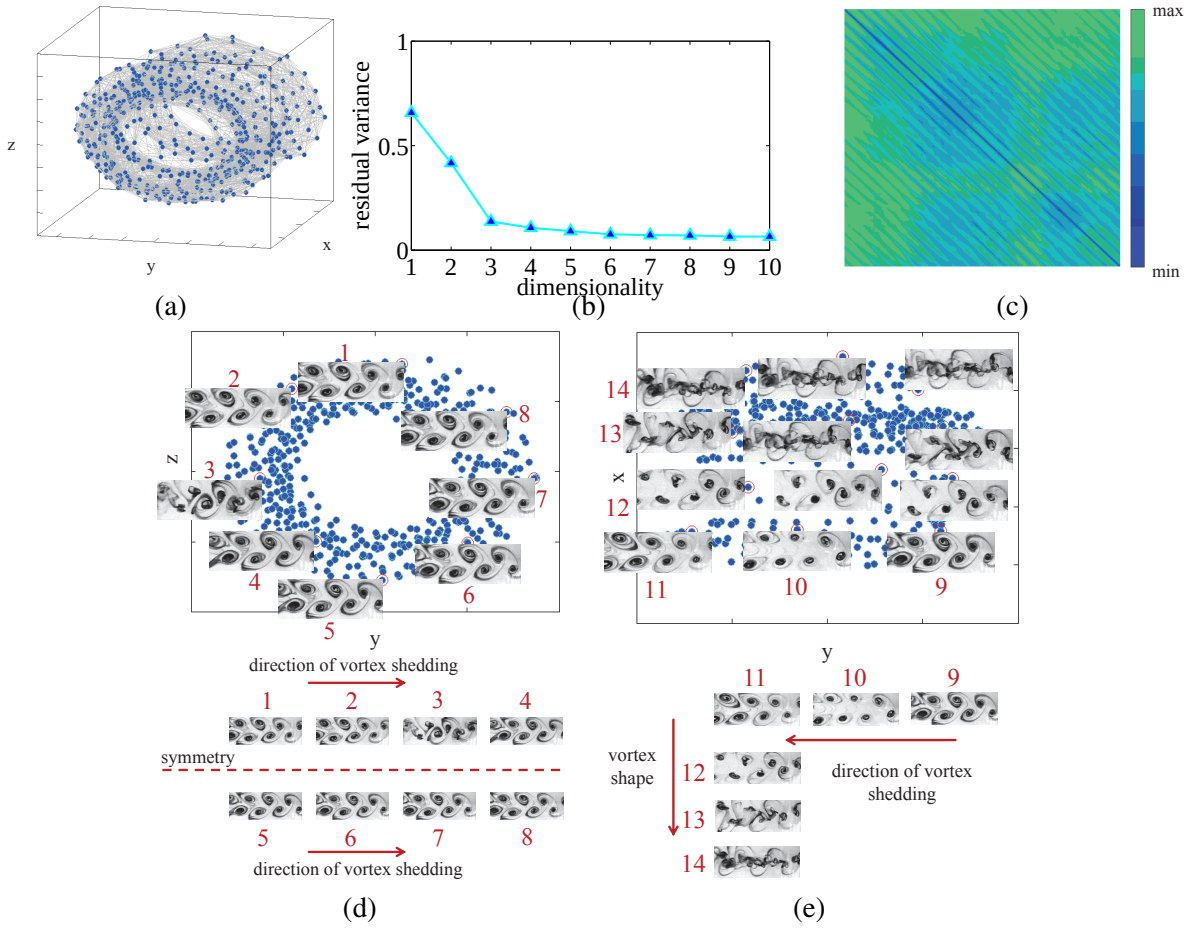

Figure 8.2: (a) Three dimensional representation of the embedding manifold for data set collected at $Re = 192$. (Data points, blue circles, are arranged on a thick cylinder). (b) Residual variance of the data set against dimensionality; values are reported up to dimensionality equal to 10. (c) Distance matrix for the data set as computed by Isomap (each point represents a frame); blue stripes indicate topologically close sets of images. (d) Two dimensional projection on the yz-plane of (a); images 1 to 8 correspond to selected data points on the annulus (inspecting the manifold in the counterclockwise direction, the direction of vortex shedding is recovered, thus revealing the coherent structures' translation. Axes of symmetry coincide with the diameters of the annulus). (e) Two dimensional projection on the xy-plane of (a); images 9 to 14 correspond to selected data points on the embedding (the axial coordinate of the cylinder is related to flow pattern configuration and, therefore, to the occurrence of shear layer separation. Images along the y axis are ordered in the direction of flow. Contrast and brightness in video frames are enhanced for readability).

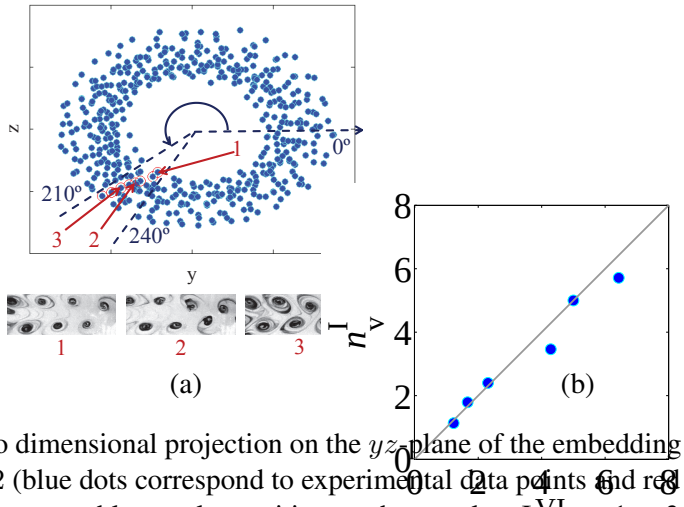

Figure 8.3: (a) Two dimensional projection on the yz plane of the embedding manifold for data set collected at $Re = 192$ (blue dots correspond to experimental data points and red circled markers are video frames laying at a comparable angular position on the annulus. Images 1 to 3 are selected video frames used for vortex shedding frequency estimation. All of them depict similar vortex patterns. Shedding frequency is computed by dividing the number of coherent structures shed from image 1 to 2 (and 2 to 3) by the respective time interval. Contrast and brightness in video frames are enhanced for readability). (b) Comparison of vortex shedding frequency obtained from the procedure illustrated in (a), $n_{\mathrm{v}}^{\mathrm{I}}$, to values computed from vortex counting, $n_{\mathrm{v}}^{\mathrm{VI}}$ (the solid line is the bisectrix).

Figure 2(e) captures variations in vortex shape and provides a measure of the wake regularity. These variations in the geometry of the shed vortices are well studied in fluid dynamics [210] and can be related to flow-induced vibrations of the cylinder, boundary-layer effects, and inhomogeneities in the free stream velocity field. We comment that higher accuracy should be attained by improving free stream velocity estimation, enhancing the dye injection system, and reducing boundary effects from the water tunnel side walls.

Raw video feed is also considered in [211] to study flow kinematics. Therein, images are obtained from a PIV study and the optical flow technique is utilized to reconstruct the velocity field. Here, we rely on standard video feed for rapid unsupervised characterization of flow phenomena through global features. While the accuracy of optical flow techniques is highly dependent on image quality and tracer seeding uniformity in the field of view, Isomap emphasizes underlying flow characteristics through relative topological distance among video data points, thus reducing the effect of fixed pattern noise in the images.

8.4 Discussion

In contrast to canonical vortex detection methodologies, no preprocessing in terms of scaling, compression, or filtering is performed on images before nonlinear embedding through Isomap. Nonetheless, the performance of the procedure relies on the visibility of the flow structures and, therefore, low contrast,

poor resolution, and highly nonuniform background noise may require image enhancement before feature extraction. In this context, we emphasize the relevance of experimenting with high sample sizes to guarantee the correct estimation of Isomap geodesic distances (see the Methods for details). Finally, we comment that learned relations between Isomap residual variances and Re are related to user-defined parameters, such as the temporal resolution and the field of view of acquired video frames. For instance, experimenting with a higher frame acquisition frequency would result in longer tails in curves in Figure 4. Indeed, sampling frequency would be closer to the flow vortex shedding frequency and periodic flow fluctuations would be more defined in the images. Similar findings are expected if larger fields of view were considered. In case of different vortical structures and shapes, we predict variations in the dimensionality of the embedding manifolds, whereas we foresee similar decays for the residual variances with respect to Re.

Our results indicate that unsupervised nonlinear machine learning through the Isomap algorithm can be successfully used to rapidly unravel salient flow features. Real time flow monitoring is a major challenge when image-based methodologies are needed rather than invasive sensors and probes. For instance, we expect this methodology to find application in biofluidics, where flow characterization can aid in monitoring hemodynamics, oxygen transport, intravascular blood pressure, and blood vessel obstructions [212, 213]. Further, unsupervised flow characterization is anticipated to provide insight in environmental sensing, where noninvasive methodologies are increasingly needed for monitoring the evolution of large scale natural systems [72, 204, 214]. In addition, the approach may find application in autonomous robotics for rapid environmental mapping of unknown areas [215].

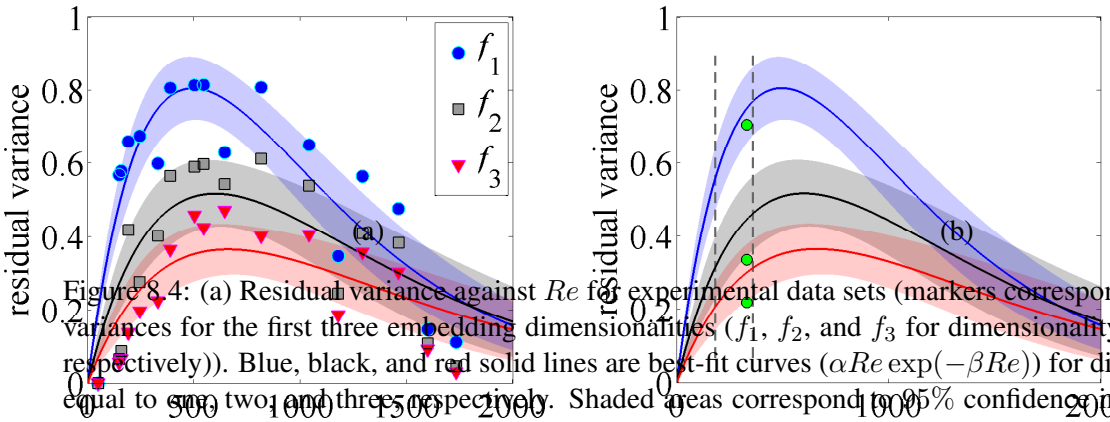

Figure 8.4: (a) Residual variance against Re for experimental data sets (markers correspond to residual variances for the first three embedding dimensionalities (f_1, f_2, and f_3 for dimensionality 1, 2, and 3, respectively)). Blue, black, and red solid lines are best-fit curves ($\alpha Re \exp(-\beta Re)$) for dimensionality equal to one, two, and three, respectively. Shaded areas correspond to 95% confidence intervals). (b) Residual variances of the independent experiment superimposed to learned relations from (a) (green circles depict residual variances at the actual experimental Re, that is, 331. Gray dashed lines display the range of possible Re detectable through the methodology).

Chapter 9

Contributions and Future Work

This work directly addresses the essential need for novel observations of the hydrological community by developing an unprecedented flow characterization methodology that relies on the mutual integration of traditional tracing techniques and state-of-the-art image-based sensing procedures. Notably, this effort results from a multidisciplinary approach to the problem of environmental monitoring at the interface of experimental hydrology and sensing systems. Specifically, in Chapter 2, we quantitatively characterize the visibility of insoluble and buoyant fluorescent particles through digital camera acquisition to assess the feasibility of using fluorescent beads as hydrological tracers. Further, we develop a procedure to detect the presence of the fluorescent particles in digital images and rapidly infer the transit of particles in videos. In Chapter 3, we develop a template-based particle tracking procedure to identify the bead trajectory and velocity in complex settings. Namely, the image analysis procedure is effective at detecting and tracking particles in case of high flow regimes, water reflections, and background noise, and leads to velocity estimations comparable to measurements obtained from PIV.

The efficiency of the detection and tracking algorithms are further demonstrated in Chapter 4 and 5, where flow velocities and travel times are estimated in proof-of-concept experiments in stream and overland flow conditions. In addition to providing an assessment of the methodology in natural settings, these studies also identify practical advantages and limitations to the proposed methodology and indicate particle characteristics and setup configurations that allow for optimal flow analyses.

In Chapter 6, we address the problem of the environmental impact of the methodology on natural ecosystems by providing an inexpensive fabrication procedure of eco-friendly fluorescent particles and a thorough characterization of the properties of the tracer. The particles are designed to be easily detectable through digital cameras and to accurately trace flows. Experimental feasibility analyses demonstrate that the particles can be detected under sunlight conditions with the developed image analysis procedures.

In Chapter 7, we focus on the implementation of the proposed sensing system combined with LSPIV algorithms in large scale riverine environments. Specifically, we identify critical sources of uncertainties in the kinematic characterization of large scale flows and propose an alternative experimental configura-

tion for data acquisition. Further, we propose guidelines and recommendations for the implementation of LSPIV. As an additional step toward the miniaturization of a stand-alone sensing station for remote flow characterization, we also design and develop an aerial platform for nonintrusive LSPIV. Based on feasibility experimental assessments, we demonstrate that values estimated from the aerial unit are comparable to traditional LSPIV implementations.

We address noninvasive flow characterization from a dimensionality reduction perspective in Chapter 8, where flows at varying regimes are studied by exploring their topological dimensionality. We find that flow features are intrinsically captured in the structure of manifold embeddings and that manifold topology can be used to estimate important flow parameters such as vortex shedding frequency. Further, we utilize this machine learning approach to detect the regime of a priori unknown flows, thus leveraging unsupervised flow in remote conditions.

The work in this dissertation contributes to the literature in experimental sensing in several aspects. Major contributions of the proposed flow characterization technique can be synthesized as follows:

- the methodology is based on the use of eco-compatible yet reliable tracers, which are capable of accurately moving with fluid flows and are not harmful for the environment;
- the particle tracers are uniquely detectable from the surrounding environment, thus leveraging the use of noninvasive sensing techniques based on image caption;
- image-based flow characterization and detection procedures provide rapid and efficient characterization of the kinematics of water bodies.

Notably, the proposed methodology is versatile in its nature and can be used to address a diverse class of hydrological aspects by fine-tuning relevant parameters, such as particle diameter and buoyancy and image acquisition rate.

A major contribution of the proposed particle synthesis procedure rests on the encapsulation of fluorescent nanoparticles in the most external layer of the spheres. This results in a progressive decay and shift of the fluorescence emission spectrum upon exposure to weathering agents. Besides providing a unique aging index for the particles, this phenomenon also guarantees the complete inactivation of the fluorescence in time. Further, the use of the beeswax matrix allows for enhanced compatibility of the beads with the surrounding environment, while the visibility of the fluorescence with respect to the background limits the amount of tracing material to be deployed for environmental investigations.

Within the proposed fabrication methodology, additional research should be directed toward the functionalization of the beeswax matrix with alternative fluorophores and organic dyes. It is expected that a systematic study of the emission signature of a variety of dyes and fluorophores upon exposure to UV light radiations will considerably aid in the formulation of highly visible tracers. In addition, further efforts should be devoted to the investigation of the fluorescence aging phenomenon and to the potential for fluorescent-decaying tracers to be used in catchment-scale hydrological studies.

Different from optical methods traditionally used for hydrological applications, in this work, we comprehensively explore the use of digital cameras for environmental monitoring in a variety of settings, spanning from controlled dark laboratory conditions to direct sunlight illumination. This previously untapped two-fold approach aims at anticipating and mitigating adverse settings typical of natural environments, thus informing the implementation of the technology for hydrological applications.

While digital acquisition systems are typically regarded as a technological tool for data acquisition, in this endeavor, we pave the way to a novel conception of video capturing. Specifically, we foresee the development of smart video acquisition systems where real-time image-based analysis feedback is employed by the camera interface to adjust acquisition parameters and improve data quality. In this framework, the integration and coordination of cameras with light and temperature sensors is expected to open novel avenues to continuous environmental monitoring in dynamic ecosystems.

In the field of image analysis for environmental monitoring, this work is the first to address the issue of dealing with non-ideal image acquisition conditions, where inhomogeneous backgrounds, rapidly-deforming water reflections, and heavy turbidity prevent the implementation of standard particle tracking algorithms. To address ambient adversities, this work proposes the use of a variety of ad hoc developed procedures, including template-based correlation algorithm, LSPIV, and dimensionality reduction through nonlinear manifold learning. Compared to more established measurement techniques, we demonstrate these methodologies to be effective for detecting flow regime and noninvasively characterizing surface flow velocity.

As a further step toward the real-time characterization of surface flows, additional efforts should be devoted to the use of computer vision tracking procedures, such as Gaussian mixture models and optical flow. Such methodologies are expected to aid rapid flow characterization by decreasing computational time. Information from such preliminary characterizations could also be used to inform the coordination of multiple sensors for continuous data acquisition.

In the realm of hydrological processes, the proposed observational methodology is applied to the study of surface water phenomena. In particular, we conduct nonintrusive field studies to estimate local flow velocities and stream reach travel times for a mountainous stream, where high flow regimes and abundant water reflections prevent the implementation of traditional flow sensing systems. In addition, we provide a kinematic characterization of the flow observed in natural hillslope rills, where the massive presence of sediments and shallow water depths limit flow measurements.

Based on results from these efforts, future research directions may entail the extension of the proposed sensing system to the characterization of large scale stream flow and overland flow systems in natural environments. In particular, the use of aerial vehicles for surface flow monitoring could be explored on large scale river ecosystems and catchment drainage networks. By integrating cutting-edge sensing systems and hydrological methods, we expect future research to be devoted to the development of dynamic networks of mobile measurement stations distributed over the territory for environmental monitoring.

Bibliography

[1] E. J. Watson. The radial spread of a liquid jet over a horizontal plane. *Journal of Fluid Mechanics*, 20:481–499, 1964.

[2] V. T. Chow, D. R. Maidment, and L. W. Mays. *Applied Hydrology*. McGraw-Hill, New York, 1988.

[3] R. L. Bras. *Hydrology: An Introduction to Hydrologic Science*. Addison-Wesley, Lebanon, Indiana, 1989.

[4] M. K. Bansal. Dispersion in natural streams. *ASCE Journal of Hydraulics Division*, 97(11):1867–1886, 1971.

[5] M. Piccarreta, H. Faulkner, M. Bentivenga, and D. Capolongo. The influence of physico-chemical material properties on erosion processes in the badlands of Basilicata, Southern Italy. *Geomorphology*, 81(3-4):235–251, 2006.

[6] J. Wainwright. Infiltration, runoff and erosion characteristics of agricultural land in extreme storm events, SE France. *Catena*, 26(1-2):27–47, 1996.

[7] M. G. Kondolf and H. Piégay, editors. *Tools in Fluvial Geomorphology*. John Wiley & Sons, West Sussex, UK, 2003.

[8] M. C. Rulli and R. Rosso. Modeling catchment erosion after wildfires in the San Gabriel Mountains of Southern California. *Geophysical Research Letters*, 32(19):L19401, 2005.

[9] G. B. Chirico, H. Medina, and N. Romano. Uncertainty in predicting soil hydraulic properties at the hillslope scale with indirect methods. *Journal of Hydrology*, 334(3-4):405–422, 2007.

[10] N. M. Gasparini, G. E. Tucker, and R. L. Bras. Network-scale dynamics of grain-size sorting: Implications for downstream fining, stream-profile concavity, and drainage basin morphology. *Earth Surface Processes and Landforms*, 29(4):401–421, 2004.

[11] E. Istanbulluoglu, O. Yetemen, E. R. Vivoni, H. A. Gutierrez-Jurado, and R. L. Bras. Eco-geomorphic implications of hillslope aspect: Inferences from analysis of landscape morphology in central New Mexico. *Geophysical Research Letters*, 35(14):L14403, 2008.

[12] G. E. Tucker and R. L. Bras. Hillslope processes, drainage density, and landscape morphology. *Water Resources Research*, 34(10):2751–2764, 1998.

[13] C. Leibundgut, P. Maloszewski, and C. Külls. *Tracers in Hydrology*. Wiley-Blackwell, Oxford, UK, 2009.

[14] M. Jodeau, A. Hauet, A. Paquier, J. Le Coz, and G. Dramais. Application and evaluation of LS-PIV technique for the monitoring of river surface velocities in high flow conditions. *Flow Measurement and Instrumentation*, 19(2):117–127, 2008.

[15] Y. Kim, M. V. I. Muste, A. Hauet, W. F. Krajewski, A. Kruger, and A. A. Bradley. Stream discharge using mobile large-scale particle image velocimetry: A proof of concept. *Water Resources Research*, 44(9):1–6, 2008.

[16] L. D. Dunkerley. An optical tachometer for short-path measurement of flow speeds in shallow overland flows: improved alternative to dye timing. *Earth Surface Processes and Landforms*, 28(7):777–786, 2003.

[17] M. A. Hassan and P. Ergenzinger. *Tools in Fluvial Geomorphology*, chapter Use of Tracers in Fluvial Geomorphology, pages 397–423. John Wiley & Sons, West Sussex, England, 2003.

[18] O. Planchon, N. Silvera, R. Gimenez, D. Favis-Mortlock, J. Wainwright, Y. Le Bissonnais, and G. Govers. An automated salt-tracing gauge for flow-velocity measurement. *Earth Surface Processes and Landforms*, 30(7):833–844, 2005.

[19] J. A. Replogle, L. E. Myers, and K. J. Brust. Flow measurements with fluorescent tracers. *Journal of Hydraulic Division*, 92:1–15, 1966.

[20] M. G. Waldon. Estimation of average stream velocity. *Journal of Hydraulic Engineering*, 130(11):1119–1122, 2004.

[21] J. Holecek and J. Vocel. Measurement of time of travel in the Volynka experimental basin. In *Representative and Experimental Areas. Symposium of Budapest*. IAHS, 1965.

[22] J. F. Wilson, Jr. Time-of-travel measurements and other applications of dye tracing. *International Association of Hydrological Sciences*, 76:252–262, 1967.

[23] G. Botter, E. Milan, E. Bertuzzo, S. Zanardo, M. Marani, and A. Rinaldo. Inferences from catchment-scale tracer circulation experiments. *Journal of Hydrology*, 369(3-4):368–380, 2009.

[24] S. W. Lyon, S. L. E. Desilets, and P. A. Troch. Characterizing the response of a catchment to an extreme rainfall event using hydrometric and isotopic data. *Water Resources Research*, 44(6):1–12, 2008.

[25] D. H. Pilgrim. Travel times and nonlinearity of flood runoff from tracer measurements on a small watershed. *Water Resources Research*, 12(3):487–496, 1975.

[26] S. Grimaldi, A. Petroselli, G. Alonso, and F. Nardi. Flow time estimation with variable hillslope velocity in ungauged basins. *Advances in Water Resources*, 33(10):1216–1223, 2010.

[27] E. F. Hubbard. *Measurement of time of travel and dispersion in streams by dye tracing*. U.S. Government Printing Office, Washington D.C., 1982.

[28] A. N. Papanicolaou, J. F. Fox, and J. Marshall. Soil fingerprinting in the Palouse Basin, USA using stable carbon and nitrogen isotopes. *International Journal of Sediment Research*, 18(2):278–284, 2003.

[29] X.-F. Wen, S.-C. Zhang, X.-M. Sun, G.-R. Yu, and X. Lee. Water vapor and precipitation isotope ratios in Beijing, China. *Journal of Geophysical Research*, 115(D1):D01103, 2010.

[30] D. H. Pilgrim. Radioactive tracing of storm runoff on a small catchment: I. Experimental technique. *Journal of Hydrology*, 4:289–305, 1966.

[31] D. Calkins and T. Dunne. A salt tracing method for measuring channel velocities in small mountain streams. *Journal of Hydrology*, 11(4):379–392, 1970.

[32] K. K. Turekian, N. Tanaka, V. C. Turekian, T. Torgersen, and E. C. Deangelo. Transfer rates of dissolved tracers through estuaries based on ^{228}Ra: a study of Long Island Sound. *Continental Shelf Research*, 16(7):863–873, 1996.

[33] J. Wienhöfer, K. Germer, F. Lindenmaier, A. Färber, and E. Zehe. Applied tracers for the observation of subsurface stormflow at the hillslope scale. *Hydrology and Earth System Sciences*, 13(7):1145–1161, 2009.

[34] T. Torgersen and B. M. Kennedy. Air-Xe enrichments in Elk Hills oil field gases: role of water in migration and storage. *Earth and Planetary Science Letters*, 167(3-4):239–253, 1999.

[35] D. Johnson and C. Pattiaratchi. Application, modelling, and validation of surfzone drifters. *Coastal Engineering*, 51(5-6):455–471, 2004.

[36] W. E. Schmidt, K. T. Holland, and R. T. Guza. Surfzone drifters: applications and observations. In *Proceedings of the IEEE/OES Eighth Working Conference on Current Measurement Technology*, pages 106–110, 2005.

[37] R. J. Stockdale, S. J. McLelland, R. Middleton, and T. J. Coulthard. Measuring river velocities using GPS river flow tracers (GRiFTers). *Earth Surface Processes and Landforms*, 33(8):1315–1322, 2008.

[38] R. J. Adrian. Twenty years of particle image velocimetry. *Experiments in Fluids*, 39(2):159–169, 2005.

[39] R. J. Adrian. Particle-imaging techniques for experimental fluid-mechanics. *Annual Review of Fluid Mechanics*, 23:261–304, 1991.

[40] M. Raffel, C. E. Willert, S. T. Wereley, and J. Kompenhans. *Particle Image Velocimetry. A practical guide.* Springer, New York, 2007.

[41] J. D. Creutin, M. Muste, A. A. Bradley, S. C. Kim, and A. Kruger. River gauging using PIV techniques: a proof of concept experiment on the Iowa River. *Journal of Hydrology*, 277(3-4):182–194, 2003.

[42] A. Melling. Tracer particles and seeding for particle image velocimetry. *Measurement Science and Technology*, 8(12):1406–1416, 1997.

[43] V. Weitbrecht, G. Kühn, and G. H. Jirka. Large scale PIV-measurements at the surface of shallow water flows. *Flow Measurement and Instrumentation*, 13(5-6):237–245, 2002.

[44] E. A. Meselhe, T. Peeva, and M. V. I. Muste. Large scale particle image velocimetry for low velocity and shallow water flows. *Journal of Hydraulic Engineering*, 130(9):937–940, 2004.

[45] H. W. Tang, C. Chen, H. Chen, and J. T. Huang. An improved PTV system for large-scale physical river model. *Journal of Hydrodynamics, Ser. B*, 20(6):669–678, 2008.

[46] A. A. Bradley, A. Kruger, E. A. Meselhe, and M. V. I. Muste. Flow measurement in streams using video imagery. *Water Resources Research*, 38(12):1–8, 2002.

[47] D. Angarita-Jaimes, M. Ormsby, M. Chennaoui, N. Angarita-Jaimes, C. Towers, A. Jones, and D. Towers. Optically efficient fluorescent tracers for multi-constituent PIV. *Experiments in Fluids*, 45(4):623–631, 2008.

[48] S. Jin, P. Huang, J. Park, J. Y. Yoo, and K. S. Breuer. Near-surface velocimetry using evanescent wave illumination. *Experiments in Fluids*, 37(6):825–833, 2004.

[49] F. Pedocchi, J. Martin, and M. H. García. Inexpensive fluorescent particles for large-scale experiments using particle image velocimetry. *Experiments in Fluids*, 45(1):183–186, 2008.

[50] J. Martin and M. García. Combined PIV/PLIF measurements of a steady density current front. *Experiments in Fluids*, 46(2):265–276, 2009.

[51] Y. J. Weitsman and M. Elahi. Effects of fluids on the deformation, strength and durability of polymeric composites – An overview. *Mechanics of Time-Dependent Materials*, 4(2):107–126, 2000.

[52] K. J. Beven and M. J. Kirkby. A physically based, variable contributing area model of basin hydrology. *Hydrological Sciences Bulletin*, 24(1):43–69, 1979.

[53] K. Beven and J. Freer. A dynamic TOPMODEL. *Hydrological Processes*, 15(10):1993–2011, 2001.

[54] A. Rinaldo, K. J. Beven, E. Bertuzzo, L. Nicotina, J. Davies, A. Fiori, and D. Russo. Catchment travel time distributions and water flow in soils. *Water Resources Research*, 47(7):W07537, 2011.

[55] A. Bronstert and E. J. Plate. Modelling of runoff generation and soil moisture dynamics for hillslopes and micro-catchments. *Journal of Hydrology*, 198(1–4):177–195, 1997.

[56] S. Scherrer, F. Naef, A. O. Faeh, and I. Cordery. Formation of runoff at the hillslope scale during intense precipitation. *Hydrology and Earth System Sciences*, 11(2):907–922, 2007.

[57] M. P. Clark, D. E. Rupp, R. A. Woods, H.J. Tromp-van Meerveld, N. E. Peters, and J. E. Freer. Consistency between hydrological models and field observations: linking processes at the hillslope scale to hydrological responses at the watershed scale. *Hydrological Processes*, 23(2):311–319, 2009.

[58] D. Dunkerley. Estimating the mean speed of laminar overland flow using dye injection-uncertainty on rough surfaces. *Earth Surface Processes and Landforms*, 26(4):363–374, 2001.

[59] K. J. McGuire, M. Weiler, and J. J. McDonnell. Integrating tracer experiments with modeling to assess runoff processes and water transit times. *Advances in Water Resources*, 30(4):824–837, 2007.

[60] J. J. McDonnell, K. McGuire, P. Aggarwal, K. J. Beven, D. Biondi, G. Destouni, S. Dunn, A. James, J. Kirchner, P. Kraft, S. Lyon, P. Maloszewski, B. Newman, L. Pfister, A. Rinaldo, A. Rodhe, T. Sayama, J. Seibert, K. Solomon, C. Soulsby, M. Stewart, D. Tetzlaff, C. Tobin, P. Trotch, M. Weiler, A. Western, A. Wörman, and S. Wrede. How old is streamwater? Open questions in catchment transit time conceptualization, modelling and analysis. *Hydrological Processes*, 24(12):1745–1754, 2010.

[61] J.E. Costa, K.R. Spicer, R.T. Cheng, F.P. Haeni, N.B. Melcher, E.M. Thurman, W.J. Plant, and W.C. Keller. Measuring stream discharge by non-contact methods – a proof-of-concept experiment. *Geophysical Research Letters*, 27(4):553–556, 2000.

[62] M. C. Lee, C. J. Lai, J. M. Leu, W. J. Plant, W. C. Keller, and K. Hayes. Non-contact flood discharge measurements using an X-band pulse radar (I) Theory. *Flow Measurement and Instrumentation*, 13(5-6):265–270, 2002.

[63] N. B. Melcher, J. E. Costa, F. P. Haeni, R. T. Cheng, E. M. Thurman, M. Buursink, K. R. Spicer, E. Hayes, W. J. Plant, W. C. Keller, and K. Hayes. River discharge measurements by using helicopter-mounted radar. *Geophysical Research Letters*, 29(22):2084, 2002.

[64] J. D. Osorio-Cano, A. F. Osorio, and R. Medina. A method for extracting surface flow velocities and discharge volumes from video images in laboratory. *Flow Measurement and Instrumentation*, 33:188–196, 2013.

[65] W. J. Plant, W. C. Keller, and K. Hayes. Measurement of river surface currents with coherent microwave systems. *IEEE Transactions on Geoscience and Remote Sensing*, 43(6):1242–1257, 2005.

[66] J. A. Puleo, T. E. McKenna, K. T. Holland, and J. Calantoni. Quantifying riverine surface currents from time sequences of thermal infrared imagery. *Water Resources Research*, 48(1):W01527, 2012.

[67] C. Mügler, O. Planchon, J. Patin, S. Weill, N. Silvera, P. Richard, and E. Mouche. Comparison of roughness models to simulate overland flow and tracer transport experiments under simulated rainfall at plot scale. *Journal of Hydrology*, 402(1–2):25–40, 2011.

[68] G. Dramais, J. LeCoz, B. Camenen, and A. Hauet. Advantages of a mobile LSPIV method for measuring flood discharges and improving stage-discharge curves. *Journal of Hydro-environment Research*, 5(4):301–312, 2011.

[69] M. Bakalowicz. Karst groundwater: a challenge for new resources. *Hydrogeology Journal*, 13(1):148–160, 2005.

[70] F. Tauro, M. Aureli, M. Porfiri, and S. Grimaldi. Characterization of buoyant fluorescent particles for field observations of water flows. *Sensors*, 10(12):11512–11529, 2010.

[71] F. Tauro, C. Pagano, M. Porfiri, and S. Grimaldi. Tracing of shallow water flows through buoyant fluorescent particles. *Flow Measurement and Instrumentation*, 26:93–101, 2012.

[72] F. Tauro, S. Grimaldi, A. Petroselli, and M. Porfiri. Fluorescent particle tracers in surface hydrology: a proof of concept in a natural stream. *Water Resources Research*, 48(6):W06528, 2012.

[73] F. Tauro, S. Grimaldi, A. Petroselli, M. C. Rulli, and M. Porfiri. Fluorescent particle tracers for surface flow measurements: a proof of concept in a semi-natural hillslope. *Hydrology and Earth System Sciences*, 16(8):2973–2983, 2012.

[74] F. Tauro, M. Porfiri, and S. Grimaldi. Fluorescent eco-particles for surface flow physics analysis. *AIP Advances*, 3(3):032108, 2013.

[75] F. Tauro, E. Rapiti, J. F. Al-Sharab, L. Ubertini, P. Grimaldi, and M. Porfiri. Characterization of eco-friendly fluorescent nanoparticle doped-tracers for environmental sensing. *Journal of Nanoparticle Research*, 15(9):1884, 2013.

[76] F. Tauro, G. Mocio, E. Rapiti, S. Grimaldi, and M. Porfiri. Assessment of fluorescent particles for surface flow analysis. *Sensors*, 12(11):15827–15840, 2012.

[77] M. A. Lenzi and L. Marchi. Suspended sediment load during floods in a small stream of the Dolomites (Northeastern Italy). *Catena*, 39(4):267–282, 2000.

[78] T. W. Lambe and R. V. Whitman. *Soil Mechanics*. John Wiley & Sons, New York, 1969.

[79] C. Crowe, M. Sommerfield, and Y. Tsuji. *Multiphase Flows with Droplets and Particles*. CRC Press, Boca Raton, 1998.

[80] W. Merzkirch. *Flow Visualization*. Academic Press, Inc., New York, 1974.

[81] Cospheric LLC. http://www.cospheric-microspheres.com/default.asp, 2010.

[82] D. G. Alciatore and B. Histand. *Introduction To Mechatronics And Measurement Systems*. McGraw–Hill, New York, second edition, 2003.

[83] R. C. Gonzalez, R. E. Woods, and S. L. Eddins. *Digital Image Processing using MATLAB*. Pearson Prentice-Hall, Upper Saddle River, NJ, 2004.

[84] L. Hou, S. Kagami, and K. Hashimoto. Illumination-based synchronization of high-speed vision sensors. *Sensors*, 10(6):5530–5547, 2010.

[85] P. D Z. Varcheie, M. Sills-Lavoie, and G.-A. Bilodeau. A multiscale region-based motion detection and background subtraction algorithm. *Sensors*, 10(2):1041–1061, 2010.

[86] C. M. Tchen. *Mean value and correlation problems connected with the motion of small particles suspended in a turbulent fluid*. PhD thesis, Delft, The Hague, 1947.

[87] S. L. Soo. *Fluid Dynamics of Multiphase Systems*. Blaisdell Publishing Company, Waltham, MA, 1967.

[88] M. R. Maxey and J. J. Riley. Equation of motion for a small rigid sphere in a nonuniform flow. *Physics of Fluids*, 26(4):883–889, 1983.

[89] S. Umeda and W. J. Yang. Dynamics of particles floating on liquid flowing in a semicircular open channel. *Experiments in Fluids*, 12(1):106–112, 1991.

[90] G. K. Batchelor. *An Introduction to Fluid Dynamics*. Cambridge Mathematical Library, New York, 1967.

[91] E. E. Michaelides. Review - The transient equation of motion for particles, bubbles, and dropets. *Journal of Fluids Engineering*, 119(2):233–247, 1997.

[92] I. Kim, S. Elghobashi, and W. A. Sirignano. On the equation for spherical-particle motion: effect of Reynolds and acceleration numbers. *Journal of Fluid Mechanics*, 367(1):221–253, 1998.

[93] W. Holländer and S. K. Zaripov. Hydrodynamically interacting droplets at small Reynolds numbers. *International Journal of Multiphase Flow*, 31(1):53–68, 2005.

[94] R. I. Nigmatulin. *Dynamics of Multiphase Media*, volume 1. Hemisphere, New York, 1991.

[95] J. Jiménez-Lozano, M. Sen, and P. F. Dunn. Particle motion in unsteady two-dimensional peristaltic flow with application to the ureter. *Physical Review E*, 79(4):041901, 2009.

[96] MathWorks. MATLAB 7.5.0 (R2007b).

[97] J. P. Lewis. Fast normalized cross-correlation. http://www.idiom.com/ zilla/papers/nvisioninterface/nip.html.

[98] R. V. Hogg and A. T. Craig. *Introduction to Mathematical Statistics*. Macmillan Publishing Co., New York, fourth edition, 1978.

[99] R. M. Haralick, S. R. Sternberg, and X. Zhuang. Image analysis using mathematical morphology. *IEEE Transactions on Pattern Analysis and Machine Intelligence*, PAMI-9(4):532–550, 1987.

[100] T. Gomi, R. C. Sidle, S. Miyata, K. Kosugi, and Y. Onda. Dynamic runoff connectivity of overland flow on steep forested hillslopes: Scale effects and runoff transfer. *Water Resources Research*, 44(8):W08411, 2008.

[101] K. J. McGuire and J. J. McDonnell. Hydrological connectivity of hillslopes and streams: Characteristic time scales and nonlinearities. *Water Resources Research*, 46(10):W10543, 2010.

[102] T. Uchida and Y. Asano. Spatial variability in the flowpath of hillslope runoff and streamflow in a meso-scale catchment. *Hydrological Processes*, 24(16):2277–2286, 2010.

[103] C. Berger, M. Schulze, D. Rieke-Zapp, and F. Schlunegger. Rill development and soil erosion: a laboratory study of slope and rainfall intensity. *Earth Surface Processes and Landforms*, 35(12):1456–1467, 2010.

[104] A. Ghahramani, Y. Ishikawa, T. Gomi, K. Shiraki, and S. Miyata. Effect of ground cover on splash and sheetwash erosion over a steep forested hillslope: a plot-scale study. *CATENA*, 85(1):34–47, 2011.

[105] J. L. Ticehurst, H. P. Cresswell, N. J. McKenzie, and M. R. Glover. Interpreting soil and topographic properties to conceptualise hillslope hydrology. *Geoderma*, 137(3–4):279–292, 2007.

[106] J. A. Hudson. The impact of sediment on open channel flow measurement in selected UK experimental basins. *Flow Measurement and Instrumentation*, 15(1):49–58, 2004.

[107] R. Rosso, M. C. Rulli, and D. Bocchiola. Transient catchment hydrology after wildfires in a mediterranean basin: runoff, sediment and woody debris. *Hydrology and Earth System Sciences*, 11(1):125–140, 2007.

[108] G. Dunjó, G. Pardini, and M. Gispert. The role of land useland cover on runoff generation and sediment yield at a microplot scale, in a small Mediterranean catchment. *Journal of Arid Environments*, 57(2):99–116, 2004.

[109] L. Hopp and J.J. McDonnell. Connectivity at the hillslope scale: identifying interactions between storm size, bedrock permeability, slope angle and soil depth. *Journal of Hydrology*, 376(3-4):378–391, 2009.

[110] S. H. R. Sadeghi, M. Bashari Seghaleh, and A. S. Rangavar. Plot sizes dependency of runoff and sediment yield estimates from a small watershed. *CATENA*, 102:55–61, 2013.

[111] G. Jost, H. Schume, H. Hager, G. Markart, and B. Kohl. A hillslope scale comparison of tree species influence on soil moisture dynamics and runoff processes during intense rainfall. *Journal of Hydrology*, 420–421:112–124, 2012.

[112] P. Budai and A. Clement. Refinement of national-scale heavy metal load estimations in road runoff based on field measurements. *Transportation Research Part D: Transport and Environment*, 16(3):244–250, 2011.

[113] A. Vacca, S. Loddo, G. Ollesch, R. Puddu, G. Serra, D. Tomasi, and A. Aru. Measurement of runoff and soil erosion in three areas under different land use in Sardinia (Italy). *CATENA*, 40(1):69–92, 2000.

[114] M. C. Rulli, S. Bozzi, M. Spada, D. Bocchiola, and R. Rosso. Rainfall simulations on a fire disturbed mediterranean area. *Journal of Hydrology*, 327(3–4):323–338, 2006.

[115] M. H. Hussein, T. H. Kariem, and A. K. Othman. Predicting soil erodibility in northern Iraq using natural runoff plot data. *Soil and Tillage Research*, 94(1):220–228, 2007.

[116] F. Domingo, L Villagarcía, M. M. Boer, L. Alados-Arboledas, and J. Puigdefábregas. Evaluating the long-term water balance of arid zone stream bed vegetation using evapotranspiration modelling and hillslope runoff measurements. *Journal of Hydrology*, 243(1–2):17–30, 2001.

[117] T. Gomi, R. C. Sidle, M. Ueno, S. Miyata, and K. Kosugi. Characteristics of overland flow generation on steep forested hillslopes of central Japan. *Journal of Hydrology*, 361(3–4):275–290, 2008.

[118] D. G. Doody, A. Higgins, D. Matthews, R. H. Foy, K. Pilatova, O. Duffy, and C. J. Watson. Overland flow initiation from a drumlin grassland hillslope. *Soil Use Management*, 26(3):286–298, 2010.

[119] Á. G. Mayor, S. Bautista, and J. Bellot. Scale-dependent variation in runoff and sediment yield in a semiarid Mediterranean catchment. *Journal of Hydrology*, 397(1–2):128–135, 2011.

[120] A. C. Johnson, A. H. Haria, C. L. Bhardwaj, R. J. Williams, and A. Walker. Preferential flow pathways and their capacity to transport isoproturon in a structured clay soil. *Pesticide Science*, 48(3):225–237, 1996.

[121] P. Fiener and K. Auerswald. Measurement and modeling of concentrated runoff in grassed waterways. *Journal of Hydrology*, 301(1–4):198–215, 2005.

[122] J. Léonard, O. Ancelin, B. Ludwig, and G. Richard. Analysis of the dynamics of soil infiltrability of agricultural soils from continuous rainfall-runoff measurements on small plots. *Journal of Hydrology*, 326(1–4):122–134, 2006.

[123] E. Laloy and C. L. Bielders. Plot scale continuous modelling of runoff in a maize cropping system with dynamic soil surface properties. *Journal of Hydrology*, 349(3–4):455–469, 2008.

[124] N. Mathys, S. Klotz, M. Esteves, M. Descroix, and J. M. Lapetite. Runoff and erosion in the Black Marls of the French Alps: Observations and measurements at the plot scale. *CATENA*, 63(2–3):261–281, 2005.

[125] R. Armand, C. Bockstaller, A.-V. Auzet, and P. Van Dijk. Runoff generation related to intra-field soil surface characteristics variability: Application to conservation tillage context. *Soil and Tillage Research*, 102(1):27–37, 2009.

[126] J. Patin, E. Mouche, O. Ribolzi, V. Chaplot, O. Sengtahevanghoung, K. O. Latsachak, B. Soulileuth, and C. Valentin. Analysis of runoff production at the plot scale during a long-term survey of a small agricultural catchment in Lao PDR. *Journal of Hydrology*, 426–427:79–92, 2012.

[127] L. Tatard, O. Planchon, J. Wainwright, G. Nord, D. Favis-Mortlock, N. Silvera, O. Ribolzi, M. Esteves, and C. H. Huang. Measurement and modelling of high-resolution flow-velocity data under simulated rainfall on a low-slope sandy soil. *Journal of Hydrology*, 348(1-2):1–12, 2008.

[128] J. Lange, N. Greenbaum, S. Husary, J. Timmer, C. Leibundgut, and A. P. Schick. Tracers for runoff generation studies in a mediterranean region: comparison of different scales. In E. Servat, W. Najem, C. Leduc, and A. Shakeel, editors, *Hydrology of the Mediterranean and Semiarid Regions*, volume 278, pages 117–123, Montpellier, France, 2003. IAHS.

[129] E. S. F. Berman, M. Gupta, C. Gabrielli, T. Garland, and J. J. McDonnell. High-frequency field-deployable isotope analyzer for hydrological applications. *Water Resources Research*, 45(10):W10201, 2009.

[130] H. McMillan, D. Tetzlaff, M. Clark, and C. Soulsby. Do time-variable tracers aid the evaluation of hydrological model structure? a multimodel approach. *Water Resources Research*, 48(5):W05501, 2012.

[131] G. Li. Preliminary study of the interference of surface objects and rainfall in overland flow resistance. *CATENA*, 78(2):154–158, 2009.

[132] L. Qu, J. Zhao, X. Zhao, L. Yan, J. Zhou, and T. Lei. A mechanicelectronic sensor for automatic measurement of sediment-laden flow rate from erosion runoff plots. *Journal of Hydrology*, 342(1–2):42–49, 2007.

[133] C. Legout, F. Darboux, Y. Nédélec, A. Hauet, M. Esteves, B. Renaux, H. Denis, and S. Cordier. High spatial resolution mapping of surface velocities and depths for shallow overland flow. *Earth Surface Processes and Landforms*, 37(9):984–993, 2012.

[134] M. Muste, I. Fujita, and A. Hauet. Large-scale particle image velocimetry for measurements in riverine environments. *Water Resources Research*, 44(4):W00D19, 2008.

[135] M. Muste, H-C. Ho, and D. Kim. Considerations on direct stream flow measurements using video imagery: Outlook and research needs. *Journal of Hydro-environment Research*, 5(4):289–300, 2011.

[136] J. LeCoz, A. Hauet, G. Pierrefeu, G. Dramais, and B. Camenen. Performance of image-based velocimetry (LSPIV) applied to flash-flood discharge measurements in Mediterranean rivers. *Journal of Hydrology*, 394(1–2):42–52, 2010.

[137] G. T. Vladisavljević, U. Lambrich, M. Nakajima, and H. Schubert. Production of O/W emulsions using SPG membranes, ceramic α-aluminum oxide membranes, microfluidizers and a silicon microchannel plate–a comparative study. *Colloids and Surfaces, A: Physicochemical and Engineering Aspects*, 232(2–3):199–207, 2004.

[138] A. O. Hanstveit. Biodegradability of petroleum waxes and beeswax in an adapted CO_2 evolution test. *Chemosphere*, 25(4):605–620, 1992.

[139] M. Kubista, R. Sjöback, S. Eriksson, and B. Albinsson. Experimental correction for the inner-filter effect in fluorescence spectra. *Analyst*, 119(3):417–419, 1994.

[140] A. Kurian, N. A. George, B. Paul, V. P. N. Nampoori, and C. P. G. Vallabhan. Studies on fluorescence efficiency and photodegradation of rhodamine 6G doped PMMA using a dual beam thermal lens technique. *Laser Chemistry*, 20(2–4):99–110, 2002.

[141] M. Fikry, M. M. Omar, and L. Z. Ismail. Effect of host medium on the fluorescence emission intensity of rhodamine B in liquid and solid phase. *Journal of Fluorescence*, 19(4):741–746, 2009.

[142] M. Nakanishi, O. Sugihara, N. Okamoto, and K. Hirota. Ultraviolet photobleaching process of azo dye doped polymer and silica films for fabrication of nonlinear optical waveguides. *Applied Optics*, 37(6):1068–1073, 1998.

[143] C. Eggeling, A. Volkmer, and C. A. M. Seidel. Molecular photobleaching kinetics of rhodamine 6G by one- and two-photon induced confocal fluorescence microscopy. *ChemPhysChem*, 6(5):791–804, 2005.

[144] J. R. Albani. *Principles and Applications of Fluorescence Spectroscopy*. Blackwell Publishing Ltd, Oxford, 2007.

[145] J. R. Lakowicz. *Principles of Fluorescence Spectroscopy*. Springer, 2006.

[146] K. Leblanc and D. A. Hutchins. New applications of a biogenic silica deposition fluorophore in the study of oceanic diatoms. *Limnology and Oceanography: Methods*, 3:462–476, 2005.

[147] J. W. M. Bush and J. M. Aristoff. The influence of surface tension on the circular hydraulic jump. *Journal of Fluid Mechanics*, 489:229–238, 2003.

[148] A. Montanari, G. Young, H. Savenije, D. Hughes, T. Wagener, L. Ren, D. Koutsoyiannis, C. Cudennec, S. Grimaldi, G. Bloeschl, M. Sivapalan, K. Beven, H. Gupta, B. Arheimer, Y. Huang, A. Schumann, A. Post, V. Srinivasan, E. Boegh, P. Hubert, C. Harman, S. Thompson, M. Rogger, M. Hipsey, E. Toth, A. Viglione, G. DiBaldassarre, B. Schaefli, H. McMillan, S.J. Schymanski, G. Characklis, B. Yu, Z. Pang, and V. Belyaev. Panta Rhei Everything Flows: Change in hydrology and society The IAHS Scientific Decade 2013-2022. *Hydrological Sciences Journal*, 58(6):1256–1275, 2013.

[149] I. Fujita, M. Muste, and A. Kruger. Large-scale particle image velocimetry for flow analysis in hydraulic engineering applications. *Journal of Hydraulic Research*, 36(3):397–414, 1997.

[150] S. A. Kantoush and A. J. Schleiss. Channel formation during flushing of large shallow reservoirs with different geometries. *Environmental Technology*, 30(8):855–863, 2009.

[151] A. Hauet, M. Muste, and H.-C. Ho. Digital mapping of riverine waterway hydrodynamic and geomorphic features. *Earth Surface Processes and Landforms*, 34(2):242–252, 2009.

[152] T. J. Buchanan and W. P. Somers. Discharge measurements at gaging stations: U.S. geological survey techniques of water-resources investigations. Technical report, U.S. Geological Survey, 1969.

[153] T. H. Yorke and K. A. Oberg. Measuring river velocity and discharge with acoustic Doppler profilers. *Flow Measurement and Instrumentation*, 13(5–6):191–195, 2002.

[154] B. Gunawan, X. Sun, M. Sterling, K. Shiono, R. Tsubaki, P. Rameshwaran, D.W. Knight, J.H. Chandler, X. Tang, and I. Fujita. The application of LS-PIV to a small irregular river for inbank and overbank flows. *Flow Measurement and Instrumentation*, 24:1 – 12, 2012.

[155] S. A. Kantoush, A. J. Schleiss, T. Sumi, and M. Murasaki. LSPIV implementation for environmental flow in various laboratory and field cases. *Journal of Hydro-environment Research*, 5(4):263 – 276, 2011.

[156] A. Bechle, C. Wu, W. Liu, and N. Kimura. Development and application of an automated river-estuary discharge imaging system. *Journal of Hydraulic Engineering*, 138(4):327–339, 2012.

[157] R. Tsubaki, I. Fujita, and S. Tsutsumi. Measurement of the flood discharge of a small-sized river using an existing digital video recording system. *Journal of Hydro-environment Research*, 5(4):313–321, 2011.

[158] A. Hauet, J. D. Creutin, and P. Belleudy. Sensitivity study of large-scale particle image velocimetry measurement of river discharge using numerical simulation. *Journal of Hydrology*, 349(1-2):178 – 190, 2008.

[159] Y. Kim. *Uncertainty analysis for non-intrusive measurement of river discharge using image velocimetry*. PhD thesis, University of Iowa, Iowa City, 2006.

[160] N. V. Hoffer, C. Coopmans, A. M. Jensen, and Y. Chen. A survey and categorization of small low-cost unmanned aerial vehicle system identification. *Journal of Intelligent & Robotic Systems*, 74(1–2):129–145, 2014.

[161] I. Fujita and T. Hino. Unseeded and seeded PIV measurements of river flows video from a helicopter. *Journal of Visualization*, 6(3):245–252, 2003.

[162] I. Fujita and Y. Kunita. Application of aerial LSPIV to the 2002 flood of the Yodo River using a helicopter mounted high density video camera. *Journal of Hydro-environment Research*, 5(4):323 – 331, 2011.

[163] C. Pagano. Development of a quadricopter for environmental flow observations. Master's thesis, New York University Polytechnic School of Engineering, Brooklyn, NY, 2014.

[164] F. Wang, B. Xu, M. Xu, J. Shi, L. Jia, and C. Li. A large-scale particle image velocimetry system based on dual-camera field of view stitching. *Sensors & Transducers*, 157(10):234–239, 2013.

[165] L. Gui. EDPIV - Evaluation Software for Digital Particle Image Velocimetry. http://lcgui.net, 2013.

[166] I. Sa and P. Corke. System identification, estimation and control for a cost effective open-source quadcopter. In *Proceedings of the IEEE International Conference on Robotics and Automation (ICRA)*, pages 2202–2209, 2012.

[167] R. P. Breckenridge, M. Dakins, S. Bunting, J. L. Harbour, and S. White. Comparison of unmanned aerial vehicle platforms for assessing vegetation cover in sagebrush steppe ecosystems. *Rangeland Ecology & Management*, 64(5):521–532, 2011.

[168] J.R. Azinheira and A. Moutinho. Hover control of an uav with backstepping design including input saturations. *IEEE Transactions on Control Systems Technology*, 16(3):517–526, 2008.

[169] S. Bouabdallah, M. Becker, and R. Siegwart. Autonomous miniature flying robots: coming soon! - Research, development, and results. *IEEE Magazine on Robotics & Automation*, 14(3):88–98, 2007.

[170] H. Lim, J. Park, D. Lee, and H. J. Kim. Build your own quadrotor: open-source projects on unmanned aerial vehicles. *IEEE Magazine on Robotics & Automation*, 19(3):33–45, 2012.

[171] http://www.aibotix.com.

[172] L. Dingle and M. H. Tooley. *Aircraft Engineering Principles*. Elsevier, Burlington, 2013.

[173] APM: Copter, 2013.

[174] J. Y. Bouguet. *Camera Calibration Toolbox for Matlab*. California Institute of Technology, 2013.

[175] D. Brown. Close-range camera calibration. *Photogrammetric Engineering*, 37(8):855–866, 1971.

[176] Z. Zhang. A flexible new technique for camera calibration. *IEEE Transactions on Pattern Analysis and Machine Intelligence*, 22(11):1330–1334, 2000.

[177] W. Thielicke and E. J. Stamhuis. PIVlab - time-resolved particle image velocimetry (PIV) tool, 2010.

[178] Marcos, J. R. Seymour, M. Luhar, W. M. Durham, J. G. Mitchell, A. Macke, and R. Stocker. Microbial alignment in flow changes ocean light climate. *Proceedings of the National Academy of Sciences of the United States of America*, 108(10):3860–3864, 2011.

[179] M. C. Rulli, A. Saviori, and P. D'Odorico. Global land and water grabbing. *Proceedings of the National Academy of Sciences of the United States of America*, 2013. Published ahead of print.

[180] J. H. Agui and Y. Andreopoulos. A new laser vorticity probe - LAVOR: its development and validation in a turbulent boundary layer. *Experiments in Fluids*, 34(2):192–205, 2003.

[181] M. A. Green, C. W. Rowley, and A. J. Smits. Using hyperbolic Lagrangian coherent structures to investigate vortices in bioinspired fluid flows. *Chaos*, 20(1):017510, 2010.

[182] F. Reinders, I. A. Sadarjoen, B. Vrolijk, and F. H. Post. Vortex tracking and visualisation in a flow past a tapered cylinder. *Computer Graphics Forum*, 21(4):675–682, 2003.

[183] A. Abdelkefi, R. Vasconcellos, A. H. Nayfeh, and M. R. Hajj. An analytical and experimental investigation into limit-cycle oscillations of an aeroelastic system. *Nonlinear Dynamics*, 71(1–2):159–173, 2013.

[184] I. A. Sadarjoen and F. H. Post. Detection, quantification, and tracking of vortices using streamline geometry. *Computers & Graphics*, 24(3):333–341, 2000.

[185] F. H. Post, B. Vrolijk, H. Hauser, R. S. Laramee, and H. Doleisch. The state of the art in flow visualisation: feature extraction and tracking. *Computer Graphics Forum*, 22(4):775–792, 2003.

[186] P. Chakraborty, S. Balachandar, and R. J. Adrian. On the relationships between local vortex identification schemes. *Journal of Fluid Mechanics*, 535:189–214, 2005.

[187] J. F. Foss. Surface selections and topological constraint evaluations for flow field analysis. *Experiments in Fluids*, 37(6):883–898, 2004.

[188] S. Depardon, J. J. Lasserre, L. E. Brizzi, and J. Borée. Automated topology classification method for instantaneous velocity fields. *Experiments in Fluids*, 42(5):697–710, 2007.

[189] A. Pobitzer, R. Peikert, R. Fuchs, B. Schindler, A. Kuhn, H. Theisel, K. Matković, and H. Hauser. The state of the art in topology-based visualization of unsteady flow. *Computer Graphics Forum*, 30(6):1789–1811, 2011.

[190] P. J. Strykowski and K. R. Sreenivasan. On the formation and suppression of vortex "shedding" at low Reynolds numbers. *Journal of Fluid Mechanics*, 218:71–107, 1990.

[191] L. N. Cattafesta and M. Sheplak. Actuators for active flow control. *Annual Review of Fluid Mechanics*, 43(1):247–272, 2011.

[192] N. Kasagi, Y. Suzuki, and K. Fukagata. Microelectromechanical systems-based feedback control of turbulence for skin friction reduction. *Annual Review of Fluid Mechanics*, 41:231–251, 2009.

[193] S. T. Roweis and L. K. Saul. Nonlinear dimensionality reduction by locally linear embedding. *Science*, 290(5500):2323–2326, 2000.

[194] J. B. Tenenbaum, V. deSilva, and J. C. Langford. A global geometric framework for nonlinear dimensionality reduction. *Science*, 290(5500):2319–2323, 2000.

[195] E. Bollt. Attractor modeling and empirical nonlinear model reduction of dissipative dynamical systems. *International Journal of Bifurcation and Chaos*, 17(4):1199–1219, 2007.

[196] D. Beymer and T. Poggio. Image representations for visual learning. *Science*, 272(5270):1905–1909, 1996.

[197] J. Blackburn and E. Ribeiro. Human motion recognition using Isomap and dynamic time warping. In A. Elgammal, B. Rosenhahn, and R. Klette, editors, *Human Motion - Understanding, Modeling, Capture and Animation*, volume 4814, pages 285–298, Rio de Janeiro, Brazil, 2007. Springer Berlin Heidelberg.

[198] N. Abaid, E. Bollt, and M. Porfiri. Topological analysis of complexity in multiagent systems. *Physical Review E*, 85(4):041907, 2012.

[199] A. Roshko. On the development of turbulent wakes from vortex streets. *National Advisory Committee for Aeronautics*, Report 1191, 1954.

[200] D. J. Tritton. Experiments on the flow past a circular cylinder at low Reynolds numbers. *Journal of Fluid Mechanics*, 6(4):547–567, 1959.

[201] A. E. Perry, M. S. Chong, and T. T. Lim. The vortex-shedding process behind two-dimensional bluff bodies. *Journal of Fluid Mechanics*, 116:77–90, 1982.

[202] D. J. Olinger and K. R. Sreenivasan. Nonlinear dynamics of the wake of an oscillating cylinder. *Physical Review Letters*, 60(9):797–800, 1988.

[203] M. C. Wolochuk, M. W. Plesniak, and J. E. Braun. The effects of turbulence and unsteadiness on vortex shedding from sharp-edged bluff bodies. *Journal of Fluids Engineering*, 118(1):18–25, 1996.

[204] G. S. Young and J. Zawislak. An observational study of vortex spacing in island wake vortex streets. *Monthly Weather Review*, 134(8):2285–2294, 2006.

[205] C. Morton and S. Yarusevych. Vortex shedding in the wake of a step cylinder. *Physics of Fluids*, 22(8):083602, 2010.

[206] R. W. Floyd. Algorithm 97: Shortest path. *Magazine Communications of the ACM*, 5(6):345, 1962.

[207] T. F. Cox and M. A. Cox. *Multidimensional Scaling*. Chapman and Hall, London, 1994.

[208] D. Sumner, S. J. Price, and M. P. Païdoussis. Flow-pattern identification for two staggered circular cylinders in cross-flow. *Journal of Fluid Mechanics*, 411(1):263–303, 2000.

[209] H. Schlichting and K. Gersten. *Boundary-Layer Theory*. Springer, Germany, 2000.

[210] M. Hammache and M. Gharib. An experimental study of the parallel and oblique vortex shedding from circular cylinders. *Journal of Fluid Mechanics*, 232:567–590, 1991.

[211] G. M. Quénot, J. Pakleza, and T. A. Kowalewski. Particle image velocimetry with optical flow. *Experiments in Fluids*, 25(3):177–189, 1998.

[212] A. Szymczak, A. Stillman, A. Tannenbaum, and K. Mischaikow. Coronary vessel trees from 3D imagery: a topological approach. *Medical Image Analysis*, 10(4):548–559, 2006.

[213] L. M. Pedersen, T. A. L. Pedersen, E. M. Pedersen, H. Højmyr, K. Emmertsen, and V. E. Hjortdal. Blood flow measured by magnetic resonance imaging at rest and exercise after surgical bypass of aortic arch obstruction. *European Journal Cardio-Thoracic Surgery*, 37(3):658–661, 2010.

[214] M. E. Schaepman, S. L. Ustin, A. J. Plaza, T. H. Painter, J. Verrelst, and S. Liang. Earth system science related imaging spectroscopy - an assessment. *Remote Sensing of Environment*, 113(1):S123–S137, 2009.

[215] M. Jadaliha and J. Choi. Environmental monitoring using autonomous aquatic robots: sampling algorithms and experiments. *IEEE Transactions on Control Systems Technology*, 21(3):899–905, 2013.